QUANTIFYING THE INTERFACE DEFORMATION MECHANISMS IN NANOSTRUCTURED METALS WITH ATOMIC SIMULATIONS AND CONTINUUM FIELD REPRESENTATIONS

BY

RUIZHI LI

DISSERTATION

Submitted in partial fulfillment of the requirements
for the degree of Doctor of Philosophy in Aerospace Engineering
in the Graduate College of the
University of Illinois at Urbana-Champaign, 2017

Urbana, Illinois

Doctoral Committee:

Assistant Professor Huck Beng Chew, Chair
Professor John Lambros
Professor Philippe H Geubelle
Professor Huseyin Sehitoglu

ABSTRACT

Nanostructured metals possess ultra-high mechanical strength. A well-established consensus is that the deformation behaviors of these materials are governed by the high density of interfaces. Previous studies have shown that, at nanoscale, interfaces act not only as obstacles of dislocations but also as main sources for dislocation emission. However, due to the lack of proper descriptors for interface structures, it is difficult to quantify the interface-dislocation interaction mechanisms in the nanostructured metals.

Targeting to resolve this problem, my research is divided into two steps. In the first step, the interface-dominant plastic deformation mechanisms of semi-coherent Cu–Ag and Cu-Al nanolayered metals, subjected to out-of-plane tension, are investigated by molecular dynamics (MD) simulations. The results show that the initially planar Cu–Ag nanolayers abruptly become wavy at a critical tensile strain. High stress concentrations subsequently develop at the summits and valleys of the wavy Cu–Ag interlayer interfaces, from which micro-twinning partials are emitted. On the other hand, stacking fault tetrahedra (SFTs) are observed initiating from the Cu–Al semi-coherent interface. The closed SFTs within the Cu interlayers and open-ended SFTs within the Al interlayers envelop Cu-Al interface and result in considerable strain hardening of the Cu–Al nanolayers. These contrasting observations in Cu-Ag and Cu-Al nanolayers are associated with the different shear resistance along the respective interfaces and they both introduce new length scale effect to determine the macroscopic strength of the nanolayered metals.

While postdictive MD simulations can be used to characterize the mechanics of the interfaces, in the second step of my research, the notion of continuum-equivalent traction fields is introduced as local quantitative interface descriptors to predict the deformation behaviors directly from the atomic interface structure. These descriptors are applied to symmetrical-tilt ⟨110⟩ Ni

grain boundaries and successfully predict the critical stress for dislocation emissions. Additionally, the traction signatures along the grain boundaries are used to explain the tension-compression asymmetry of grain boundaries to nucleate dislocations.

Traction signatures descriptors can potentially be used to establish the relationship between the atomic structure of grain boundary and its propensity to impede, absorb, or transmit dislocations. The descriptors are also expected to broadly apply to more complex interface structures, such as heterogeneous interfaces.

ACKNOWLEDGEMENTS

I would like to express my appreciation to many people for offering me generous support during my PhD study. First of all, I owe gratitude to my advisor, Professor Huck Beng Chew, who provides me funding to pursue my Master and PhD degrees, and gives me great help in my application for US Visa. In these five years, he devotes plenty of time to develop my research habit, improve my writing skill, elevate my presentation performance and grant me lots of vacations with my friends. Also, I would like to thank Prof. Chew not only as my advisor but also as my good friend, who gives me multiple suggestions on how to improve my English and how to communicate with people. He guides me into the academia world and I shall follow him as a model to pursue my academic position in the future.

I would like to thank all my wonderful colleagues in the group, including the ones who are already graduated, who are still in the group, and who just joins us. For over thousands of days, we work together, chat, discuss, and play together in Talbot 324. Without you guys, my research life would be boring and painful. I would like to thank all the professors who used to teach me courses in these years. With the help of the knowledge you gave me, I could manage my research project smoothly. With the teaching skill I learned in your class, I believe that I could be an excellent professor as well in the future. Specially, I thank my committee members: Professors Huseyin Sehitoglu, John Lambros, and Philippe H Geubelle, who not only teach me many courses but also spend their time and input to guide my research project.

Thank you to all my friends in Urban-Champaign. Although many of you have graduated and left to other places, I still can remember and bear in mind forever the time we spent together. Those happy and joyful moments make me feel warm in this lonely middle-west small town and already weave into my memory of PhD life.

The last but not the least, thank you to my parents. Although 7000 miles apart between us, your encouragement and support always grant me full strength and motivation to put my shoulder to the wheel. Finally, I want to give special thanks to my girlfriend. For over 5 years, she waited for me and came to visit me every year. I am going to propose to her after my graduation. This PhD degree is my best gift for her.

TABLE OF CONTENTS

Chapter 1. Introduction

Nanostructured metals have order-of-magnitude higher mechanical strength compared to their traditional coarse-grained counterparts and therefore are highly promising as the next-generation aerospace materials [1, 2]. It is now well-accepted that the ultra-high mechanical strength of these materials stems from their high interface density [3, 4]. In traditional coarse-grained metals, the interfaces impede the motion of pre-existing dislocations (line defects) across different grains, leading to dislocation pile-up at the interface and consequently forest hardening [5, 6]. As the grain size decreases, the increasing density of interfaces provides more obstacles for dislocation motion, leading to increased mechanical strength governed by the famous Hall-Petch relationship [7, 8]. At grain-sizes of below $\sim 50nm$, however, the density of pre-existing dislocations become significantly smaller. The strength of these nanostructured metals is instead controlled by the confined slip of dislocation within single grain or interlayer [9]. As grain size reduced to ~10nm, nucleation of dislocations from the interfaces, as well as the interactions between dislocations and interfaces without the help of local "pile-up" stress, determines the materials' strength [10-12]. Through understanding and quantifying the interface-dominant deformation mechanisms, the long-term goal of my research aims to establish the relationship between the atomic structure of the interfaces and deformation response in nanostructured metals.

My thesis research is divided into two parts. The first part studies the complex interface-dominant deformation mechanisms in nanoscale bi-metal Cu-Ag and Cu-Al multilayered metals, under loading-conditions relevant to the deformation of bulk polycrystalline Cu-Ag and Cu-Al nanolayered metals. While the interfaces of Cu-Ag and Cu-Al nanolayered metals are both semi-coherent and have almost the same lattice mismatch across the interface, the deformation mechanisms revealed by molecular dynamics (MD) simulations are surprisingly different.

Specifically, a transition of the interlayers from initially planar to wavy is observed for Cu-Ag nanolayered metals subjected to out-of-plane tensile deformation. While the development of stacking fault tetrahedra (SFTs) along the interlayer interfaces is demonstrated for Cu-Al nanolayered metals under the same loading condition. The activation of both deformation mechanisms introduces new competing length-scale effects for macroscopic strength of nanolayered metals, which can ultimately explain the saturation in the yield strength of these materials with decreasing interlayer thickness below ~10 nm shown in experiments [9, 13]. Motivated by the sensitivity of the deformation mechanisms to the atomic structure of the interface, the second part of my thesis research focuses on quantifying the relationship between the atomic structure of interfaces and the propensity of these interfaces to emit dislocations with the notion of continuum-equivalent traction fields as quantitative interface descriptors. For simplicity, symmetrical-tilt ⟨110⟩Ni grain boundaries are investigated with a generalized framework based on the virtual work principle to reconstruct the traction distributions along the interface. The research uncovers the relationship between the grain boundary tractions and the critical stress to trigger dislocation emissions from the boundary. It also successfully explains the tension-compression asymmetry of dislocation emission from these grain boundary structures. The traction-based interface descriptors are expected to be applicable to quantify multiple dislocation-interface interactions across general interface structures, including semi-coherent Cu-Al and Cu-Ag interfaces.

The organization of thesis document is as follows: Chapter 2 provides an overview of state-of-the-art approaches for characterizing grain boundary and heterogeneous interface structures. The interface deformation mechanics are also reviewed in this chapter. Chapter 3 presents the results of my MD simulations on the deformation response of Cu-Ag and Cu-Al nanolayered

metals, in which two unique deformation mechanisms are uncovered, activated under out-of-plane tensile deformation: the planar-to-wavy transition for Cu-Ag nanolayers, and the formation of SFTs for Cu-Al interlayers. The relationship between these deformation mechanisms and the macroscopic strength of the respective nanolayered metals is discussed. Chapter 4 focuses on the notion of continuum-equivalent traction fields as local quantitative descriptors of interfaces. The approach to reconstruct the continuous interface tractions from atomic stress information in the vicinity of grain boundary is presented in the context of symmetrical-tilt $\langle 110 \rangle$Ni grain boundaries. The relationship between the traction signatures along these grain boundaries and the propensity of the boundaries to emit dislocations is quantified. In addition, my results explain the asymmetrical dislocation emission processes of these grain boundary structures under applied uniaxial tension and compression loading. In Chapter 5, the main findings of my research are summarized and some potential future works are suggested.

Chapter 2. Literature Review

The interfaces in nanostructured metals can be categorized as: (a) homogeneous interfaces (grain boundaries), which separate two crystals of the same metal in the same phase and (b) heterogeneous interfaces, which separate two different metals or two different phases of the same metal. In this chapter, an overview of recent efforts to characterize the atomic structures of homogeneous and heterogeneous interfaces, as well as to quantify the deformation mechanisms of these interfaces, are presented.

2.1 Homogeneous Interfaces

Grain boundaries are typically categorized by the mis-orientation angle between the two component grains. The infinite possible mis-orientation angles and multiple rotation methods give infinite number of possible grain boundary structures. However, there are certain special orientations of grain boundaries which are energetically favorable, and can be characterized by the Coincidence Site Lattice (CSL) theory [14, 15]. The CSL theory describes the degree of fit between the structures of the two grains. When the crystal lattice of one grain is virtually extended across the boundary to the other one, the superimposed lattices will have a certain number of overlapping atoms; the reciprocal of the fraction of coincidence sites to the total number of lattice sites is defined as the CSL value (Σ). Taking $\Sigma 3(111)$ grain boundary as an example, Fig. 2.1 shows a schematic of how to calculate CSL values. Using electron back scattering diffraction (EBSD) techniques and high resolution transmission electron microscopy (HRTEM), researchers are able to determine the grain orientations and in-turn the CSL value of the grain boundary [16, 17]. Early experimental studies appeared to show that a lower Σ value leads to a more stable grain boundary

structure, i.e. one that has reduced propensity for dislocation nucleation or transmission [18, 19], however this has been disproved in later experimental studies [20]. Another interface descriptor, the grain boundary energy, is used to quantify the excess energy contributed by the presence of the grain boundary structure. Olmsted, Foiles & Holm (2009) calculated the grain boundary energies for a comprehensive set of 388 distinct grain boundaries in Al and Ni, but could not find a distinct correlation between the boundary energy and the propensity for dislocation nucleation or transmission from grain boundaries [21].

Sutton and Vitek (1983) proposed the idea of Structure unit (SU) models to represent the local atomic structures of tilt grain boundaries [22]. They demonstrated that certain favored grain boundaries comprise of a contiguous sequence of one unique type of structural element defined as a structure unit (SU), while other non-favored grain boundaries are composed of combinations of different types of SUs. Rittner and Seidman (1996) characterized the SUs in twenty-one $\langle 110 \rangle$ symmetric tilt Cu grain boundaries using atomic simulations [23]. They showed that the extensive local atomic relaxations in low-stacking fault energy FCC metals result in delocalized/dissociated grain boundary structures, which are incompatible with the SU model. Depending on the mis-orientation angle, the individual SUs within different grain boundaries can have different extents of distortion which ultimately determine the propensity of the boundary to emit/transmit dislocations [24].

Because of the lack of suitable interface descriptors, the role of the atomic structure of grain boundary in the emission or transmission of dislocations is still not well understood. Material hardening laws based on dislocation pile-up model consider only the lattice orientations of adjacent grains, but have largely neglected the role of grain boundary structure [5]. Instead, the deformation mechanics of the grain boundary structure have been mostly studied with MD simulations. For

example, Yamakov et al. (2002) demonstrated that micro-twins, formed by emission of consecutive ⟨112⟩ Shockley partial dislocations from grain boundaries and triple junctions, play an important role in the plastic deformation of nanocrystalline metals, which is in contrast to coarse-grained metals where full dislocation slip dominants the deformation process [10]. In another study, Li et al. (2010) showed that the emission of dislocations from the grain boundaries softens nanocrystalline Cu with nano-twinned grains and limits the maximum strength of the metal [12]. McPhie and co-workers (2012) also showed via atomic simulations that the defect sites within grain boundary structures are more likely to nucleate partial dislocations first [25]; similar observations have been reported by Mompiou et al. (2012) using TEM [26].

Focusing on the relationship between the SU descriptors of the grain boundary and the propensity of the boundaries to emit dislocations, Tschopp et al. (2007) and Spearot et al. (2007) demonstrated that grain boundaries with high interfacial free volume, denoted by E-SUs along the boundary, generally have lower dislocation nucleation strength under tension [27, 28]. However, a direct correlation between the extent of free volume along the boundary and the critical dislocation nucleation strength of the boundary still cannot be established. Tschopp et al. (2008) further showed that symmetric tilt <110> Cu grain boundaries with E-SUs have three-time higher nucleation stress for dislocation emission under uniaxial compression compared to uniaxial tension [29]. They attributed this tension-compression asymmetry in the dislocation nucleation stress to: (a) the Burgers vector of pre-existing dislocations along the grain boundary may be affected differently by the direction of external loading, and (b) the changes in the sign of the resolved stress normal to the slip plane which may affect the barrier stress for shear slip. Sangid and co-workers (2011) calibrated the energy barrier of a grain boundary to emit/transmit dislocations using postdictive molecular dynamics (MD) simulations, and proposed an analytical framework

incorporating the MD-calibrated barrier energy of the boundary to predict the possible activated slip system for grain boundaries under loading [30].

Despite the efforts outlined above which demonstrate the close relationship between the atomic structure of the grain boundary and its deformation response, these available interface descriptors, including CSL, grain boundary energy and interface porosity, are qualitative in nature. As such, direct prediction of the dislocation nucleation stress based on the grain boundary atomic structure remains elusive. Part of my research efforts present in this thesis centers on the development of continuum-equivalent traction fields as local quantitative descriptors for interfaces. The traction fields are capable of predicting the critical stress to trigger dislocation emissions from the grain boundaries.

2.2 Heterogeneous Interface

The atomic structure of a heterogeneous interface, which separates two different metals or two different phases of the same metal, is far more complicated than the typical grain boundary structure in polycrystalline metals. These heterogeneous interfaces are qualitatively categorized as coherent, semi-coherent and incoherent, depending on the extent of lattice mismatch between the two components [31-33]. When two crystal structures with small lattice mismatch of <5% are joined together at an interface, the small lattice mismatch can be accommodated by elastic strains (termed coherency strains) resulting in a coherent interface structure. When the lattice mismatch between crystal structures exceeds ~25%, a weakly-bonded incoherent interface structure (e.g. Cu-Nb) then forms between the two metals/phases. As to two crystal structures with lattice mismatch in between (e.g. Cu-Ag, Cu-Al), semi-coherent interfaces are formed [34]. These semi-coherent

interfaces have misfit dislocations which are periodically introduced to reduce the mismatch strain. Fig. 2.2 presents examples or schematics of the three interfaces.

Nanoscale multilayered metals are ideal model systems to elucidate the deformation mechanics of heterogeneous interfaces. Since the dissociated semi-coherent interface structures possess periodical coherent and incoherent regimes along the interface, my research here focuses on interfaces in semi-coherent Cu-Ag and Cu-Al nanolayered metals. Over the past 30 years, mechanical properties of nanolayered metals were obtained from in-plane tension experiments using micro electro mechanical systems (MEMS) or from nanoindentation tests [35]. For example, nanoindentation experiments showed that the measured hardness of Cu-Ag nanolayered metals increases from 2 GPa to ~5 GPa as the interlayer thickness decreases from 200 nm to 1.2 nm [36]. Later in-plane tension experiments also showed an increase in the tensile strength of Cu-Ag nanolayered metals with decreasing interlayer thickness, reaching a peak of ~700 MPa at an interlayer thickness of 2 nm [37]. The large discrepancy of yield strength between in-plane tension and indentation tests indicates different deformation mechanisms for Cu-Ag nanolayered metals under the two loading conditions (Fig. 2.3) [38]. To investigate interface structure as well as interface-dislocation interaction mechanisms, numerical simulations on Cu-Ag multilayered metals have been taken. Li et al. [39] presented a two-dimensional quasi-continuum analysis for Cu-Ag multilayers subjected to nanoindentation. They showed that dislocations emitted under compression originate from the misfit dislocations at the semi-coherent interlayer interfaces. In another study [40], Wang et al. showed that the semi-coherent {111} Cu-Ag interface structure can facilitate the transmission of twinning partials. More recently, eutectic composites of bulk Cu-Ag, comprising of colony grains with Cu-Ag nanolayers within each grain, were successfully fabricated (Fig. 2.4) [41]. This brought forth the possibility of using nanolayered metals as loading

bearing structures which can be subjected to multiaxial loading conditions. However, while the traditional focus has been on the in-plane tensile and nanoindentation response, little is understood about of the out-of-plane tensile properties of these Cu-Ag nanolayered metals.

On the other hand, there were only a few researches on Cu-Al multilayers due to the fabrication difficulty. References have shown that due to the strong interaction of these two metallic components, reaction and diffusion occur during the current preparation process of Cu-Al interfaces and form compound such as Al_2Cu [42, 43]. However, these reactions indicate strong bond between Cu and Al atoms, which can lead to "strong" interface between Cu and Al. Nevertheless, it is still instructive to examine the semi-coherent Cu-Al interface as a comparison to Cu-Ag interface since they are both semi-coherent interfaces with almost the same lattice mismatch ($\delta_{Cu-Ag} = 13\%\ vs.\ \delta_{Cu-Al} = 12\%$).

2.3 Figures

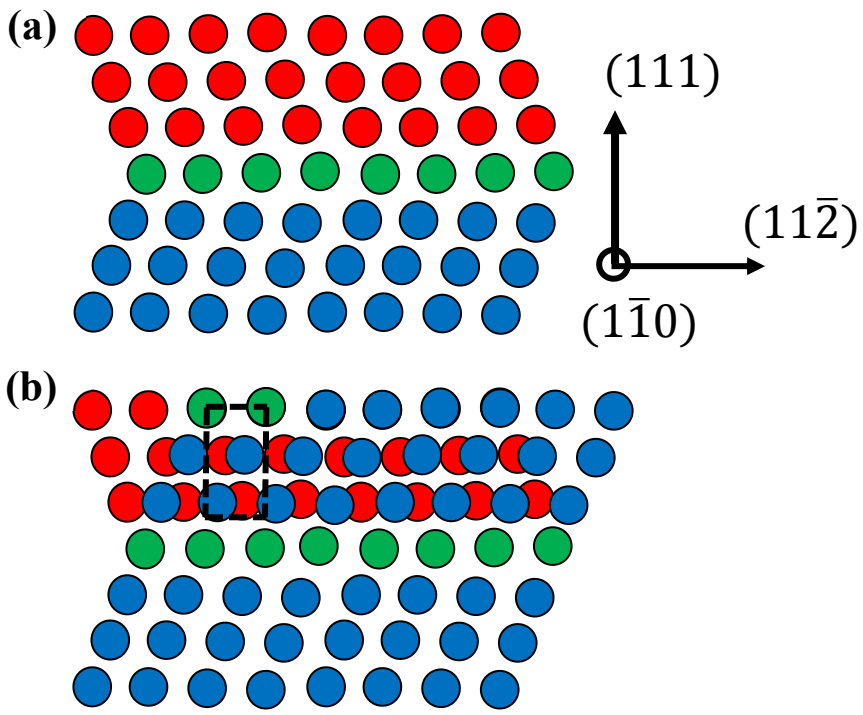

Figure 2.1 (a) Schematic of $\Sigma 3(111)$ twin boundary, atoms in top and bottom grains are colored in red and blue respectively, while boundary atoms are colored in green. (b) Schematic of Coincident site lattice (CSL), the bottom grain is expanded to the top one. In the dash line rectangle, there are 2 overlap atoms among in total 6 atoms, the CSL value is 3.

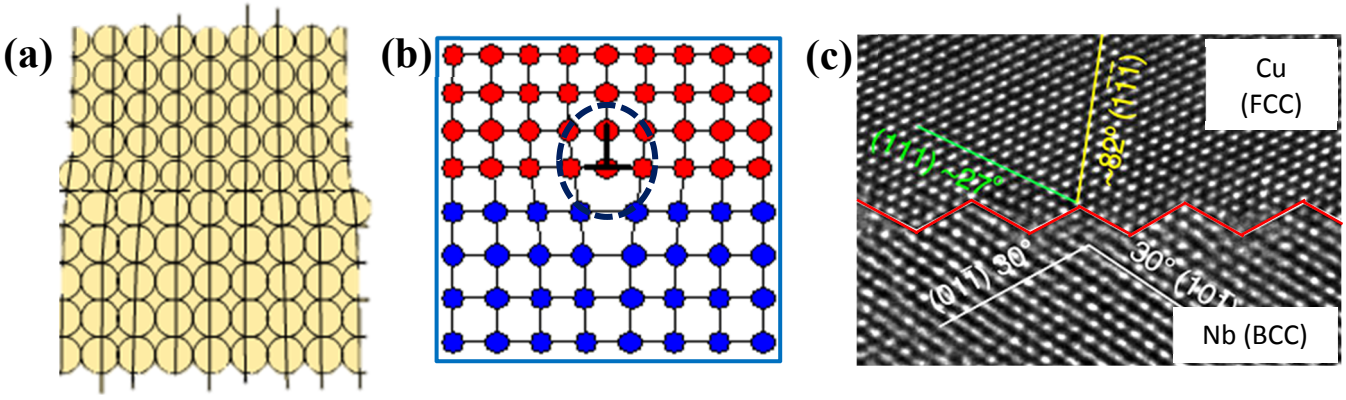

Figure. 2.2 (a) Schematic of coherent interface [44]; (b) Schematic of semi-coherent interface with misfit dislocations in black circle [45]; (c) HRTEM image of Cu-Nb incoherent interface [46].

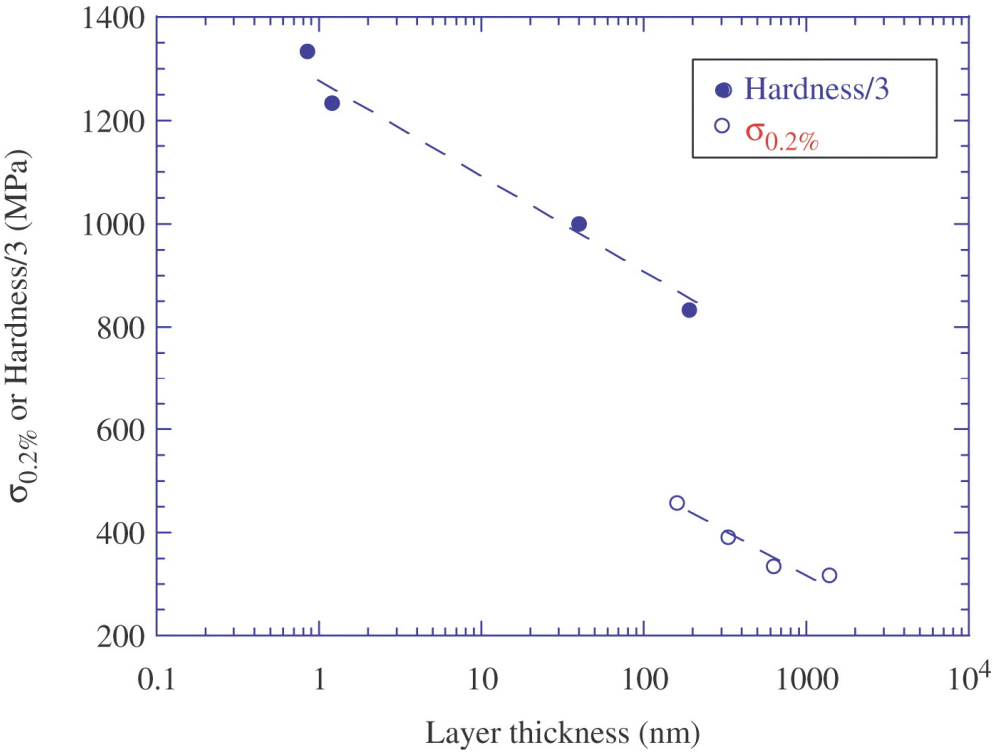

Figure 2.3 Comparison of 0.2% yield stress from in-plane tensile tests and hardness from nanoindentation with various layer thickness [38].

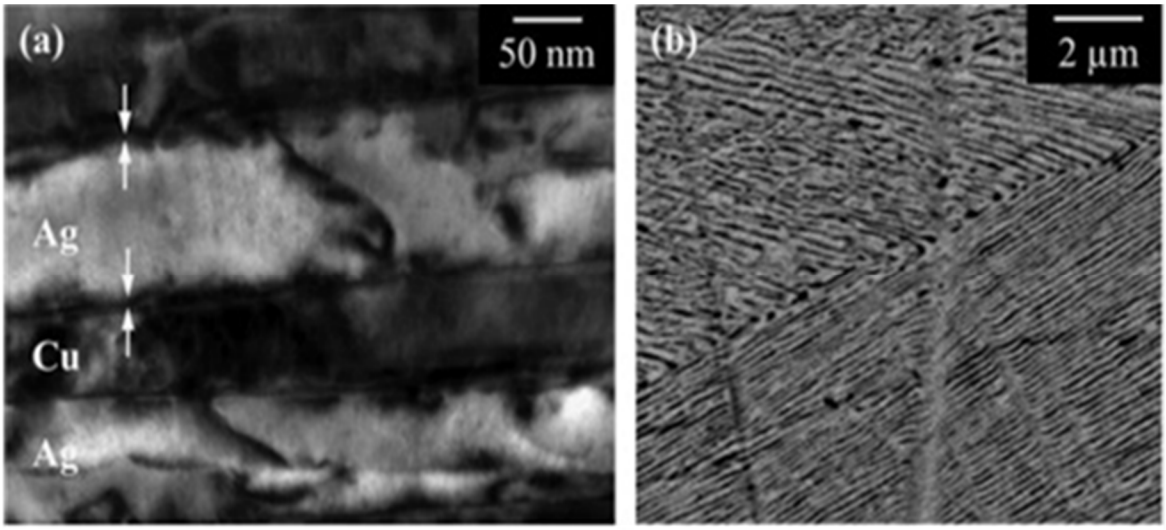

Figure 2.4 Polycrystalline eutectic Cu-Ag nanolayers prepared by flux melting technique. (a) The Cu-Ag nanolayers in individual grain taken by TEM (b) SEM micrograph showing the polycrystalline eutectic structure. [41]

Chapter 3. MD Simulations on Nanolayered Metals[1]

In the first part, my research focuses on investigating the deformation mechanics of heterogeneous interfaces of nanoscale multilayered Cu-Ag and Cu-Al metals using molecular dynamics (MD) simulations. The nanolayered metals are subjected to out-of-plane (normal to interface) tensile deformation. This loading condition is a departure from previous experimental and computational studies, which have characterized the behavior of nanolayered metals under out-of-plane compression or in-plane tension. The two Cu-Al and Cu-Ag model systems, while sharing the same semi-coherent interface structure with similar lattice mismatch, have significantly different interfacial shear properties. The uncovered interface mechanics provides insights into how this interface shear stress translates to plasticity of the nanolayered metals.

3.1 MD Modeling

The MD simulations are performed by using the research code LAMMPS [47]. The interaction between atoms for the Cu-Ag and Cu-Al nanolayers are governed by embedded atom method (EAM) potentials specifically developed for these metal systems [48, 49]. With interatomic potential energy function, the force acting on each atom can be obtained from the gradient of the potential energy function. While the motion of individual atoms is then governed by classical Newtonian mechanics [50]. A schematic of the MD model is shown in Fig. 3.1a. The

---

1. Some of the results presented in this chapter have been previously published in the following publication:
Li, R., & Chew, H. B. (2015). Planar-to-wavy transition of Cu–Ag nanolayered metals: a precursor mechanism to twinning. *Philosophical Magazine,* 95(10), 1029-1048.
Li, R., & Chew, H. B. (2015). Closed and open-ended stacking fault tetrahedra formation along the interfaces of Cu–Al nanolayered metals. *Philosophical Magazine,* 95(25), 2747-2763. Reprinted with permission from the publisher.

interface planes of the Cu-Ag or Cu-Al nanolayered metals are aligned normal to the [111] (x_2) loading direction. The atoms are in the cube-on-cube closed-pack sequence, and the interlayer thickness (h) is uniform within each model. To mimic the behavior of bulk nanolayered metals, periodic boundary conditions are imposed in all three directions of the simulation box. The MD model sizes are set to be sufficient large to elucidate the deformation behaviors discussed in my research, with each comprising of a few millions of atoms.

As aforementioned, both the Cu-Ag and Cu-Al interfaces are semi-coherent, and have similar lattice mismatch across the interlayer interfaces. To account for this lattice mismatch in the MD modeling, misfit dislocations are introduced periodically along both the Cu-Ag and Cu-Al interfaces. This is achieved by matching the rational number of planes of atoms in the Cu and Ag (Al) interlayers. The bulk lattice parameters of Ag (Al) and Cu are almost commensurate with the ratio n = d(Ag/Al):d(Cu) = 8:9, i.e. $8a_{\mathrm{Ag/Al}} \approx 9a_{\mathrm{Cu}}$. Hence, an additional plane of atoms is introduced in Cu for every 8 planes of atoms in Ag (Al) in both the $[11\bar{2}]$ (x_1) and $[1\bar{1}0]$ (x_3) directions. This is achieved by constraining the in-plane model dimensions in the x_1 and x_3 directions to be integer multiples of $\frac{\sqrt{6}}{6}\frac{(9a_{\mathrm{Cu}}+8a_{\mathrm{Ag/Al}})}{2}$ and $\frac{\sqrt{2}}{2}\frac{(9a_{\mathrm{Cu}}+8a_{\mathrm{Ag/Al}})}{2}$, and constructing the Cu and Ag (Al) layers independently based on their individual bulk lattice parameters. This approach is similar to previous MD modelling of semi-coherent interfaces in the Ref. [9, 40]. After energy minimization using the conjugate gradient method, the misfit dislocations along the (111) interface dissociate into triangular $\frac{1}{6}\langle 112\rangle$ Shockley partial dislocations intersecting at 60º. Fig. 3.1b shows the top view of the Cu-Ag (Al) interface structure, with the Burgers vectors of the Shockley partials as marked in white arrow; a corresponding A-A cross-sectional cut across the mid-section of a typical stacking fault triangle is shown in Fig. 3.1c. The atoms are colored by their centro-symmetry parameter (CSP) value, which tracks the local lattice disorder around

individual atom and scales from red to white and then to blue [51]. Thus, perfect FCC atoms are colored in red, dislocation cores are in white, and stacking faults are in blue. Observe that the intersecting misfit partial dislocations separate the Cu-Ag (Al) interface into triangular FCC and stacking fault regions. The resulting distribution and dimensions of stacking fault triangles in the computational model are reported in some previous simulation work [52]. It is also in good agreement with that observed experimentally by Scanning Tunneling Microscopy (STM) imaging of a single monolayer of Ag on (111) Cu [53], as well as recent HRTEM image of {111} Cu-Ag interface in eutectic Cu-Ag nanocomposites [54].

The MD simulations are conducted with NPT ensemble. The model structures are heated up to 300 K by velocity rescaling for 50 picoseconds, while the MD box dimensions are adjusted by a Berensen barostat to maintain traction-free periodic boundary conditions in all three directions. Subsequently the temperature is maintained using a Nose-Hoover thermostat, while the Cu-Ag (Cu-Al) nanolayer model is subjected to a uniaxial tensile load by deforming the simulation box in the out-of-plane (x_2) direction at a fixed strain rate of 10^8 s^{-1}, while maintaining zero box pressure in the x_1 and x_3 directions. All the MD simulations are performed with a fixed time step of 1 fs, up to a strain of 10% strain in the x_2 direction. To verify the investigating deformation mechanisms are strain rate independent, tensile tests are performed at smaller strain rates of $10^7\ s^{-1}$and $10^6 s^{-1}$, where similar deformation behaviors are observed.

3.2 Planar-to-Wavy Transition of Cu-Ag Nanolayered Metals

Fig. 3.2a shows the uniaxial stress-strain response of Cu-Ag nanolayers with an interlayer thickness of $h = 2\ nm$ subjected to out-of-plane (x_2) tension. The "macroscopic" stress-strain

response is obtained by averaging the atomic virial stresses of Cu and Ag atoms over the entire deformed box volume [55]. The Cu-Ag nanolayers deform linear elastically prior to reaching a peak σ_{22} stress of $3.9GPa$ at $\varepsilon_{22} = 0.030$. Beyond this point, the stress-strain response becomes highly oscillatory up to $\varepsilon_{22} = 0.045$, at which point it maintains a steady stress level of $\sigma_{22} = 1.2GPa$.

Fig. 3.2b shows the atomic configurations of the Cu-Ag nanolayers at six specific loading instants (i) to (vi) marked in Fig. 3.2a; the atoms are filtered based on CSP value to display only the defects: interlayer interfaces and dislocations. Observe that the oscillatory response in the stress-strain curve coincides with the planar-to-wavy transition of the Cu-Ag nanolayers. The Cu-Ag nanolayers remain planar during the initial linear elastic deformation, but develop a slight perturbation at (i). From (i) to (ii), the Cu-Ag nanolayers abruptly transition to become wavy with amplitude of $\zeta = \sim 1.5h$, and wavelength λ corresponding to the in-plane box dimensions of $\sim 50nm$. Note that while the Cu and Ag interlayers are now wavy, the Cu-Ag interfaces remain(111). This planar-to-wavy transition is marked by a dramatic drop in σ_{22} from 3.9 GPa to 1.2 GPa. Under further loading, σ_{22} increases to reach a second peak of $3GPa$ at (iii), while the wavy amplitude of the Cu-Ag nanolayers decreases slightly to $\sim 0.75h$. At this juncture, the Cu-Ag nanolayers, although wavy, are still pristine and have no observable emitted dislocations.

From (iii) to (iv), σ_{22} drops to 1 GPa and the wavy amplitude increases to $\sim 1.5h$. Defects are now periodically emitted from the wavy summits and valleys of the Cu-Ag interfaces, as seen in (iv) and (v). Close-up view in (iv) shows that the initial defects comprise of $\frac{1}{6}\langle 112\rangle$ Shockley partials, which are emitted through the Cu interlayer; these defects originate from the Shockley partials bounding the triangular stacking faults near the summits or valleys of the Cu-Ag interface.

Subsequent emission of $\frac{1}{6}\langle 112\rangle$Shockley partials on adjacent slip planes leads to the development of two atom-thick micro-twins, as shown by the close-up view in (v). The transmission of deformation twins, through multiple Cu-Ag nanolayers, is facilitated by Cu-Ag interfaces and locks the shape of the wavy structure in (v). This locking is caused by local kinks along the wavy Cu-Ag interface created during the emission or transmission of twinning partials across the interface, which reorients the (111) Cu-Ag interface to another $\{111\}$plane [40, 56], as shown by the close-up view in (v). Note that previous study has shown that the rotation of the Cu-Ag interface to a $\{100\}$ plane after twin transmission across the interface is also possible [40, 57]. Once the deformation twins span across the full x_2 spatial dimensions of the periodic box in (vi), continued emission of twinning partials from the summits and valleys of the wavy interfaces causes the two atom-thick micro-twins to grow in thickness, and a constant stress level of $\sigma_{22} = 1GPa$ is maintained.

Fig. 3.3 shows the evolving Cu-Ag interface structure with deformation. For clarity, only the atomic layer of Cu and Ag atoms at the interface is displayed (Ag atoms on top, Cu atoms below) with the atoms colored by CSP values. A regular triangular network of $\frac{1}{6}\langle 112\rangle$Shockley partials is seen for the planar interface at $\varepsilon_{22} = 0.030$ in Fig. 3.3a. However, the transition of the interface from planar to wavy in Fig. 3.3b and 3.3c distorts this regular arrangement of Shockley partials. At the wavy summits, the triangular stacking faults bounded by Shockley partials become highly elongated and distorted with each stacking fault occupying an area 5 times larger than the original ones. At the wavy valleys, the density of Shockley partials is much higher; each triangular network of Shockley partials now bounds a smaller stacking fault area. The average density of Shockley partials across the wavy interface, however, remains the same prior to twin emission and transmission. These results imply that there is a redistribution of Shockley partials along the

interface from the wavy summits to the wavy valleys. At this point, the deformation process, while nonlinear, is still elastic, and the planar configuration can be recovered upon unloading of the nanolayers. Once micro-twinning partials are emitted and are transmitted through the interlayer interfaces, as in Fig. 3.3c and 3.3d, kinks in the interface structure are generated at the locations marked by yellow arrows; this deformation twinning process locks the wavy profile, and the structure remains wavy even upon unloading.

While oscillations in the stress-strain behavior of nanostructures are sometimes observed in MD simulations due to the non-uniform strain distribution in the structure resulting from high loading rates (e.g. [58]), the oscillatory stress-strain behavior of Cu-Ag nanolayers has a more physical basis. As will be shown by my analytical formulation in Section 3.5, the wavy state of the Cu-Ag nanolayers is energetically more favorable than the planar state, since the out-of-plane deformation of the wavy structure can be accommodated by interface sliding. However, interface sliding can only initiate, when a critical barrier stress is reached. Then, the almost instantaneous release of elastic strain energy due to the abrupt formation of these wavy structures triggers the oscillatory stress-strain response.

The formation of macroscale wavy structures, such as the buckling of multilayered composite plates or the surface wrinkling of thin films, is commonly caused by mechanical compression along the in-plane direction. The formation of wavy Cu-Ag nanolayers, on the other hand, is solely caused by out-of-plane tensile deformation: there are no external lateral stresses available to drive the planar-to-wavy transition of the nanolayers. The Poisson's ratio of the Cu-Ag nanolayers also does not play much of a role, since the periodic x_1 and x_3 simulation box boundaries are constrained to have zero average pressure. Instead, the planar-to-wavy transition is facilitated by the unique ability of the Cu-Ag interfaces to redistribute misfit Shockley partial

dislocations to reduce the bending energy. This process is very abrupt and the sudden release of elastic strain energy due to the lower energy state of the wavy nanolayers compared with its planar configuration causes the oscillatory stress-strain response seen in Fig. 3.2a. Although this planar-to-wavy interlayer transition mechanism is akin to grain boundary migration [59], no coarsening of the nanolayers is observed and the interlayer interfaces remain$\{111\}$. In addition, the planar-to-wavy transition is activated by energetics rather than thermal diffusion processes, and thus occurs well within MD time scales.

3.3 SFTs Formation along Cu-Al Interface

In contrast to the planar-to-wavy transition of Cu-Ag nanolayers, the Cu-Al interfaces remain planar throughout the uniaxial tensile deformation process. Instead, closed and open stacking fault tetrahedra (SFTs) are initiated from Cu-Al interlayer interfaces and completely envelope those interfaces. Fundamentally, SFTs are three-dimensional (3D) crystalline defects, which have been observed in FCC metals and alloys for over half a century [60-64]. A typical closed SFT comprises four intrinsic stacking faults planes intersecting along $\langle 110 \rangle$ edges to form a perfect tetrahedron. Such defects are commonly produced by irradiation [61, 62], ageing after quenching [63-65] or by plastic deformation [66]. One of the simplest mechanisms for SFT formation is by direct vacancy clustering, in which a small vacancy cluster serves as a nucleus and grows into a tetrahedron by absorption of vacancies along a jog line [67, 68]. Silcox and Hirsch proposed an alternative SFT formation mechanism [60], where vacancy clusters collapse to form a triangular faulted loop of $\frac{1}{3}\langle 111 \rangle$Frank partials bounding an intrinsic stacking fault; this faulted loop later dissociates into stair-rod and Shockley partials on the three inclined $\{111\}$planes to form

the SFT. In contrast to these vacancy-originated SFTs, dislocation-based SFTs have been observed as well in deformed metals [69, 70], where the triangular loops of Frank partials result from cross-slip of extended dislocations under plastic deformation. Somewhat less reported are open-ended SFTs where only three tetrahedron faces are stacking fault planes. Such open-ended SFTs have been previously seen in strained Si-Ge thin films grown by thermal chemical vapor deposition [71, 72]. The presence of closed or open-ended SFTs can obstruct the motion of dislocations and in turn induce significant changes to the mechanical properties of the material, such as strengthening, hardening and plastic instability during deformation [73, 74]. Here, a first observation of deformation induced closed and open-ended SFTs formation from Cu-Al interface is reported in my MD simulations.

Fig. 3.4a shows the stress-strain response of Cu–Al nanolayers, with interlayer thickness of $h = 4nm$. The Cu–Al nanolayers deform linear elastically up to $\varepsilon_{22} = 0.035$ where a kink in the stress–strain curve is observed, indicating the onset of yielding. Subsequent deformation results in appreciable strain hardening, and σ_{22} saturates at strains beyond$\varepsilon_{22} = 0.055$. Fig. 3.4b shows the cross-sectional views of the deformed atomic configurations at four instances (i)– (iv) marked in Fig. 3.4a, which are filtered to show only the non-FCC Al (yellow) and Cu (green) atoms in the structure. Both the Cu and Al interlayers remain defect-free during the initial elastic deformation. At $\varepsilon_{22} = 0.025$, a SFT develops within the Cu interlayer, with the base of the SFT located at a Cu–Al interface (Fig. 3.4b-i). The edge dimension of this SFT corresponds exactly to that of the partial misfit dislocations bounding the intrinsic stacking faults along the interface (edge length of ~2.3 nm), suggesting that the SFT nucleates from these partial misfit dislocations. The density of SFTs within the Cu interlayers increases with deformation and results in the strain hardening stress–strain response in Fig. 3.4a. At $\varepsilon_{22} = 0.050$, the density of SFTs in Cu reaches a maximum

(Fig. 3.4b-ii). Close examination shows the presence of several larger SFTs in Cu with edge length twice that of the more typical smaller SFTs. Beyond this point, SFTs now also develop within the Al interlayers (Fig. 3.4b-iii). Once the density of SFTs within the Al interlayers reaches a maximum (Fig. 3.4b-iv), the σ_{22} stress saturates at $\sim 4.1 GPa$. The triangular stacking faults along the interface (colored in blue in Fig. 3.1b) form the base of the SFTs in Cu, which are therefore closed SFTs. In contrast, the SFTs in Al are located on top of triangular FCC planes along the interface (colored in red in Fig. 3.1b) and are therefore open-ended SFTs. Fig. 3.4c displays the locations of SFTs at Cu-Al interface. Details of the formation mechanisms of these closed and open-ended SFTs are discussed below.

3.3.1 Closed SFT Formation in the Cu Interlayers

Fig. 3.5a and 3.5b shows the perspective and top views of the closed SFT formation process in Cu interlayers from partial misfit dislocations along the Cu–Al interface (stacking fault interface atoms on the side of Cu are colored in green). These results are obtained by conducting MD simulations for the $h = 4nm$ Cu–Al nanolayers at a relatively low temperature of $100K$ to reduce the thermal noise. The corresponding dislocation mechanisms are schematically shown in Fig. 3.5c using the Thompson's tetrahedron convention: A, B, C and D represents the four corners of the tetrahedron, while mid-points of the opposite faces of the tetrahedron are denoted by α, β, γ and δ, and the corresponding $\{111\}$ slip planes are denoted by a, b, c and d. The formation of closed SFTs in the Cu interlayers originates from the triangular intrinsic stacking faults along the (111) Cu–Al interface, each bounded by three edge-type $\frac{1}{6}\langle 112 \rangle$ partial misfit dislocations intersecting at 60°. Here, BCD represents a triangular intrinsic stacking fault along the interface,

while the partial misfit dislocations bounding this stacking fault prior to deformation are denoted by αB, αC and αD.

In the first snapshot, a Shockley partial γA, originating near the middle of αC along edge BD, is emitted along the slip plane c; the process leaves behind a stair-rod dislocation $\alpha\gamma$ at the interface. In the second snapshot, a second Shockley partial βA emerges along slip plane b, which transforms the partial misfit dislocation αB into a second stair-rod dislocation $\alpha\beta$ along DC. The two expanding Shockley partials (γA, βA) meet along the edge DA to form a stair-rod dislocation $\beta\gamma$, i.e.

$$\beta A + A\gamma = \beta\gamma \tag{3.1}$$

Concurrently, a third Shockley partial δA, originating from the remaining partial misfit dislocation αD, is emitted along the slip plane d, leaving behind a stair-rod dislocation $\alpha\delta$ along CB. The emitted Shockley partial δA grows and eventually intersects with the other two Shockley partials γA and βA on the inclined slip planes c and b, respectively, to form stair-rod dislocations ($\delta\beta$, $\gamma\delta$) along CA and BA, i.e.

$$\delta A + A\beta = \delta\beta \tag{3.2}$$

$$\gamma A + A\delta = \gamma\delta \tag{3.3}$$

The resulting dislocation structure is now a closed SFT, comprising of four intrinsic stacking fault planes (one along the interface) which are bounded by six stair-rod dislocations: three along the interface($\alpha\gamma, \alpha\beta, \alpha\delta$), which are formed during the emission of Shockley partials, and the other three on the inclined edges ($\beta\gamma, \delta\beta, \gamma\delta$)formed from interaction of the emitted Shockley partials.

3.3.2 Open-ended SFT Formation in the Al Interlayers

The formation of closed SFTs prevents further sliding between atomic planes within the Cu interlayers, thus causing the nanolayers to undergo strain hardening (Fig. 3.4a). Once the closed SFTs within the Cu interlayers have completely enveloped the intrinsic stacking faults along the Cu–Al interface, further emission of dislocations into Cu is no longer possible. Instead, Shockley partials are now emitted into the Al interlayers despite the much higher intrinsic stacking fault energy of Al ($\gamma_{Al} = 146mJ/m^2$) compared to Cu ($\gamma_{Cu} = 44mJ/m^2$). Fig. 3.6 shows the perspective (Fig. 3.6a) and top view (Fig. 3.6b) atomic configurations of this SFT formation process in the Al interlayers, as viewed from the side of Al (Cu and Al stacking fault interface atoms are colored in green and yellow, respectively). Observe that the emitted Shockley partials travel along the same inclined $\{111\}$ planes as in the closed SFT formation process, but in the opposite direction into the Al interlayers. The Shockley partials interact along the $B'A'$, $C'A'$ and $D'A'$ edges of the tetrahedron to form, $\frac{1}{6}[0\bar{1}\bar{1}]$, $\frac{1}{6}[\bar{1}\bar{1}0]$ and $\frac{1}{6}[\bar{1}0\bar{1}]$ stair-rod dislocations (Fig. 3.6c). The edges $B'C'$, $C'D'$ and $D'B'$ along the interface are already stair-rod dislocations, but they now enclose a triangular plane of atoms which have perfect FCC arrangement at the Cu–Al interface. Hence, the SFTs within the Al interlayers comprise only three inclined stacking fault planes and are considered open-ended.

3.3.3 Large-dimension SFT Formation in the Cu Interlayers

The MD simulations presented in this section thus far are conducted under fixed temperature of 100 K; the edge dimensions of both the closed and open-ended SFTs approximately correspond to that of the triangular stacking faults along the Cu–Al interface. Under a temperature of 300 K, however, larger-dimension (LD-) SFTs with edge length twice that of the interface

stacking faults can also form in Cu (see Fig. 3.4b-iii and 3.4b-iv)). MD simulations show that these LD-SFTs actually develop from the smaller SFTs in the Cu interlayers. Fig. 3.7a and b shows the perspective and top views of the formation process of a typical LD-SFT in Cu with atoms are colored in the same manner as in Fig. 3.5. While Fig. 3.7c shows the cross-sectional views of the atomic configurations along specific cuts A–A, B–B and C–C in Fig. 3.7b with atoms are colored by CSP values. The detailed mechanisms of the LD-SFT formation process corresponding to each snapshot in Fig. 3.7a and 3.7b are schematically illustrated in Fig. 3.8; the superscripts I, II and III are used to denote the burgers vectors associated with the smaller SFTs and are dropped for the burgers vectors of the LD-SFT.

The formation process of the LD-SFT begins with the dissociation of the stair-rod dislocation $\delta\beta^I$ back into its Shockley partial components: $A\beta^I$and δA^I ((ii) in Fig. 3.7a/3.7b/3.8). The Shockley partial δA^I retracts back to the interface and reforms the partial misfit dislocation αD^I bounding the interface stacking fault, as well as the inclined Shockley partial γA^I. Both the Shockley partials $A\beta^I$ and γA^I grow and intersect to form a stair-rod dislocation $\beta\gamma$ of the LD-SFT at one end, while concurrently advancing across the interface triple junction points at the other end (snapshot). Once $A\beta^I$ and γA^I approach SFT II and III, respectively, the stair-rod dislocations $\beta\gamma^{II}$ and $\beta\gamma^{III}$ dissociate into their respective Shockley partials ($A\beta^{II}$, γA^{II}) and ($A\beta^{III}$, γA^{III}). The Shockley partials $A\beta^{II}$ and γA^{III} merge with the expanding Shockley partials $A\beta^I$ and γA^I to form $A\beta$ and γA of the LD-SFT ((iii) and (iv) in Fig. 3.7a/3.7b/3.8). Concurrently, the Shockley partials γA^{II} and $A\beta^{III}$ retract to the Cu–Al interface to reform the partial misfit dislocations αC^{II} and αB^{III} bounding the interface stacking faults of II and III; the process also removes the stair-rod dislocations $\gamma\delta^{II}$ and $\delta\beta^{III}$ and reforms the Shockley partials δA^{II} and δA^{III} which merge to form δA of the LD-SFT ((v) in Fig. 3.7a/3.7b/3.8). Finally, the Shockley partials $A\beta$, γA and δA

completely intersect to form the stair-rod dislocations, $\delta\beta$, $\beta\gamma$ and $\gamma\delta$ bounding the inclined stacking fault planes of the LD-SFT ((vi) in Fig. 3.7a/3.7b/3.8). Note that the LD-SFT is a partially closed SFT since it forms across both the triangular planes of stacking faults and perfect FCC atoms along the Cu–Al interface. Due to the higher temperature of 300 K, the closed SFTs, which first develop along the Cu–Al interface, may not be perfectly aligned and may result in the formation of ledges on the inclined faces of the LD-SFT as shown clearly in the cross-sectional view C–C in Fig. 3.7c. The entire LD-SFT formation process occurs within $1.22ps$ after the initial development of the three closed SFTs along the Cu–Al interface. As can be seen in the formation process, the development of these LD-SFTs requires sufficient thermal energy to dissociate the existing stable stair-rod dislocations of the smaller closed SFTs into their Shockley partial components. Therefore, they are not observed at lower temperatures of 100 K. In addition, such LD-SFTs do not form within the Al interlayers even at 300 K, presumably because of the high stacking fault energy of Al compared to Cu, as well as the high barrier energy required to dissociate the stair-rod dislocations within Al to reform the curved stacking fault atomic structure along the Cu–Al interface.

3.4. Interface Mechanisms versus Shear Resistance

The contrasting deformation mechanisms in Cu-Ag and Cu-Al nanolayers is associated with the shear resistance along the respective interfaces. Fig. 3.9 compares the generalized stacking fault energy (GSFE) γ_s for sliding along the (111) Cu–Ag interface versus the (111) Cu-Al interface. The GSFE surface is obtained by rigidly displacing two halves of a (111) bicrystal Cu–Ag (Cu-Al) structure in both the $[\bar{1}10]$and $[11\bar{2}]$directions at small increment each step and

calculating the energy values. Fig. 3.9a shows the GSFE surface of Cu-Ag interface. In Fig. 3.9b and c, the GSFE γ_s for relative sliding between the Cu and Ag interlayers along the $\langle 110 \rangle$ and $\langle 112 \rangle$pathways is presented in solid lines. By taking the gradient of γ_s along both directions, the associated shear strength τ_s for interface sliding, is obtained and shown as dashed line in Fig. 3.9b and 3.9c. For comparison, the GSFE γ_s and associated shear strength τ_s along the $\langle 110 \rangle$ and $\langle 112 \rangle$ pathways for Cu-Al interface are displayed in Fig. 3.9d and 3.9e.

Observe that, in the Cu-Ag interface, although the critical barrier strength for interface sliding along $\langle 112 \rangle$is almost the same as along $\langle 110 \rangle$, the barrier energy for sliding is higher by 10%. the lowest energy pathway for relative sliding between the Cu and Ag interlayers is the $\langle 110 \rangle$direction, which is different from the conventional $\langle 112 \rangle$ pathway for partial dislocation slip in an FCC crystal. This has been confirmed by tracing the relative motions of Cu and Ag atoms along the interface from the MD simulations in Fig. 3.10. A cross row of Ag atoms along the interface is highlighted in green, while a similar cross row of Cu atoms along the interface is highlighted in yellow. As shown, the relative motion of the highlighted Cu and Ag atoms is consistently along the close-pack $\langle 110 \rangle$ direction, as denoted by red arrows.

In contrast, the critical barrier stress, as well as barrier energy, in Cu-Al interface are twice as high as that in Cu-Ag interface (almost $6GPa$) in both $\langle 112 \rangle$ and $\langle 110 \rangle$ directions. This could be due to the strong bonding effect between Cu and Al atoms. As a result, the sliding of Cu-Al interface is extremely difficult and the Cu-Al nanolayers will remain planar throughout the deformation process. Instead, the unique Cu-Al interface structure caused by strong bond between the two atoms leads to Shockley partial emission from Cu-Al interface that produce SFTs.

3.4.1 Sliding along Cu-Ag Interface

The interface sliding between Cu and Ag interlayers along $\langle 110 \rangle$ direction is accompanied by the redistribution of Shockley partials. To quantify this relationship, a $[11\bar{2}]$ cross sectional view of the Cu-Ag interface is examined in Fig. 3.11a, which is filtered to include four layers of Ag atoms (top) and four layers of Cu atoms (bottom). I trace the $[1\bar{1}0]$motion of several groups of atoms labelled A, B and C along the interface, each group comprising of eight Ag atoms and nine Cu atoms, which are colored in green and yellow, respectively. Within each group, the Ag and Cu atoms will approximately span the same spatial extent along a planar Cu-Ag interface as shown for $\varepsilon_{22} = 0.030$. A close up view of these individual groups of atoms is presented in Fig. 3.11b. Note that groups A, B and C reside at the valley, incline and summit positions along the wavy profile at $\varepsilon_{22} = 0.040$, which represents the final "locked" wavy configuration after the emission and transmission of micro-twinning partials across the interlayers. Observe that there is significant relative sliding between the Ag and Cu atoms along an inclined section of the evolving wavy profile, but the relative sliding between these Cu and Ag atoms at the wavy summit or valley is small. At $\varepsilon_{22} = 0.034$, for example, atoms in groups A and C are at a wavy incline and undergo significant relative sliding of almost 2-3 atomic spacing of Cu along $[1\bar{1}0]$, but atoms in group B are positioned near the valley of the wavy profile and slide by approximately one atom spacing. At $\varepsilon_{22} = 0.040$, the Cu atoms in group B slide by almost two atomic spacing towards the valley with respect to the Ag atoms, while almost no sliding occurs between the Cu and Ag atoms in groups A and C.

Close examination shows that the Ag atoms (green) are packed closer together and the Cu atoms (yellow) are spaced further apart at the summit, while the trend is reversed at the valley. To clarify this point, Fig. 3.11c and 3.11d shows the distribution of the spacing between Shockley

partials d and the local density of Shockley partials $\rho = 1/d$ along the wavy interface for the four wavy configurations above. Each symbol in the figure represents a single Shockley partial along the interface. Note that the total number of Shockley partials along the interface remains the same during the wavy transition. In addition, the densely-packed Shockley partials reside close to the valley of the wavy interface (in-between atoms in groups A and B), while sparsely distributed Shockley partials are located near the summit (close to atoms in group C). This is attributed to the development of high in-plane tensile stresses at the outer bends of the wavy profile, and high in-plane compressive stresses at the inner bends. These bending stresses are significantly reduced by the motion of misfit Shockley partials along the interface, as seen by the relative sliding of Cu atoms from the summits towards the valleys, and are further relaxed by the subsequent emission of Shockley (and subsequently micro-twinning) partials from the valleys and summits at $\varepsilon_{22} = 0.040$.

Fig. 3.12 traces the evolution of the in-plane σ_{11} stress as the wavy profile develops for the three specific groups of Cu and Ag interface atoms, A, B and C highlighted in Fig. 3.11. The evolution of σ_{11} with deformation is obtained by averaging the atomic σ_{11} virial stress values of the Cu or Ag atoms within each group every 1ps. For the planar nanolayers, the σ_{11} stress component only has contribution from the coherency stress, which remains constant. Note that the coherency stress is not uniform across the different groups of atoms, since it varies periodically along the Cu-Ag interface depending on the proximity of the different groups to the triangular network of Shockley partials along the interface. Once the nanolayers become wavy at $\varepsilon_{22} = 0.040$, σ_{11} now mainly reflects the in-plane bending stress contribution which evolves with the wavy profile. My results show that high σ_{11} tensile stress consistently develops for the interface atoms at the outer bends, while interface atoms at the inner bends undergo high σ_{11} compressive

stress. On the other hand, atoms along the incline do not undergo bending, and therefore have $\sigma_{11}\sim 0$. Observe that the Cu and Ag interface atoms in the group A (Fig. 3.12a) experience the highest magnitude of σ_{11} stress among all three groups of atoms: the localized and sustained bending stress of $\sigma_{11} = \pm 10\sim 15GPa$ at applied strains of $0.036 \leq \varepsilon_{22} \leq 0.038$ results in the emission of micro-twinning partials at group A, which subsequently relaxes the σ_{11} stress to ± 5GPa.

As previously shown in Fig. 3.2a, the abrupt transition of the Cu-Ag nanolayers from planar to wavy at the critical strain of $\varepsilon_{22} = 0.030$ is demarcated by a sharp drop in the stress carrying capacity, from 3.9 to $1.2GPa$. This 3- to 4-fold loss of stress carrying capacity is associated with sliding between the wavy Cu and Ag interlayers to accommodate the out-of-plane deformation in the x_2 direction. For the Cu–Ag nanolayers subjected to uniaxial tension, the total u_2 displacement caused by the stretching of an interlayer interface bounded by a Cu nanolayer of thickness $h/2$ and an Ag nanolayer of thickness $h/2$ is given by $\varepsilon_{22}h$. This u_2 displacement can be delineated into the elastic stretching contributions of the Cu and Ag nanolayers, given by $\frac{\sigma_{22}h}{2E_{Cu}}$ and $\frac{\sigma_{22}h}{2E_{Ag}}$, respectively, as well as the cohesive separation of the Cu–Ag interface in the x_2 direction due to interface slip denoted by δ_2. Then, the effective secant modulus defined by $E = \frac{\sigma_{22}}{\varepsilon_{22}}$ can be expressed as follows:

$$\frac{1}{E} = \frac{1}{2E_{Cu}} + \frac{1}{2E_{Ag}} + \frac{\delta_2}{E\varepsilon_{22}h} \tag{3.4}$$

Prior to the critical strain of $\varepsilon_{22} = 0.030$ in Fig. 3.2a, the Cu–Ag nanolayers remain planar and deform linear elastically with an elastic (secant) modulus of $E = 130GPa$. Taking the elastic modulus of Cu and Ag to be $E_{Cu} = 168GPa$ and $E_{Ag} = 124GPa$, respectively, $\delta_2 = 0.002h$ is

obtained from (3.4). This small cohesive separation confirms that the deformation process of the planar Cu–Ag structure is dominated by elastic straining of the individual Cu and Ag interlayers, while the Cu–Ag interfaces are essentially rigidly bonded. When the interlayers transits to become wavy, the effective secant modulus E now drops to $35GPa$. Assuming that the elastic modulus of the rotated Cu and Ag interlayers do not deviate significantly from the values for E_{Cu} and E_{Ag} above, then $\delta_2 = 0.02h$ is obtained for the wavy nanolayer interface in (3.4); this cohesive separation of the wavy interface is an order of magnitude larger than the cohesive separation for the planar nanolayer interface. At this juncture, the interlayer interface away from the summits and valleys is now inclined at an angle of $\theta = 18°$ relative to the initial planar configuration. See wavy profile for $\varepsilon_{22} = 0.034$ in Fig. 3.11a. The average relative sliding between the Cu and Ag interlayers along the wavy interface is $\delta_t = \frac{\delta_2}{\sin\theta} = 0.17nm$, which is in good agreement with the MD simulation results.

The planar-to-wavy transition abruptly initiates at a critical stress level of $\sigma_{22} = 3.9GPa$. At this stress level, a slight perturbation develops along the interlayers, which rotates the planar Cu-Ag interface by $\sim 5°$ near the atoms in group C as seen in Fig. 3.11a. Then, the external loading effectively generates a resolved shear stress of $\sim 0.3\ GPa$, which combined with the coherency stress of $\sim 2.5\ GPa$ for this group of atoms (Fig. 3.12c) will be sufficient to overcome the $2.8\ GPa$ barrier strength for interface sliding along the $\langle 110 \rangle$ pathway. Once this critical process is initiated, localized tensile and compressive in-plane stresses induced by bending at the wavy summits and valleys will drive the redistribution of misfit dislocations along the interface.

Observe that interface sliding and the redistribution of misfit dislocations are intimately connected. In conventional engineering structures, the interlocking nature of wavy interfaces will

usually prevent sliding [75]. For the Cu–Ag wavy nanolayers, the presence of misfit partials along the semi-coherent interface provides a novel mechanism for sliding. Along each wavy interface, the atoms in the outer bends of the interface experience tension, while atoms in the inner bends undergo compression. Then, the initial uniform distribution of misfit dislocations along the planar configuration no longer becomes ideal, once the nanolayers transition to become wavy. Instead, there is now a driving force for the motion of these misfit dislocations from the inner bends to the outer bends along the interface through interface sliding to relieve the build-up of tensile or compressive stresses at the summits and valleys of the wavy interface. See schematic in Fig. 3.13. This explains the relative sliding between Ag and Cu atoms along the interlayer interface in Fig. 3.11, which essentially occurs to increase the density of Cu atoms at the valley (outer bend), and at the same time to reduce the density of Cu atoms at the summit (inner bend).

3.4.2 Shockley Partial Emission from Cu-Al Interface

Consider the Cu-Al interface under the same uniaxial tensile load, Fig. 3.14 shows the $[1\bar{1}0]$ cross-sectional view of the closed SFT formation process taken along section A–A in Fig. 3.1b. The core of the misfit partial (yellow dashed circle in Fig. 3.14a) has a unique structure. While under uniaxial tension, high resolved shear stress along the $[110]$ direction develops near the dislocation core. Once the resolved shear stress reaches a critical value of $\sim 2\ GPa$, it causes the emission of a perfect $\frac{1}{2}[110]$ dislocation (DA), which interacts with the $\frac{1}{6}[\bar{1}\bar{1}2]$partial misfit dislocation$(\alpha D)$to form a $\frac{1}{6}[110]$ stair-rod dislocation $(\alpha\delta)$ along the interface and to emit a $\frac{1}{6}[112]$ Shockley partial (δA) along the $[11\bar{1}]$slip plane (d) (Fig. 3.14b and 3.14c).

$$\frac{1}{6}[\bar{1}\bar{1}2]+\frac{1}{2}[110]=\frac{1}{6}[110]+\frac{1}{6}[112]$$

$$\alpha D + DA = \alpha\delta + \delta A \tag{3.5}$$

Similar emissions of perfect dislocations (BA, CA) interacting with the partial misfit dislocations (αB, αC) lead to the formation of Shockley partials (βA, γA) on the other two inclined b and c slip planes, leaving behind stair-rod dislocations ($\alpha\beta$, $\alpha\gamma$) along the Cu–Al interface. The interaction between the Shockley partials βA, γA later form the stair-rod dislocation ($\beta\gamma$), as marked in Fig. 3.14d. Note that the Shockley partials (βA, δA, γA) are consistently emitted near the middle of the partial misfit dislocations (αB, αC, αD), rather than near the triple junction sites where there is equal probability of dislocation slip in all three inclined $\{111\}$ planes.

In the Al interlayers, the Shockley partials are concurrently emitted from all three stair-rod dislocations bounding the perfect FCC triangular planes of atoms along the interface, rather than the sequential emission process for the closed SFTs in Cu (compare Fig. 3.5 and 3.6). To explain this phenomenon, the $[1\bar{1}0]$cross-sectional view of the open-ended SFT formation process is examined in Fig. 3.15 taken along section A–A in Fig. 3.1b. Observe in Fig. 3.15a, the stacking fault planes along the Cu–Al interface are slightly curved once the closed SFTs have formed in Cu, compared to the originally flat stacking fault planes of SFTs in bulk Cu. This slightly curved stacking fault plane along the Cu–Al interface is probably due to the $\sim$12% larger lattice constant of Al compared to Cu and strong bond between Cu and Al atoms at the core of each stair-rod dislocation along the interface (yellow arrow in Fig. 3.15a). With continued deformation, Shockley partials ($\frac{1}{6}[\bar{1}\bar{1}\bar{2}]$ in the cross-sectional view of Fig. 3.15b and c) are emitted from this initial gap and transmitted into the Al interlayer. This process significantly reduces the curvature of the interface stacking fault (Fig. 3.15c and d). The resulting dislocation structure now comprises a corrugated sheet of closed and open-ended SFTs on the sides of Cu and Al, respectively, which

completely envelopes the entire Cu–Al interface (Fig. 3.15d). The formidable locks posed by the stair-rod dislocations on these closed and open-ended SFTs prevent the further emission of dislocations from the Cu–Al interface into either the Cu or Al interlayers.

The same Cu–Al nanolayers models are also subjected to in-plane equal-biaxial compression while maintaining stress-free periodic boundary conditions in the out-of-plane direction. Again, closed and open-ended SFTs along the Cu–Al interfaces ae formed by the same mechanisms discussed above. This observation is attributed the Poisson's ratio effect, which induces an out-of-plane stretch during in-plane compression. Conversely, my simulations show that SFTs do not form under in-plane tension or out-of-plane compression, since these deformation states are more likely to generate extrinsic rather than intrinsic stacking faults [76]. Theoretically, such extrinsic stacking faults can lead to the formation of extrinsic SFTs which are interstitial-based, but no experimental or atomic simulation evidence currently exists for the formation of these extrinsic SFTs. In the presence of an interstitial rich environment, e.g. during ion irradiation processes, the interstitials tend to group together to form prismatic dislocation loops rather than extrinsic SFTs [77].

The closed SFTs in Cu that develop along the Cu–Al interfaces have edge lengths of $\sim 2.3nm$, which are close to the edge dimensions of the triangular stacking faults that form along the semi-coherent Cu–Al interface. Early studies proposed that the stacking fault energy of a FCC metal can be inversely determined from the typical size of the SFT present in the bulk metal [69]. While this correlation has been a source of debate [70], it suggests that the stable size of the SFT is uniquely dependent on the type of FCC metal. Therefore, in order for closed SFTs to first develop within the Cu interlayers, the size of the triangular stacking fault along the Cu–Al interface should be on the same order of the stable size of the SFT in bulk Cu. Experiments show that the

SFTs in bulk Cu have edge length of $\sim 2.0nm$ [73, 78], which is indeed comparable to the $\sim 2.3nm$ edge dimensions of the intrinsic triangular stacking fault along the Cu–Al interface. On the other hand, SFTs in bulk Al metals are only observed under extreme conditions, due to the large stacking fault energy of Al, and have edge lengths over $\sim 90nm$ [79]. In comparison, the open-ended SFTs within the Al interlayers have edge lengths of $\sim 2.6nm$, since they are a consequence of the formation of closed SFTs within the Cu interlayers.

3.5. Competing Length-Scale Effects

3.5.1 Interlayer Thickness versus Wavelength of the Wavy Cu–Ag Nanolayers

For the planar-to-wavy transition to occur in Cu-Ag nanolayers, two necessary conditions are that (a) the Cu–Ag nanolayers structure has to overcome the barrier energy strength for interface sliding to initiate the transition, and (b) the wavy Cu–Ag nanolayers configuration has to be energetically more stable than the planar configuration at the critical strain. From MD simulations, the former process is achieved at a critical strain of$\varepsilon_{22} = 0.030$. As to the later process, consider the configurational energy change between a wavy Cu–Ag nanolayers structure and a planar nanolayers structure subjected to uniaxial tensile stress at the same applied strain:

$$dU_{tot} = d\left(U_{interface} + U_{elastic} + U_{bend}\right) \tag{3.6}$$

, where $U_{interface}$ is the Cu–Ag interlayer interface energy, and $U_{elastic}$ and U_{bend} are the internal elastic strain energies of the nanolayers associated with out-of-plane tensile stress and bending. While the actual wavy profile of the nanolayers is three-dimensional, for simplicity, a two-dimensional (2D) approximation is present here, while each energy contribution in (3.6) is

normalized by the volume to obtain the energy density. The individual energy density contributions are separately considered to the total energy density dU_{tot} below.

The transition of the initially planar Cu–Ag nanolayers to become wavy extends the area of the interface, and thus increases the interface energy. Throughout this transition, results in Fig. 3.2 show that the wavy interlayer interface still remains(111). While the local density of misfit partials varies along the wavy interface, the average density of misfit dislocations within one wavelength period λ remains the same as the initially planar configuration (Fig. 3.11d), implying that the wavy interface comprises of the same number of Cu–Ag atoms at least prior to the emission and transmission of micro-twinning partials. As such, the interfaces can be treated as being elastically stretched to fit the contoured wavy shape. For simplicity, the contours of the wavy interfaces can be approximated by interconnecting straight line segments joining the summits and the valleys, each line segment of length $\sqrt{(2\zeta)^2 + (\lambda/2)^2}$. Since the wavy amplitude$\zeta \ll \lambda$, the interface extends by $\sim 8\zeta^2/\lambda$ per wavelength λ, and the approximate increase in interface energy density can be expressed as:

$$dU_{interface} = 8\tau \frac{\zeta^2}{\lambda^2 h} \tag{3.7}$$

, where $\tau = \gamma + A\left(\frac{\partial \gamma}{\partial A}\right)$ represents the energy required to increase the interface area while keeping the number of atoms along the interface constant, γ is the interface energy and A is the area of the interface. For the {111} Cu–Ag interlayer interface, $\tau = 0.32 mJ/m^2$[80]. Due to the low shear resistance of the interface between the Cu and Ag nanolayers, the planar-to-wavy transition of the Cu–Ag nanolayers allows a large part of the deformation to be accommodated by interface sliding, which explains the significant loss of stress carrying capacity from $\sigma_{22}^{(i)} = 3.9$ to $\sigma_{22}^{(ii)} = 1.2GPa$. At this point, the Cu and Ag nanolayers are still free of dislocation or twinning defects, and behave

linear elastically with strain energies of $\frac{(\sigma_{22})^2}{2E_{Cu}}$ and $\frac{(\sigma_{22})^2}{2E_{Ag}}$, respectively, thus the elastic energy change is:

$$dU_{elastic} = \frac{\left(\sigma_{22}^{(ii)}\right)^2 - \left(\sigma_{22}^{(i)}\right)^2}{2}\left(\frac{1}{E_{Cu}} + \frac{1}{E_{Ag}}\right) \tag{3.8}$$

The bending energy associated with the valleys and summits of the wavy nanolayers can be approximated by the bending energy of a thin-laminated flat plate [81], and has the form:

$$dU_{bend} = \alpha \frac{h^2 \zeta^2}{\lambda^4} \tag{3.9}$$

, where α is a function of both E_{Cu} and E_{Ag}, and is calculated to be $\alpha = 14.3\ keV/nm^3$. Note that dU_{bend} represents an upper bound approximation, which correctly captures the bending energy contributions in the separate Cu and Ag interlayers, but does not account for the effects of interface sliding.

For the planar-to-wavy transition of the Cu–Ag nanolayers to be energetically favorable, the change in energy density in (3.6) must be negative, i.e. $dU_{tot} < 0$. For any waviness effects to be appreciable, the wavy amplitude must be of the order of the interlayer thickness. Assuming $\zeta \approx h$ and $\lambda \gg h$, then $dU_{interface}$ in (3.7) scales with the order of h/λ^2 and will be very small compared with the other two terms in (3.8) and (3.9) and may be neglected for simplicity. As such, the planar-to-wavy transition will mainly be governed by the competition between (a) the relaxation of out-of-plane σ_{22} stress due to the loss of strain energy ($dU_{elastic}$), and (b) the build-up of in-plane σ_{11} stress associated with bending at the summits and valleys of the wavy nanolayers (dU_{bend}). The former is sensitive to the interfacial properties (γ_s and τ_s), while the latter scales with order of $(h/\lambda)^4$. Should sliding along the Cu and Ag interlayers be permitted,

then the wavelength of the wavy nanolayers λ will directly scale with the interlayer thickness h. A series of MD simulations on Cu-Ag nanolayers with simulation box sizes of $Xnm(x_1)\times 16nm(x_2)\times 8nm(x_3)$ are also performed, where the simulation box size in the x_3 direction is intentionally reduced to trigger a 2D wave response in the $x_1 - x_2$ plane to be comparable with the 2D formulation developed above. The results from these simulations, together with the corresponding analytical predictions, are summarized in Table 3.1. Note that the critical wavelength λ must be smaller than the lateral simulation box dimensions X, in order for the planar-to-wavy transition to be triggered due to the enforced model periodicity. In addition, the wave number k will be integer multiples of X/λ. The MD simulations show that both ζ and $dU_{elastic}$ are independent of h, within the range of h values considered; the critical h/λ is also found to range from 0.04 to 0.05, which is in good agreement with upper bound analytical predictions of $\frac{h}{\lambda} = \sim 0.065$ based on (3.6) to (3.9).

Once the Cu–Ag nanolayers become wavy, high stress concentrations develop at the periodic wavy valleys and summits, which become the sources for the emission of Shockley partials. While Ag has a sufficiently low stacking fault energy that it can provide copious amounts of partial dislocation content in the bulk for twinning of Cu–Ag eutectic composites with interlayer thickness in the submicron regime ($> 100\ nm$) [2, 82], the interfaces become the main source of twinning partials for nanolayers with an interlayer thickness of tens of nanometers or smaller. Then, the wavelength λ of the wavy Cu–Ag nanolayers controls the density of twinning sources, and becomes an additional length scale for controlling the dissipation of plasticity. Since λ scales with h, reducing the interlayer thickness increases the density of twinning sources in a wavy structure, which promotes the earlier onset of plastic yielding. This mechanism could explain why certain nanolayers, including Cu–Ag, do not exhibit continuous strengthening with decreasing interlayer

thickness, but show saturation or decreasing yield strength (i.e. inverse "Hall-Petch" behavior) with decreasing thickness below $h \sim 5nm$ [13, 34]. In this regard, TEM imaging of eutectic Cu–Ag nanolayers is reviewed again (Fig. 2.4). Kingstedt et al. showed that the Cu–Ag nanolayers could transform from an initially parallel orientation to one that has a significant curvature without delamination under a multiaxial stress state [38]. Their observed planar-to-wavy transition of the Cu–Ag nanolayers with deformation is uncannily similar to the results of my MD simulations. In fact, these wavy nanolayers have a wavelength of $\lambda = 200nm$ with an interlayer thickness of $h = 20nm$, giving a $h = k$ ratio of 0.1 which is of the same order, as that predicted by both my MD simulations and analytical model.

3.5.2 Interlayer Thickness versus Size of SFTs in Cu–Al Nanolayers

With the presence of closed and open-ended SFTs, the strength of the Cu–Al nanolayers will be dependent on two competing length-scales: the interlayer thickness h and the size of the SFTs that develop in interlayers. Fig. 3.16a shows the stress–strain response for Cu–Al nanolayers of varying interlayer thicknesses ($h = 2, 3, 4, 6, 8, 10$ and $16nm$) subjected to out-of-plane uniaxial tension, conducted at a fixed temperature of $300K$. These Cu–Al nanolayers are constrained to have the same ($x_1 \times x_3$) in-plane model dimensions of $13.8 \times 19.9\ nm^2$, with out-of-plane dimensions of $16h$, $12h$ and $8h$ for $h = 2, 3\ and\ 4nm$, respectively, and $4h$ for larger interlayer thicknesses. Results show a sharp transition in the stress–strain behaviors of these Cu-Al nanolayers at interlayer thicknesses between 4 and 6 nm. Specifically, the nanolayers with $h \leq 4\ nm$ undergo substantial post yield strain hardening, while those with $h \geq 6nm$ exhibit a sudden drop in σ_{22} followed by a steady σ_{22} response. Note that the latter's post-yield response is typical

of the sudden release of dislocations within the initially pristine structure to accommodate the deformation, and the stress-state after dislocation emission is representative of the yield stress [12].

Fig. 3.16b summarizes the yield stress σ_y as a function of interlayer thickness h, taken at the strain of$\varepsilon_{22} = 0.065$ where the flow stress for $h \geq 6nm$ reaches a steady value. Interestingly, σ_y remains almost constant at $\sim 2 - 2.5GPa$ for $6 \leq h \leq 16nm$, but suddenly increases to $4GPa$ at $h = 4\,nm$. The yield stress decreases slightly to 3.8 GPa for $h = 3\,nm$ and to $\sim 3.1GPa$ for $h = 2nm$, indicating that the Cu-Al nanolayers with interlayer thickness of $h = 4\,nm$ represents the optimal configuration to achieve the highest possible strength.

To explain this trend, Fig. 3.17 compares the post-yielding atomic configurations of all seven interlayer thicknesses taken at a fixed strain of $\varepsilon_{22} = 0.065$. Observe that a corrugated sheet of closed and open-ended SFTs completely envelops the interface at the optimal interlayer thickness of $h = 4\,nm$; the deformed configuration has the highest volumetric density of SFTs (both closed and open-ended) possible within the nanolayers structure. As aforementioned, the formation of these SFTs prevents further dislocation slip and results in considerable strain hardening, as seen in Fig. 3.16a. For Cu–Al nanolayers with h = 3 nm, dual rows of closed SFTs still form within each Cu interlayer, but the reduced interlayer spacing now places the apex of these SFTs in close-proximity to each other. On the other hand, only a single row of complete open-ended SFTs now form within each Al interlayer, with apexes sometimes alternating upwards and downwards. This difference is due to the $\sim 12\%$ larger lattice spacing of Al and consequently the $\sim 12\%$ larger SFTs in Al compared to Cu. Dislocation slip is still restricted by the presence of these SFTs, and the yield strength is slightly, albeit consistently, lower than that for $h = 4nm$ across the entire deformation range. At $h = 2nm$, complete SFTs can no longer form in either the Cu or Al interlayers, and Shockley partials originating from the interface can now be

transmitted across the interlayers. As a result, yielding of these nanolayers initiates at much lower strain of $\varepsilon_{22} = \sim 0.030$ compared to the thicker nanolayers. The consequent strain hardening for nanolayers with $h = 2\ nm$ in Fig. 3.16a results from obstruction of slip by the Cu–Al interfaces. At larger interlayer thicknesses of $h \geq 6\ nm$, both closed and open-ended SFTs still form initially along the interlayer interfaces. Since h is now more than four times larger than the height of the individual SFTs, the stair-rod dislocations bounding the stacking faults in the SFTs now dissociate at larger strains to permit the growth of Shockley partials within the interlayers to accommodate the deformation. The release of strain energy in the process results in the sudden drop in σ_{22}. For nanolayers with $h \geq 8\ nm$, the transmission of perfect dislocation loops (Orowan bowing) within the Al interlayers is also observed, due to the high stacking fault energy of Al [13].

3.6 Conclusion

In this part of my research, uniaxial tension tests are performed on Cu-Ag and Cu-Al nanolayered metals using MD simulations. A novel mechanism responsible for the abrupt transition of the initially planar nanolayers to become wavy is uncovered for Cu-Ag nanolayered metals. Activation of this planar-to-wavy interlayer transition mechanism is facilitated by the unique structure of the semi-coherent Cu–Ag interface, which permits sliding between the Cu and Ag interlayers to simultaneously accommodate the out-of-plane deformation and redistribute misfit dislocations to relax the bending stress associated with the wavy structure. This mechanism can potentially explain the formation of some of the wavy Cu–Ag nanolayer patterns observed experimentally. For Cu-Al nanolayered metals, the study provides the first direct evidence of open and closed SFT formation along the interlayer interfaces. The formation of such 3D volumetric

structures along the semi-coherent interfaces has been previously postulated but never proven before. Unlike typical SFTs which form by vacancy clustering, the SFTs along the Cu-Al interlayers originate from the concurrent nucleation of Shockley partials from the dissociated misfit dislocations under tensile deformation. The final dislocation network comprises of closed SFTs within the Cu interlayers which are tied across the Cu–Al interfaces to open-ended SFTs within the Al interlayers. This network of SFTs completely envelops the Cu–Al interfaces and induces significant strain hardening of the Cu–Al nanolayered metal. Uncovering this interface-based SFT formation mechanism can provide insights to explain the role of misfit dislocations in the formation of SFTs in other bicrystal structures, such as the open-ended SFTs in epitaxial layers of $Si_{0.85}Ge_{0.15}$ grown on $\{111\}$Si substrates.

3.7 Figures and Tables

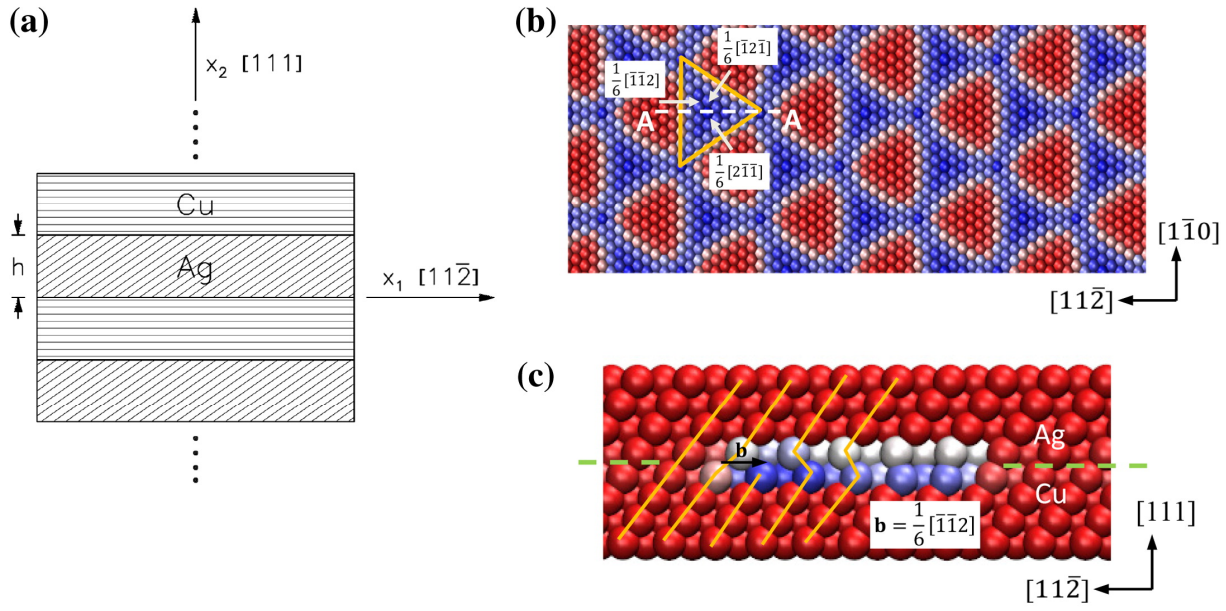

Figure 3.1 (a) Schematic of a periodic bimetal Cu–Ag (Al) nanolayers. (b) Top view of the Cu atoms along the interface showing the triangular network of Shockley partials bounding stacking faults. The atoms are colored according to their CSP values: FCC atoms are in red, dislocation cores in white and stacking faults in blue. Burgers vectors of the Shockley partials bounding the triangular stacking faults are as indicated. (c) Cross-sectional view of the Cu–Ag (Al) interface corresponding to an A–A cut along the dashed lines in (b).

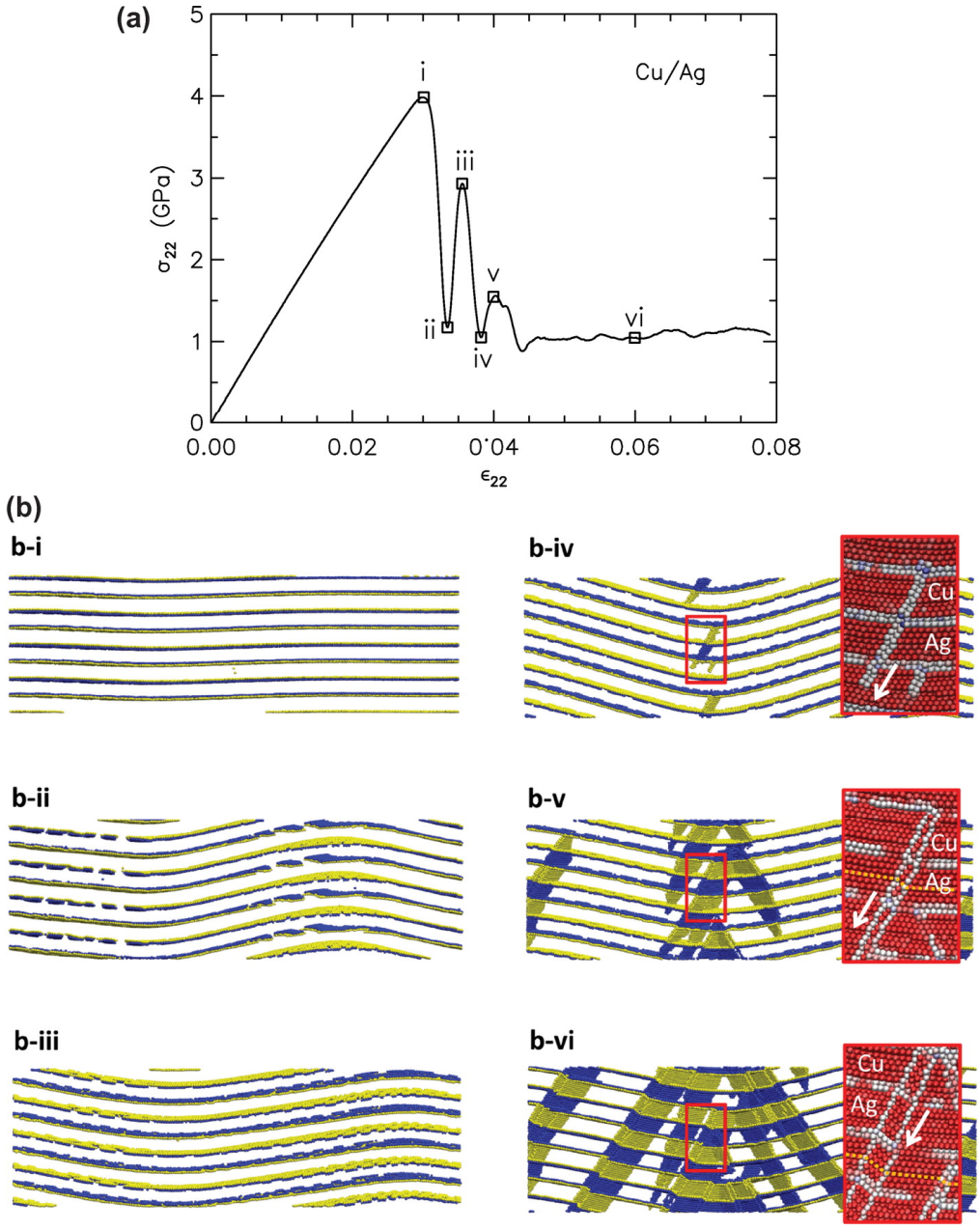

Figure 3.2 (a) Stress-strain curve of Cu-Ag nanolayers with $h = 2nm$ subjected to out-of-plane tension; (b) Atomic configurations of Cu-Ag nanolayers at instances marked in (a) as viewed from $[11\bar{2}]$ direction, demonstrating that the highly oscillatory stress–strain response corresponds to the planar-to-wavy transition of the nanolayers. Only non-FCC Ag (blue) and Cu (yellow) atoms are displayed. Close-up views show the emission of $\frac{1}{6}[\bar{2}1\bar{1}]$or $\frac{1}{6}[1\bar{2}\bar{1}]$Shockley partials with mixed edge and screw components along adjacent $(\bar{1}\bar{1}1)$slip planes from the interface (b-iv), resulting in the development of two-atom-thick micro-twins (b-v), which subsequently grow in thickness (b-vi).

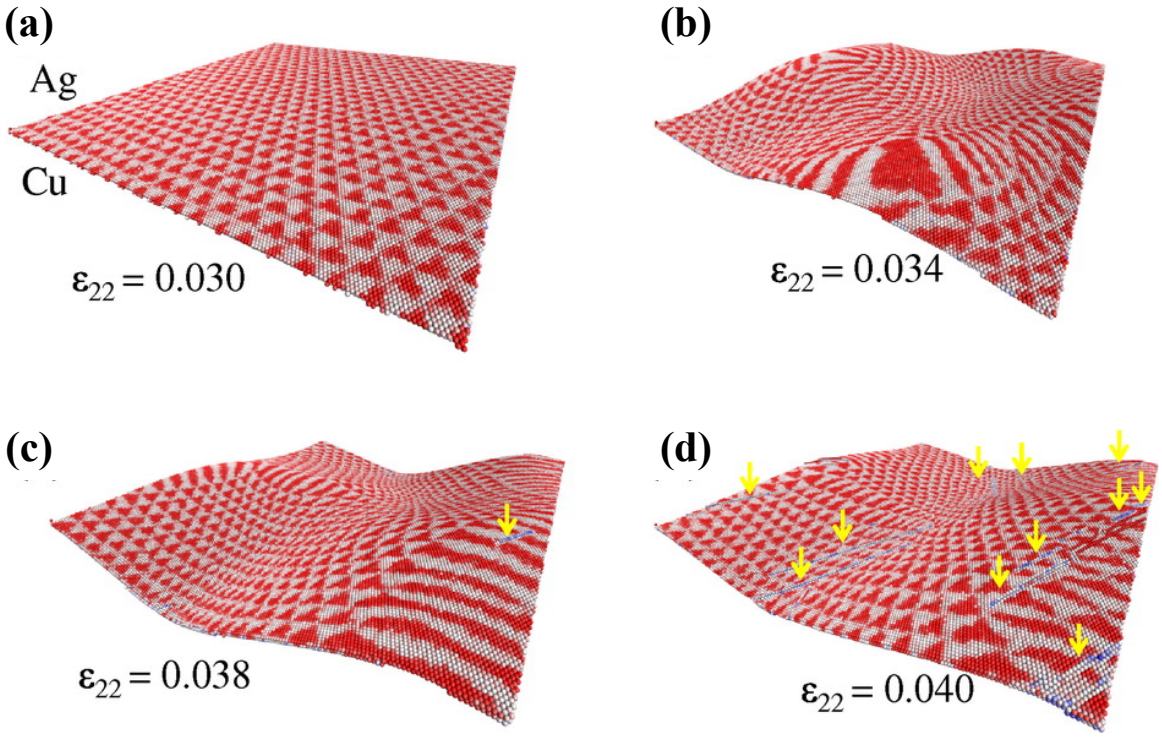

Figure 3.3 Evolving atomic configurations of a Cu–Ag interface with deformation as viewed from the Ag side. The atoms are colored by the CSP. The dissociated Shockley partials (from the misfit dislocations) are continuously redistributed along the interface from the wavy summits to the wavy valleys. Yellow arrows denote kinks in the Cu–Ag interface caused by emission or transmission of micro-twinning partials.

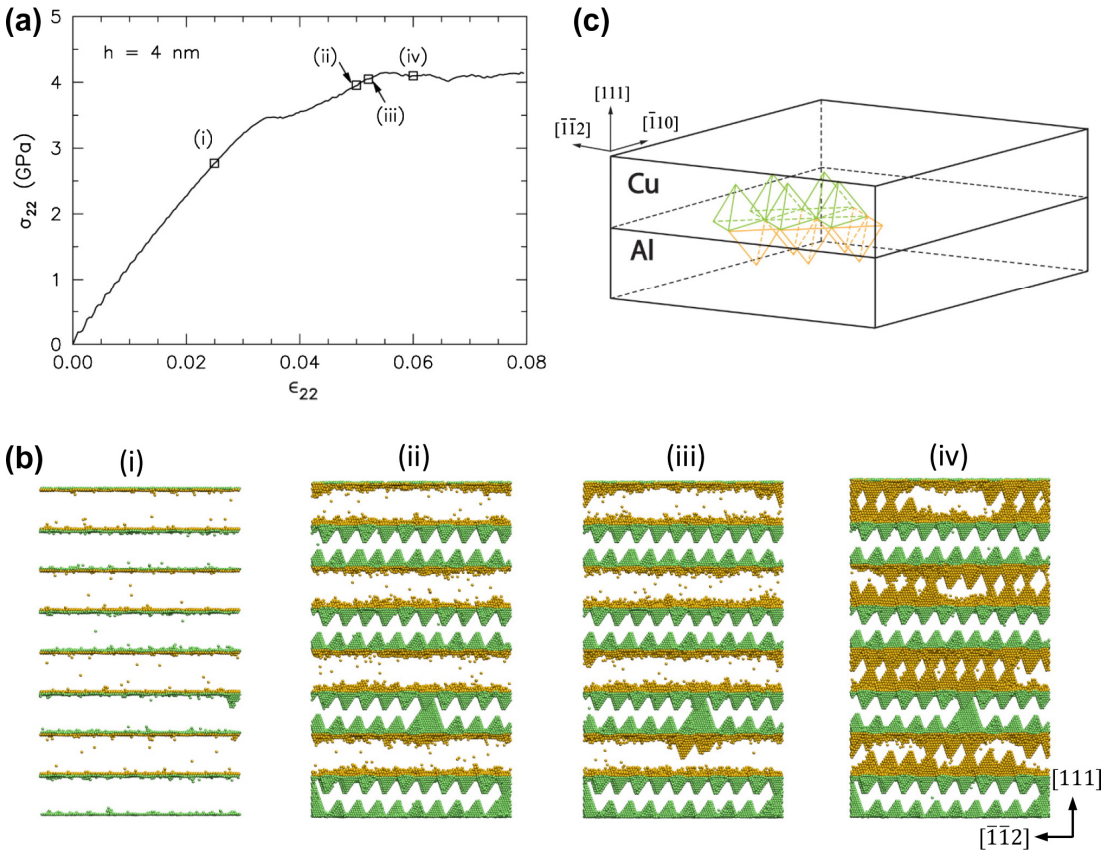

Figure 3.4 (a) Stress–strain response of the Cu–Al nanolayers with $h = 4nm$ subjected to out-of-plane tension. (b) Deformed atomic configurations of the Cu–Al nanolayers as viewed from the $[1\bar{1}0]$ direction which are filtered to display the non-FCC Cu and Al atoms colored in green and yellow, respectively. (c) Schematic of the dislocation structure along a Cu–Al interlayer interface, comprising of closed SFTs in Cu (green) and open-ended SFTs in Al (yellow).

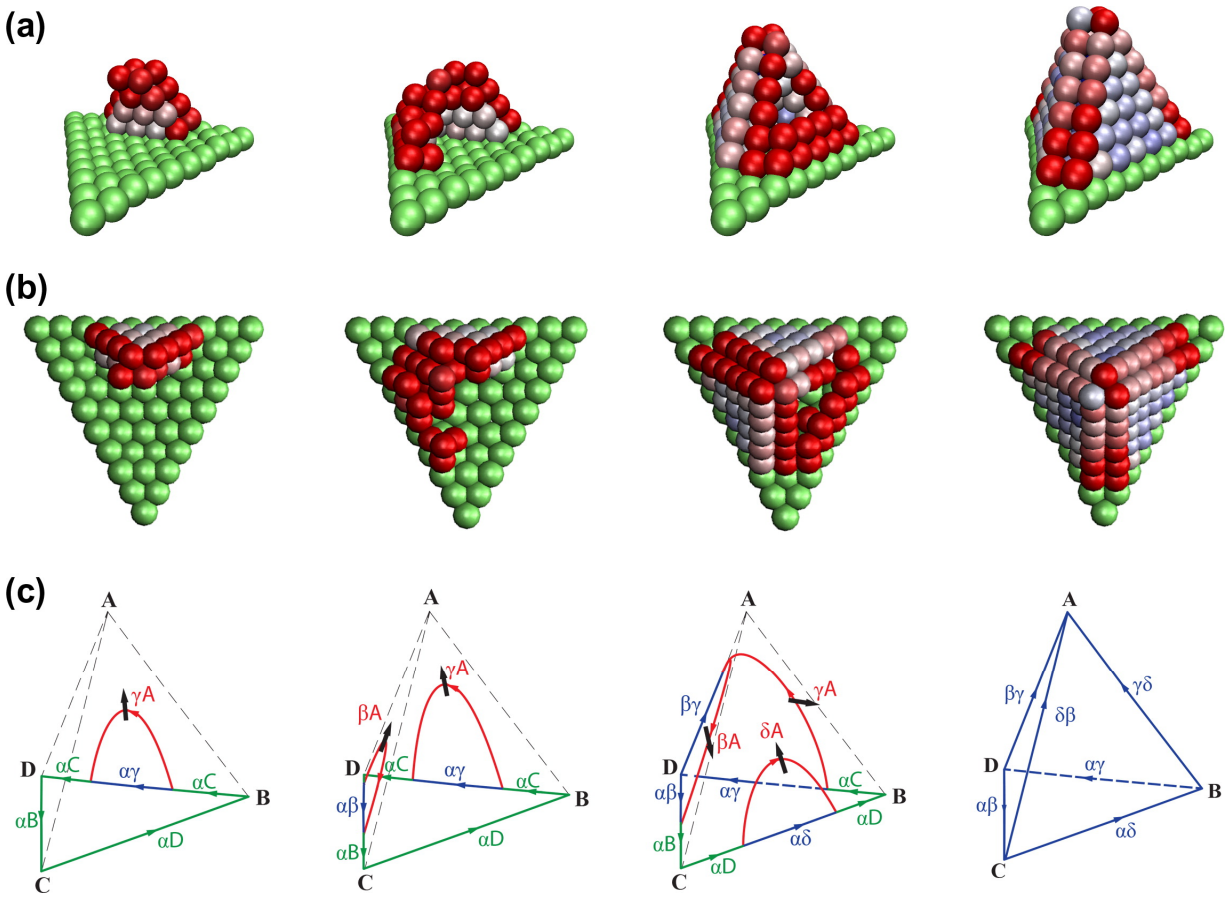

Figure 3.5 (a) Perspective and (b) top views of the formation process of a closed SFT within the Cu interlayer, located above the triangular stacking fault (colored in green on the side of Cu) along the Cu–Al interface. The atoms comprising the SFT are colored by their CSP values. (c) Schematic illustration of the dislocation mechanisms underlying the closed SFT formation process. Partial misfit dislocations along the interface are colored in green, Shockley partials on the inclined slip planes are colored in red and stair-rod dislocations are colored in blue. The colored arrows denote the positive line sense, while bold black arrows indicate the general growth direction of the Shockley partials.

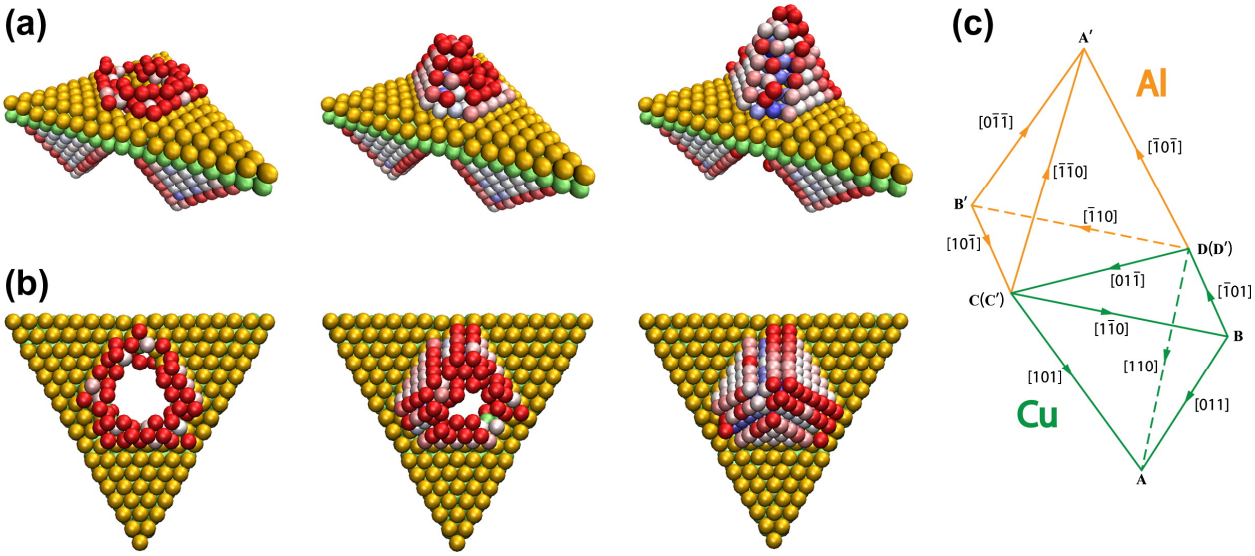

Figure 3.6 (a) Perspective and (b) top views of the formation process of an open-ended SFT within the Al interlayer, located above the perfect FCC plane of atoms along the interface. Cu and Al atoms representing the stacking fault along the interface are colored in green and yellow, respectively. The atoms comprising the SFT are colored by their CSP values. (c) Schematic illustration of the stair-rod dislocations bounding the stacking fault planes in the open-ended SFT (yellow) and closed SFT (green).

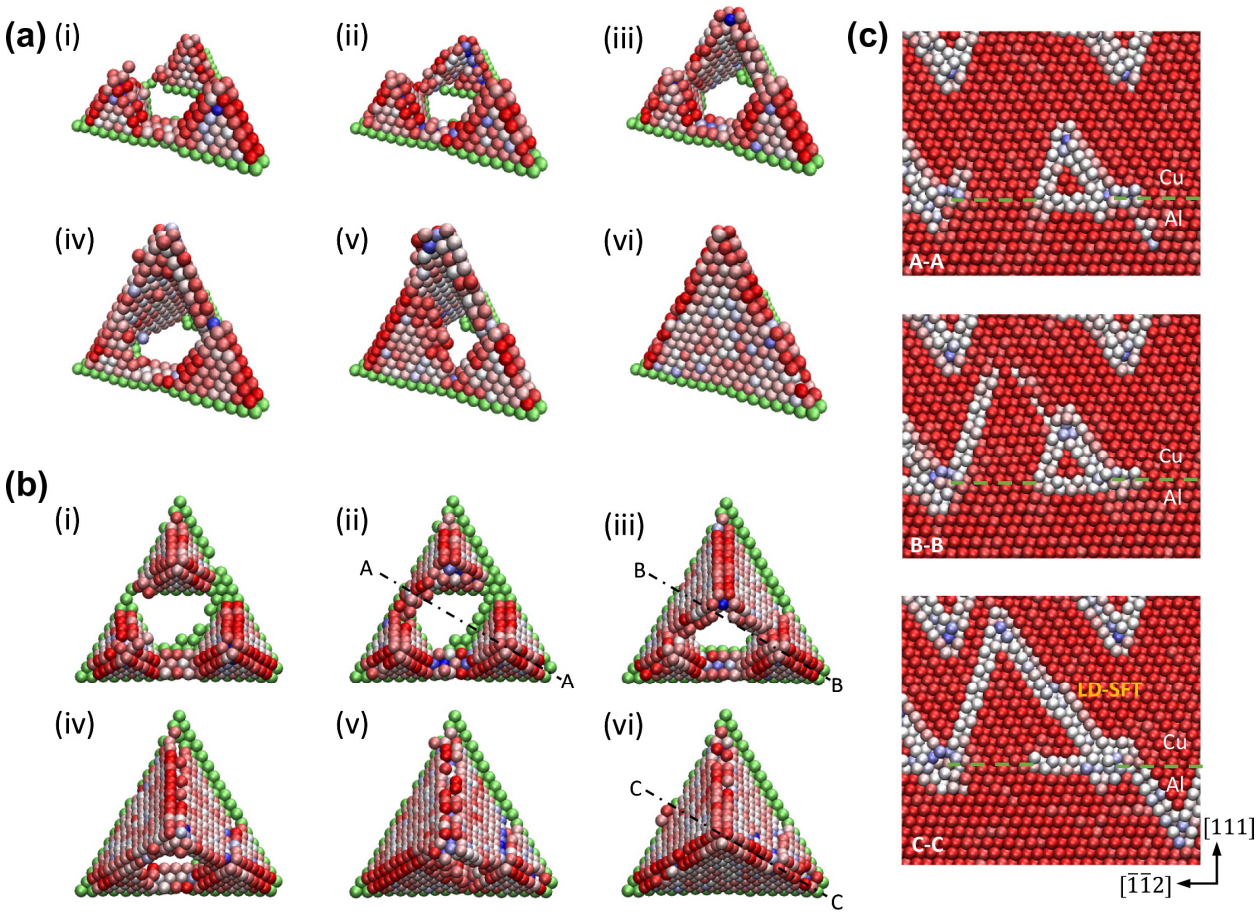

Figure 3.7 (a) Perspective and (b) top views of the formation process of a large-dimension (LD) SFT from three closed SFTs in the Cu interlayer. Cu atoms comprising the stacking faults along the interface are colored in green, while atoms comprising the SFTs are colored by their CSP values. (c) Cross-sectional views of the LD-SFT formation process along cuts A–A, B–B and C–C, in the second, third and sixth snapshots indicated in (b).

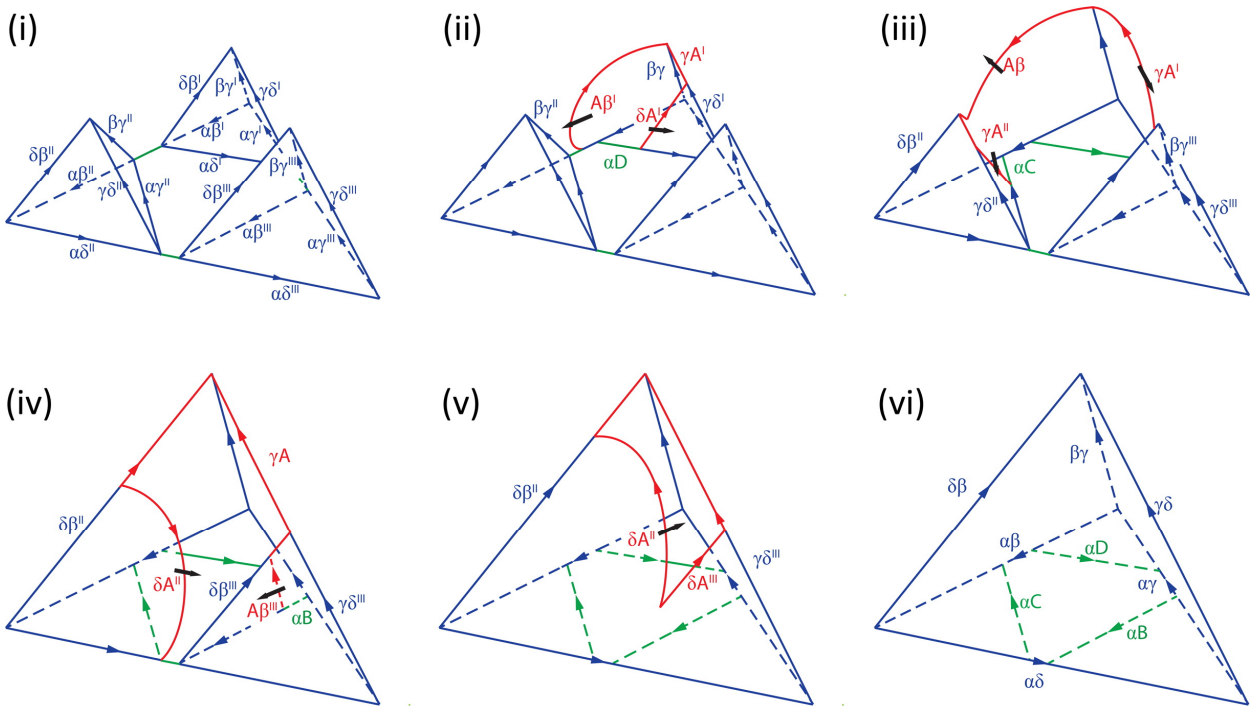

Figure 3.8 Schematic illustration of the dislocation mechanisms underlying the formation of a LD-SFT, corresponding to the six snapshots in Figure 7(a) and (b). The burgers vectors associated with the smaller SFTs are denoted with superscripts I, II and III. Partial misfit dislocations along the interface are colored in green, Shockley partials on the inclined slip planes are colored in red and stair-rod dislocations are colored in blue. The colored arrows denote the positive line sense, while bold black arrows indicate the general growth direction of the Shockley partials.

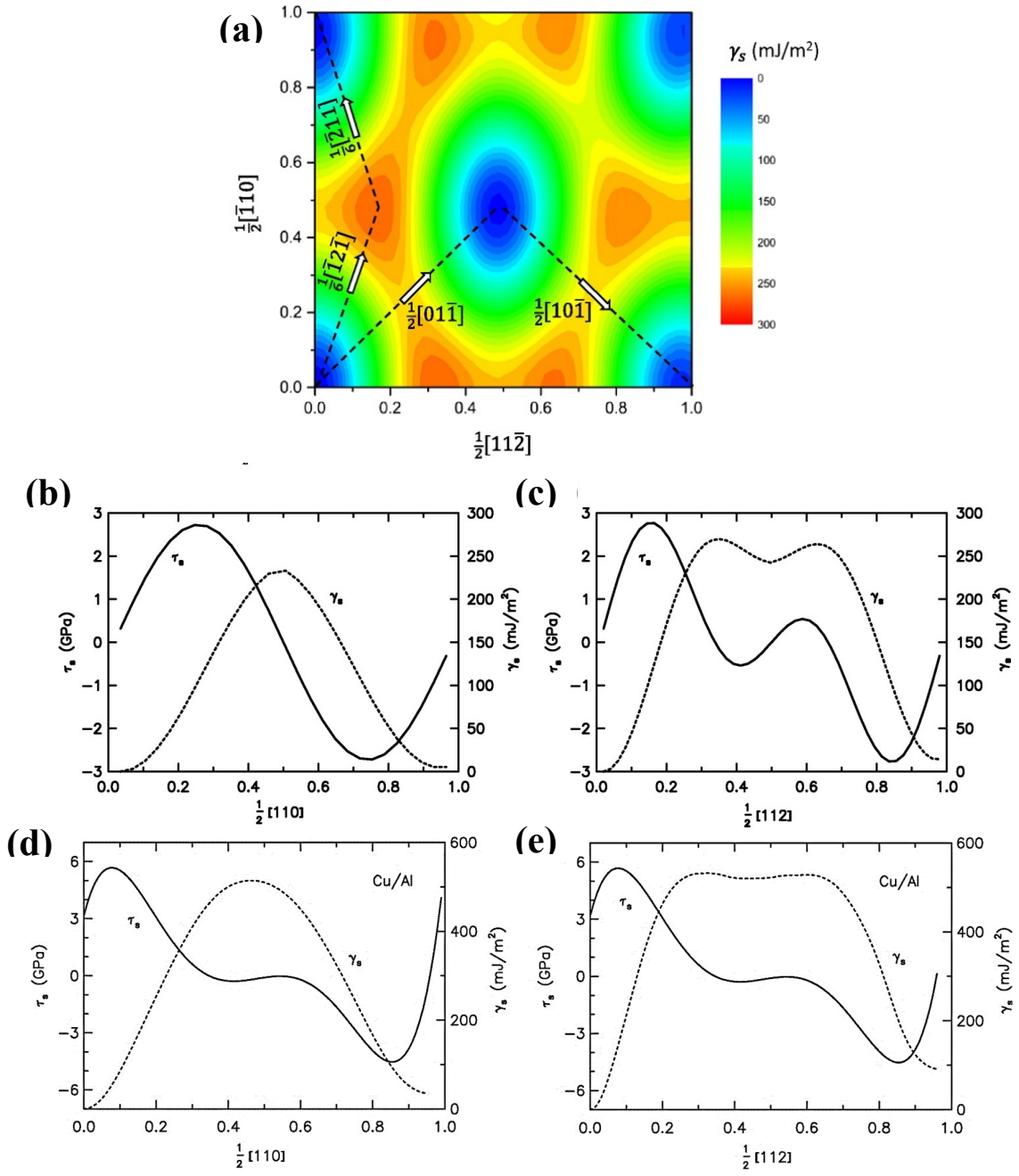

Figure 3.9 (a) GSFE surface of the Cu–Ag nanolayer interface. (b, c) GSFE $\gamma_s$and barrier strength τ_s for Cu-Ag interface sliding along the (c) ⟨110⟩ and (d) ⟨112⟩pathways. (d, e) GSFE $\gamma_s$and barrier strength $\tau_s$for Cu-Al interface sliding along the (d) ⟨110⟩ and (e) ⟨112⟩pathways.

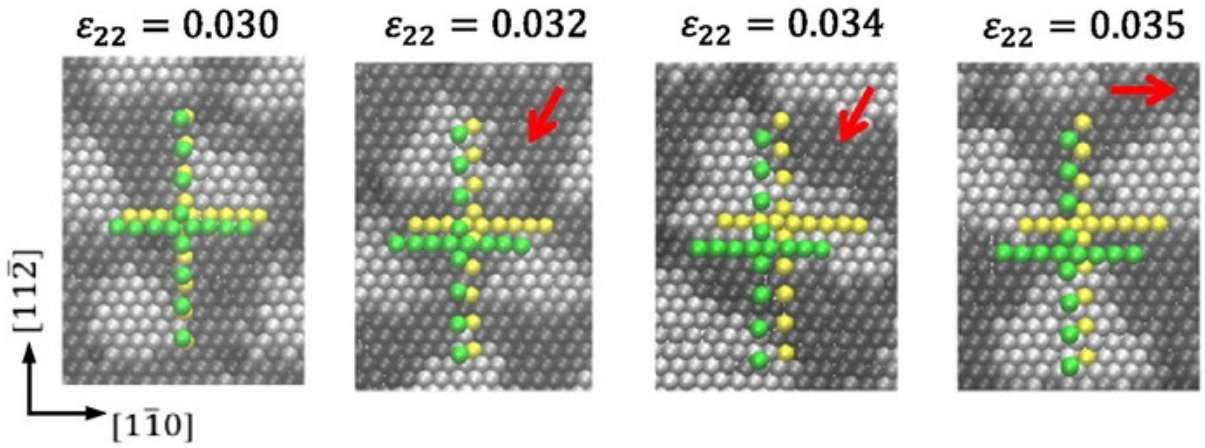

Figure 3.10 Relative motion of Cu and Ag interface atoms. Cross rows of Ag and Cu interface atoms are highlighted in green and yellow, respectively. Red arrows denote the direction of the relative motion of these Ag and Cu interface atoms, which is consistently ⟨110⟩.

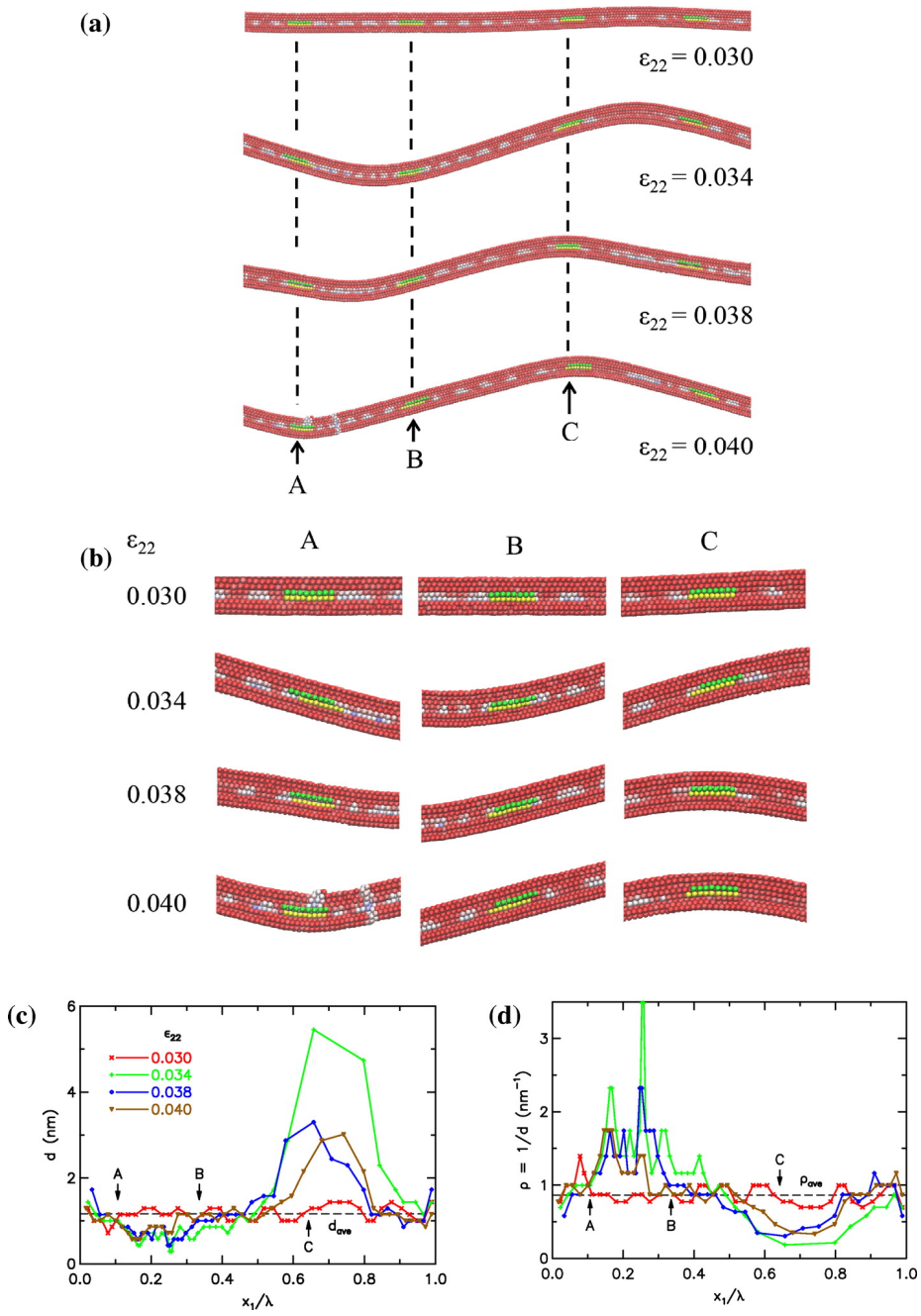

Figure 3.11 (a) Cross-sectional view of the evolving wavy profile of a Cu–Ag interface as viewed from the $[11\bar{2}]$direction, with Ag atoms on top and Cu atoms below. The atoms are colored by the CSP. (b) Close-up view of three groups of atoms (A, B and C). Selected Ag and Cu atoms in each of these three groups are colored in green and yellow, respectively, to trace their relative positions along the interface. (c) Spacing between Shockley partials d and (d) local density of Shockley partials ρ along the Cu–Ag interface for the four wavy configurations in (a).

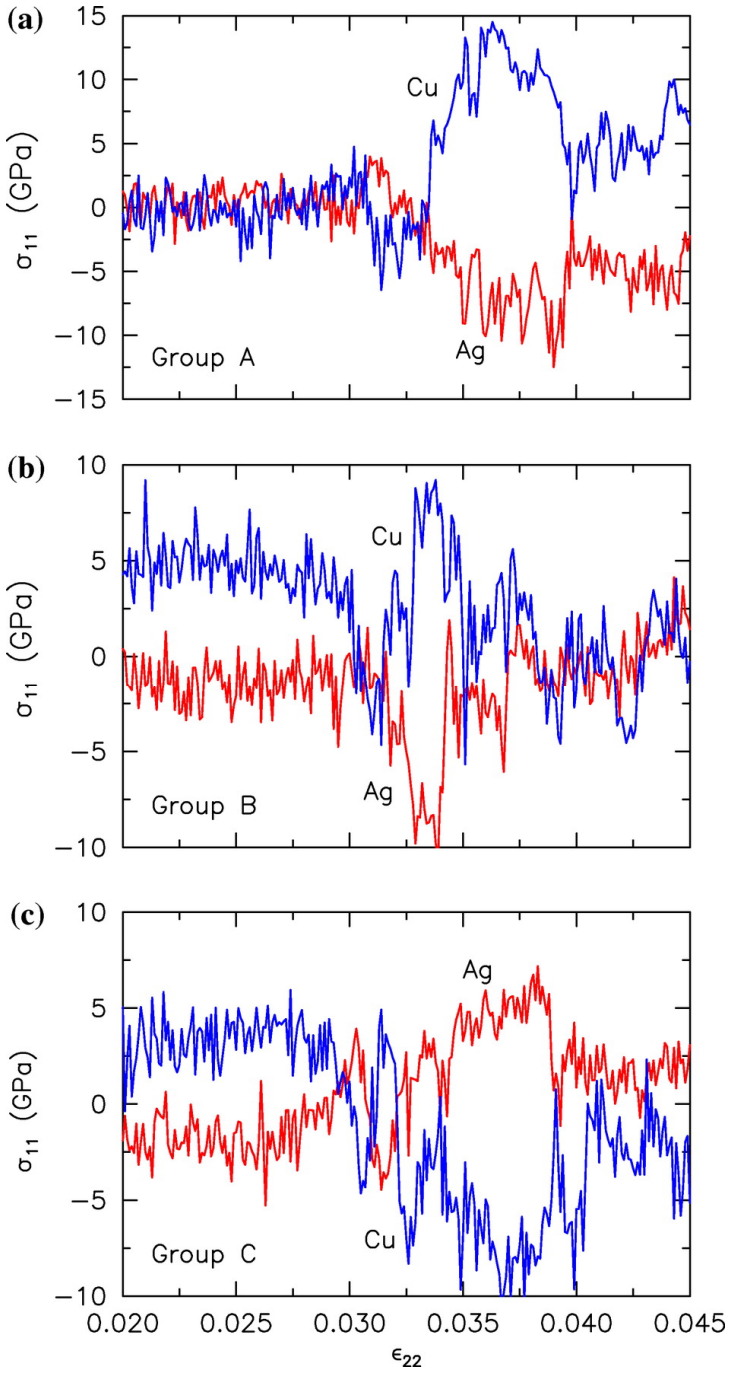

Figure 3.12 Evolution of the local stress σ_{11} versus the applied global strain ε_{22} for Cu and Ag atoms in groups (a) A, (b) B and (c) C. Tensile and compressive σ_{11} stress peaks correspond to atoms at the outer and inner bends of the wavy profile.

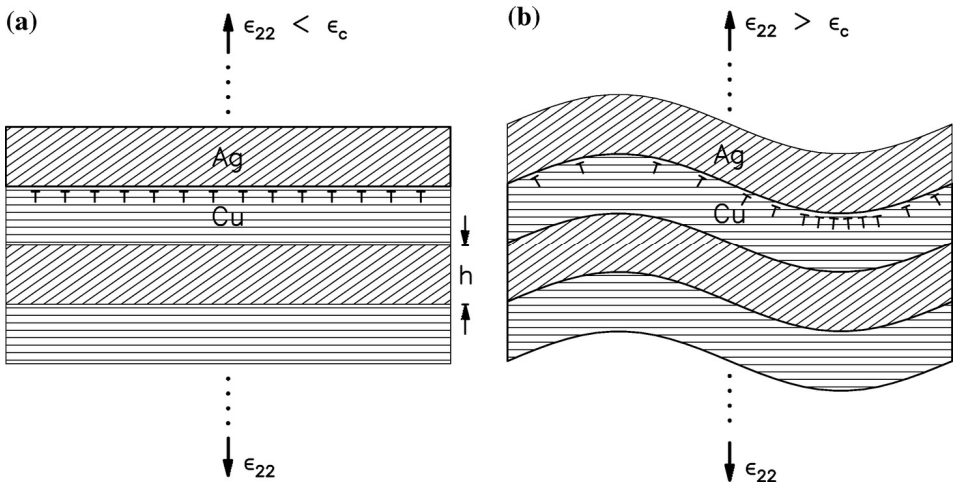

Figure 3.13 Schematic showing the redistribution of misfit dislocations along the interface during the planar-to-wavy transition of Cu–Ag nanolayers under out-of-plane tension. (a) Misfit dislocations are uniformly distributed along the planar Cu–Ag interface prior to the critical strain ε_c. (b) The formation of wavy interlayers at ε_c concurrently redistributes misfit dislocations from the wavy summits to the wavy valleys to reduce the bending stress.

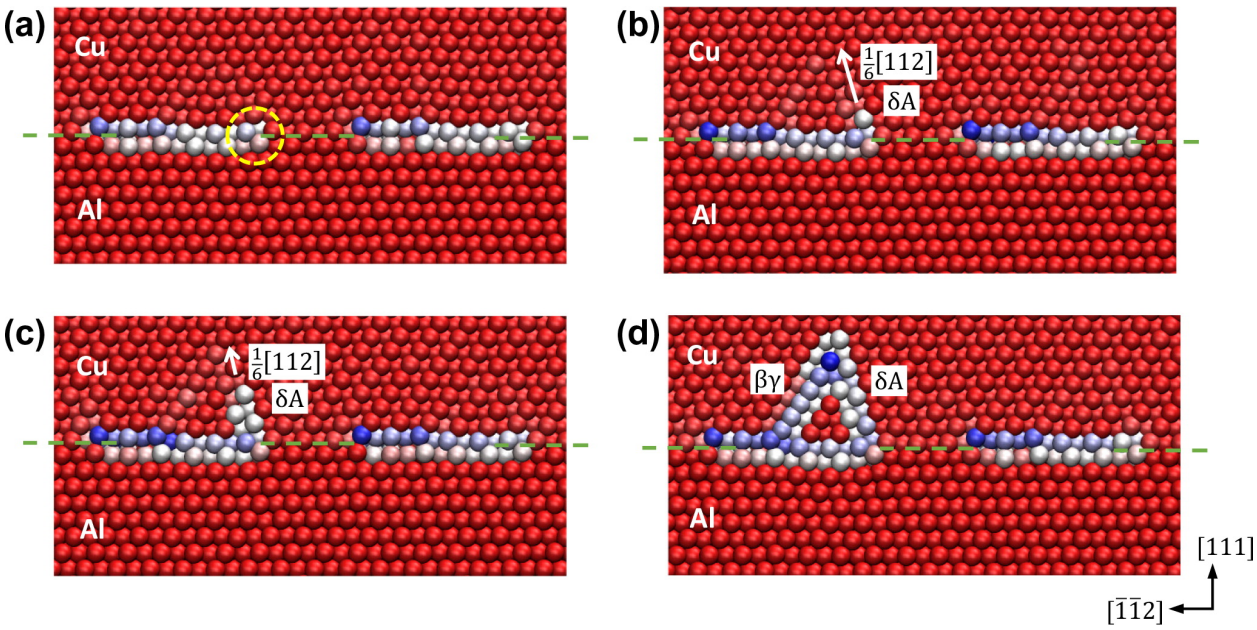

Figure 3.14 Cross section of the closed SFT formation process as viewed from the $[1\bar{1}0]$direction, with the atoms colored by their CSP values. Green dashed lines denote the Cu–Al interface. The partial misfit dislocation core is encircled by yellow dashed lines in the first snapshot, and white arrows in the second and third snapshots denote the growth directions of the emitted Shockley partials.

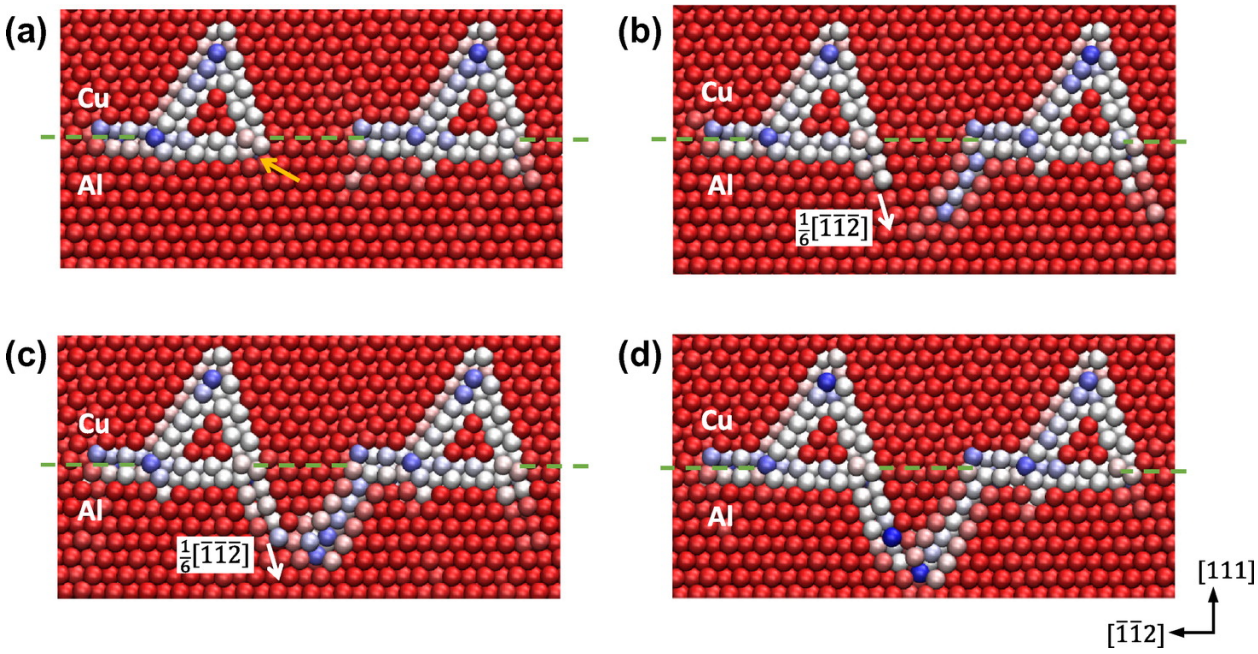

Figure 3.15 Cross section of the open-ended SFT formation process, as viewed from the $[1\bar{1}0]$direction, following the formation of closed SFTs in Cu. The atoms are colored by their CSP values. Green dashed lines denote the Cu–Al interface. Yellow arrow in the first snapshot denotes an initial gap at the core of the stair-rod dislocation along the interface, while white arrows in the second and third snapshots denote the growth directions of the emitted Shockley partials.

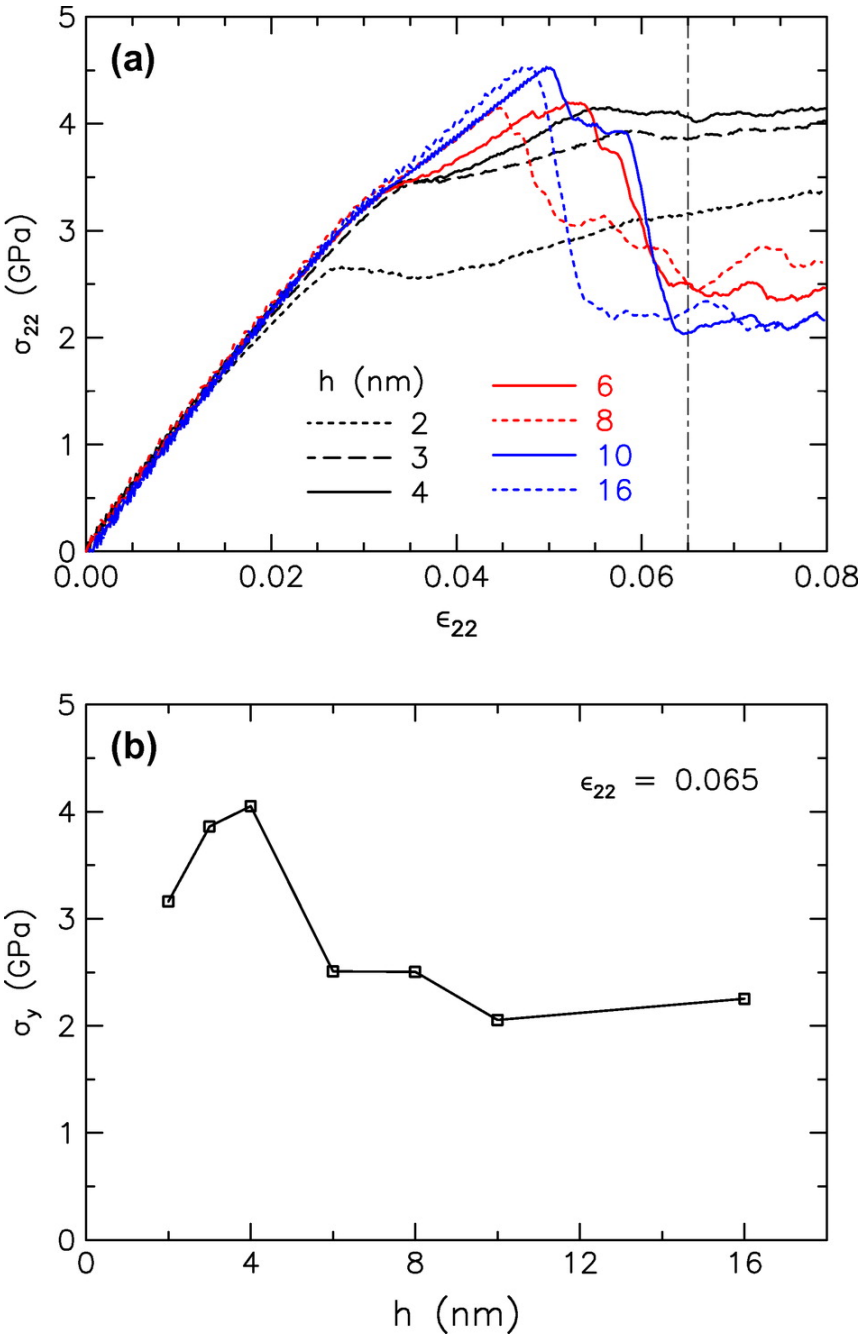

Figure 3.16 (a) Stress–strain response of Cu–Al nanolayers of varying h, subjected to out-of-plane tension under a temperature of $300K$. (b) Yield strength σ_y vs. the interlayer thickness h of the Cu–Al nanolayers taken at the strain of $\varepsilon_{22} = 0.065$.

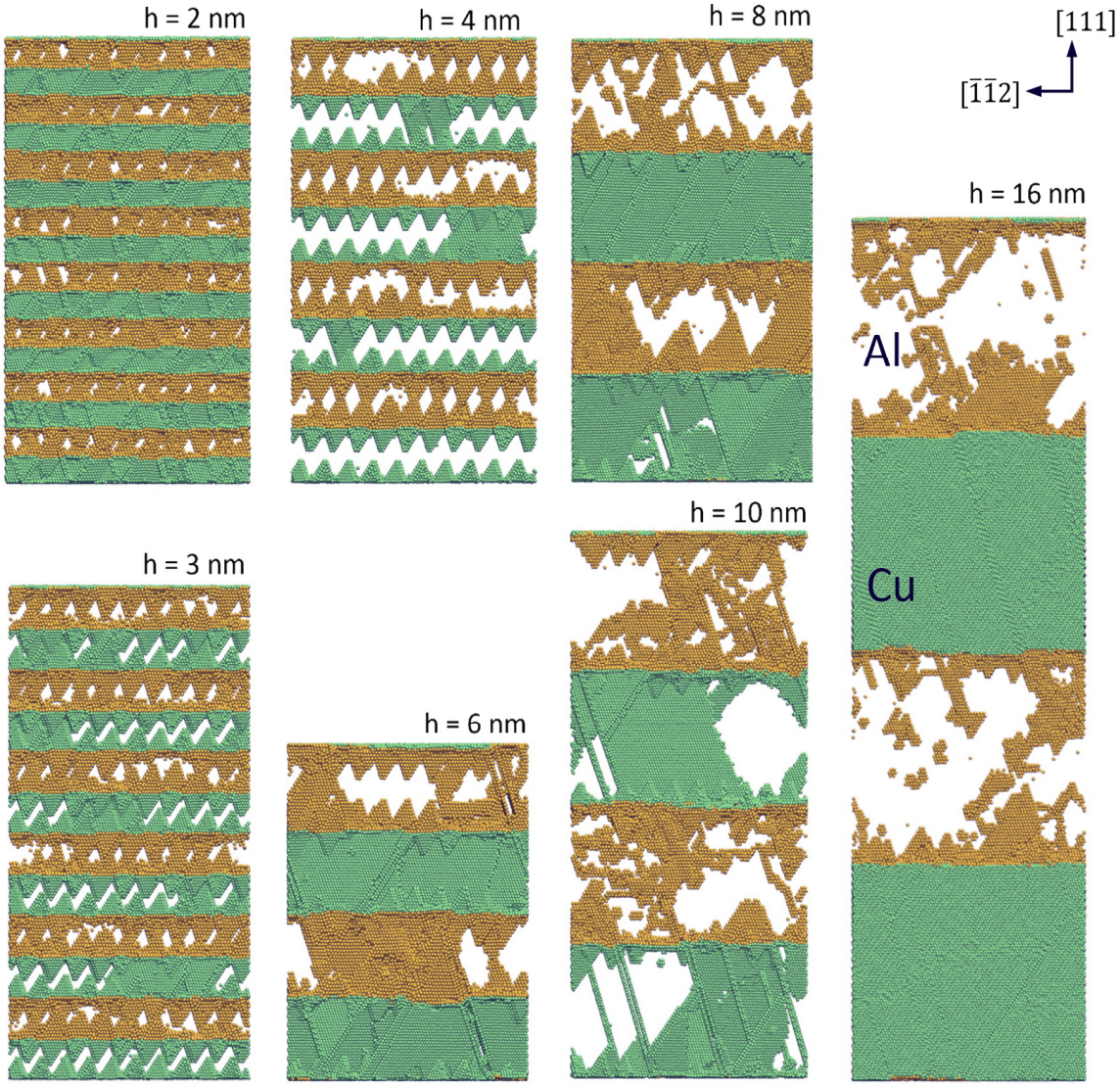

Figure 3.17 Deformed atomic configurations of the Cu–Al nanolayers at the strain of $\varepsilon_{22} = 0.065$ as viewed from the $[1\bar{1}0]$direction; the atomic configurations are filtered to display the non-FCC Cu and Al atoms, which are colored in green and yellow, respectively.

Interlayer thickness h (nm)	Lateral MD box size X (nm)	Wave number (per X) k	MD simulation results			Analytical prediction
			h/λ	ζ/λ	$dU_{elastic}$ (eV/nm^3)	h/λ
2	20	0	–	–	–	–
	25	0	–	–	–	–
	30	0	–	–	–	–
	35	0	–	–	–	–
	40	1	0.050	1.4	–0.618	0.068
	50	1	0.040	1.6	–0.658	0.065
	76	1	0.026	1.5	–0.673	0.067
	100	2	0.040	1.4	–0.545	0.066
	130	3	0.046	1.5	–0.569	0.065
4	100	1	0.040	1.5	–0.582	0.065
	230	3	0.052	1.2	–0.533	0.070
8	100	0	–	–	–	–
	200	1	0.040	1.2	–0.565	0.068

Table 3.1 Comparison of the critical h/λ predicted by MD simulations versus analytical formulation.

Chapter 4. Traction Signature: Quantitative Interface Descriptors[1]

As shown in Chapter 3, the deformation mechanics of the nanolayered metals is closely coupled to the atomic properties of the interface. While postdictive molecular dynamics (MD) simulations can be used to characterize the mechanics of the interfaces, a far better approach towards achieving interface-by-design is to develop quantitative interface descriptors capable of predicting the deformation mechanics directly from the initial equilibrium interface atomic structure. The second part of my research builds on the notion of continuum-equivalent traction fields as local quantitative interface descriptors. These descriptors are applied to symmetrical-tilt $\langle 110 \rangle$ nickel grain boundaries to predict the critical stress for dislocation emission. Predictions from the traction-based descriptors are in very good agreement with postdictive MD simulation results, and the traction signatures are used to explain the currently unresolved asymmetry in the nucleation stress for dislocation emission from the grain boundaries under uniaxial tension and compression loads.

4.1 MD Modeling and Simulation

To study dislocation emission from grain boundaries, MD simulations conducted by LAMMPS are performed on 16 bicrystal symmetrical-tilt <110> Ni grain boundary structures of

---

1. Some of the results presented in this chapter have been previously published in the following publication:
Li, R., & Chew, H. B. (2016). Grain Boundary Traction Signatures: Quantitative Predictors of Dislocation Emission. *Physical review letters,* 117(8), 085502.
Li, R., & Chew, H. B. (2017). Grain Boundary Traction Signatures: Quantifying the Asymmetrical Dislocation Emission Processes under Tension and Compression. *Journal of the Mechanics and Physics of Solids, (submitted).* Reprinted with permission from the publisher.

varying tilt angles θ; the interatomic interaction is governed by the embedded atom method (EAM) potential for Ni [83]. Each bicrystal grain boundary model structure is created by first rotating two single crystals by $\pm\frac{\theta}{2}$ respectively about the [110] x_3 axis, with the grain boundary located along the x_1 axis. By laterally displacing one of the crystals with respect to the other in 1% increments of the unit structural length along the x_1 direction and deleting the overlapping atoms with fixed overlapping distance$0.088\,nm$, multiple possible grain boundary configurations are created for each θ. Then all the possible structures are subjected to energy minimization and the lowest energy configuration is identified as the correct grain boundary structure [27, 84]. The grain boundary energies of the selected model structures are found to be in very good agreement with previous studies [21, 85]; the atomic configurations of these grain boundary structures are validated against previous simulations and existing experiments [23, 86-88]. Each of the bicrystal grain boundary structures has model dimensions of $\sim 10\times20\times10$ nm^3 in the (x_1, x_2, x_3) directions, and is fully periodic in all three directions to mimic bulk structures. The grain boundary structures are subjected to an NVT ensemble with temperature maintained at 500K by a Nose-Hoover thermostat for 0.05 ns and quenched to the target temperature of 10K within 0.03 ns using an NPT ensemble. The box is kept to be pressure-free in all three directions with a Berendson barostat during the quenching process. The 16 created grain boundaries are two-dimensional (2D) which, as reviewed in Chapter 2, are characterized by repeating sequences of A, C, D, and/or E SUs along the $x_1$axis.

Uniaxial tension (compression) simulations are performed on the grain boundary model structures by stretching (shrinking) the simulation box along the x_2 direction perpendicular to the grain boundary at a strain rate of 10^8 /s, while maintaining stress-free boundary conditions in the x_1 and x_3 directions. The system is equilibrated to the target temperature of 10 K throughout the deformation process. Previous study has shown that the atomic structures of these grain boundaries

are the same under 0K as well as elevated to 800 K; only that at elevated temperature, a multiplicity of structures may exist for one grain boundaries [23]. Thus, my simulations are conducted at 10K to obtain clear atomic configurations without thermal noise. All the simulations are based on a fixed MD time step of 1fs and conducted till the first dislocation nucleates from the simulation box.

The deformation of grain boundary structures with $55^{\circ} < \theta < 100^{\circ}$ involve phase boundary migration and grain rotation, which have been well studied in Ref. [89]. Grain boundaries with $\theta = 53^{\circ}$ and 105° are extremely stable with very low grain boundary energy; deformation of these stable grain boundaries results in emission of dislocations from within the bulk crystal (Fig. 4.1). As such, the study here will be limited to grain boundaries with $0^{\circ} < \theta < 50^{\circ}$and $120^{\circ} < \theta < 180^{\circ}$. Fig. 4.2 summarizes the 10 grain boundaries considered in my research. Fig. 4.3 shows the absolute tensile and compressive stress-strain response of these grain boundaries. Observe that the stress-strain curves exhibit sudden loss of stress-carrying capacity which corresponds to the first nucleation of dislocations in the model structure, and the maximum tensile (compressive) strength,$|\sigma_{22}|$, is termed as the critical tensile or compressive stress for dislocation emission. Tension-compression asymmetry in the critical strength for nucleation of dislocations is consistently observed across all ten <110> symmetric-tilt grain boundary structures considered here. Grain boundaries with $\theta < 50°$ is brittle which exhibit higher critical strength of $\sim 12 - 14GPa$ under tension than the $\sim 5GPa$ critical strength under compression. In contrast, grain boundaries with $\theta > 120°$ display critical strengths of $15 - 25GPa$ under compression, but is ductile under compression that readily emit dislocations with critical strength of $\sim 3 - 5GPa$.

Fig. 4.4 shows the deformed atomic configurations at the first instant of dislocation emissions for four representative grain boundaries under tension and compression loadings. Each

of these structures is filtered, based on the CSP values to display only non-FCC atoms, with dislocations colored in red and stacking faults colored in green. Observe that uniaxial compression of the $\Sigma19(116)$ and $\Sigma27(115)$ grain boundaries results in the ready emission of edge-type $\frac{1}{6}\langle 112\rangle$ Shockley partials ($\boldsymbol{b}_1$) from the boundaries, but, under tension, dislocations only nucleate in the bulk at much higher stress magnitude. Similar observations are made for the remaining $\theta < 50°$ grain boundary structures ($\Sigma33(118), \Sigma9(114)$), which implies that the grain boundary structures of $\theta < 50°$, while seemingly ductile under compression, have even higher tensile strength than the same oriented bulk FCC crystals. In contrast, the Σ33(554) and Σ33(441) grain boundaries readily emit dislocations from their pre-existing dislocations or respective E-SUs under tension. However, these grain boundaries can sustain very high compressive loads exceeding 20 GPa (Fig. 4.3b) under compression, which causes the collapse of the porous E-SUs along the boundaries to reform distorted A-SUs. Continued deformation results in the emission of non-Schmid edge-type $\{001\}\langle\bar{1}10\rangle$ full dislocations for Σ33(554) and Σ11(332) grain boundaries, while extrinsic {111} stacking faults of a few atomic layers thick are formed for the remaining $\theta > 120°$ grain boundaries (Σ9(221), Σ27(552), Σ19(331), Σ33(441)).

4.2 Reconstruction of Continuum-Equivalent Interface Traction Fields

As mentioned in Chapter 2, the presence of active dislocation sources in the form of E-SUs was previously used to explain the ready emission of dislocation along the ductile grain boundaries [27, 90]. However, why these same structures are inherently brittle under compression has not been well-understood. In addition, certain grain boundary structures also contain pre-existing dislocations in the form of edge-type Shockley partials ($\boldsymbol{b}_1$), but are inherently brittle under tension

(e.g. $\Sigma 33(118)$, $\Sigma 19(116)$). In the following, the notion of continuum-equivalent traction fields as new quantitative descriptors of the grain boundary atomic structure is introduced, and used to predict the critical stress for dislocation emission from grain boundaries under applied tensile and compressive loads.

The local disruption of atoms from their bulk crystallographic arrangement near the grain boundary generates a stress-field which decays with distance away from the boundary. Consider a plane-of-cut, with outer normal vector n_i, along the equilibrium grain boundary structure, a distribution of tractions t_i has to be introduced along this plane-of-cut to maintain the same disruption of atoms caused by the presence of the grain boundary. These tractions are taken to represent the equilibrium grain boundary structure. Since these tractions are the equivalent forces per unit area acting across the grain boundary, they are related to the Cauchy stress tensor by $t_i = \sigma_{ij} n_j$. In MD simulations, the virial definition of stress is often interpreted as the Cauchy equivalent stress [91]. However, one cannot directly determine the grain boundary tractions from virial stress information along the grain boundary, since this information is only available at discrete atomic sites and provides an indication of stress only in an averaged sense. Instead, my research adopts the field projection method (FPM) based on the principle of virtual work to project the local virial stress information as continuum-equivalent shear t_1 and normal t_2 traction distributions along the selected plane-of-cut [92-94].

For a static system without body force, the principle of virtual work can be written as [95]:

$$\int_V \delta\boldsymbol{\varepsilon} : \boldsymbol{\sigma} \, \mathrm{d}v = \int_S \delta\boldsymbol{u} \cdot \boldsymbol{t} \, \mathrm{d}s = \Delta\Phi \tag{4.1}$$

, where $\delta\boldsymbol{\varepsilon}$ is the virtual strain which is work-conjugate to the Cauchy stress $\boldsymbol{\sigma}$, $\delta\boldsymbol{u}$ denotes the admissible virtual displacement field, and $\boldsymbol{t}$ represents the boundary tractions. Fig. 4.5a shows a

schematic of the field projection scheme for projecting the atomic stress information within the domain bounded by red lines in the upper-grain to the grain boundary denoted by dashed red lines. The model is divided into five regions, D_0, D_1, D_2, D_3, and D_4, where D_1, D_2, and D_3 make up the volume V with bounding surface S in (4.1), and L and H are the width and height of the domain. The (t_1, t_2) shear and normal tractions along the grain boundary is expressed in terms of a Fourier series:

$$t_i(x_1) = \sum_{k=1}^{n} A_k^i \sin\frac{2k\pi x_1}{L} + \sum_{k=1}^{n} B_k^i \cos\frac{2k\pi x_1}{L} \tag{4.2}$$

, where k is the wave number, n is the number of Fourier terms, and A_k^i, B_k^i are the Fourier coefficients to be determined. Then the virtual displacement field in V is defined as:

$$\delta u_i^1(x_1, x_2) = \epsilon F(x_1, x_2)\sin\frac{2k\pi x_1}{L}$$

$$\text{or } \delta u_i^2(x_1, x_2) = \epsilon F(x_1, x_2)\cos\frac{2k\pi x_1}{L} \tag{4.3}$$

, where $\epsilon = 0.01$ is the amplitude of the displacement variation, and $F(x_1, x_2)$ is a perturbation envelope function:

$$F(x_1, x_2) = \begin{cases} 0 & (x_1, x_2) \in D_0 \\ \left(\frac{H}{x_2} - 1\right)\left(1 + \frac{2x_1}{L}\right) & (x_1, x_2) \in D_1 \\ 1 - \frac{x_2}{H} & \text{for} \quad (x_1, x_2) \in D_2 \\ \left(\frac{H}{x_2} - 1\right)\left(1 - \frac{2x_1}{L}\right) & (x_1, x_2) \in D_3 \\ 1 & (x_1, x_2) \in D_4 \end{cases} \tag{4.4}$$

as shown in Fig. 4.5b, which is specifically designed to achieve $\delta\boldsymbol{u} \cdot \boldsymbol{t} = 0$ along the solid red lines and $\delta\boldsymbol{u} \cdot \boldsymbol{t} \neq 0$ along red dashed line of S in Fig. 4.5a. From the definition of (4.3) and (4.4), $\delta\boldsymbol{u}$ is a continuous and smooth function, from which one can obtain the virtual strain field $\delta\boldsymbol{\varepsilon}$. The local

virial atomic stress obtained from MD is considered to represent the average Cauchy stress $\boldsymbol{\sigma}$ within the Voronoi cell around each atom. Fig. 4.5c and 4.5d display the virial σ_{22} and σ_{12}stress in the vicinity of Σ11(332) grain boundary. While there are some controversies on the equivalence between the virial definition of stress and the Cauchy stress [96, 97], this ambiguity stems from the velocity term in the former which is negligible in my study since the MD simulations are conducted at cryogenic temperatures of $10K$.

Calculating $\Delta\Phi$ from the left side of (4.1) can obtain the Fourier coefficients $A_k^i = \frac{2\Delta\Phi_k^1}{\epsilon L}, B_k^i = \frac{2\Delta\Phi_k^2}{\epsilon L}$, and in turn $t_i(x_1)$, where $\Delta\Phi_k^{1,2}$ represent the total interatomic potential energy variation caused by $\delta u_i^{1,2}$ in (4.3). Because each grain boundary structure has a period length d_p, significant changes to the traction distributions occur only at Fourier term n intervals of L/d_p. Fig. 4.5e and Fig. 4.5f show the t_1, t_2 shear and normal tractions along a Σ11(332) grain boundary structure, with increasing number of normalized Fourier terms $\hat{n} = nd_p/L$. Observe that convergence is approximately achieved at $\hat{n} = 4$ to 5 for both t_1 and t_2 traction distributions. Furthermore, the converged field-projected traction distributions are in good agreement with the discrete atomic (virial) stress values centered at atoms which are within 1.5 Å from the boundary (cross symbols in Fig. 4.5e and 4.5f). For all the grain boundary structures, same convergence analysis is repeated to obtain the final converged traction distributions. The reconstructed grain boundary tractions satisfy both compatibility and equilibrium requirements, and are therefore continuum-equivalent descriptors for the grain boundary atomic structures.

Grain boundary structures are typically of finite thickness, and the extracted traction distributions will be sensitive to the plane-of-cut taken along the finite thickness dimension (x_2). To accurately predict the critical stress for emission of dislocations from the boundary, the traction

distributions should be centered about the cores of pre-existing dislocations along the boundary or at locations where slip first initiates, for example near the relevant E-SUs. These dislocation emission sites typically have high resolved shear stress along the active slip-plane [98]. Fig. 4.6a shows the equilibrium grain boundary structure for $\Sigma 27(115)$, which colored by their CSP values. The three shear (t_1) and normal (t_2) traction distributions corresponding to three planar cuts (red, blue, and magenta lines in Fig. 4.6a) taken along the grain boundary are shown in Fig. 4.6b and 4.6c respectively. The t_1 tractions are negligible along the center of the boundary (red line) due to the symmetrical structure of the $\Sigma 27(115)$ grain boundary. The t_2 tractions, however, fluctuate between positive and negative peaks of $\sim \pm 30GPa$ within a single atomic spacing at periodic sites along the boundary. At these sites, the equal but opposite t_2 tractions on pairs of neighboring atoms contribute to shear dominant loading along the two neighboring closed-packed {111} slip planes in the $\langle 112 \rangle$slip direction, as denoted by white arrows in Fig. 4.6a. This non-trivial resolved shear stress arises solely from local tractions along an undeformed grain boundary structure, and allows one plane of atoms to slip more easily over its neighboring plane of atoms. Hence, the sharp transition in the t_2 tractions between atom pairs on neighboring slip planes are indicative of initiation sites for dislocation slip. This has been confirmed by postdictive MD simulations under uniaxial compression, as shown by the deformed atomic configuration of the $\Sigma 27(115)$ grain boundary in the inset in Fig. 4.6a. In addition, the fluctuations of t_2 traction decline with increasing distance x_2 distance from the initiation sites for dislocation slip, due to the decay of the local stress field. The t_1 tractions become more distinctive some distance away (blue line) since the structure is no longer symmetric, but rapidly decreases to 0 as the plane of cut is sufficient away from dislocation initiation sites (magenta line).

4.3 Traction-assisted Shockley Partial Emission

Fig. 4.7 and Fig. 4.8 summarize the traction signatures of grain boundary structures with $0^{\circ} < \theta < 50^{\circ}$ and $120^{\circ} < \theta < 180^{\circ}$ respectively. The traction signatures of equilibrium grain boundary structures and related atomic configurations are displayed in Fig. 4.7-i, ii and 4.8-i, ii. Because of the translational symmetry of these grain boundary structures, similar traction signatures are observed along the green dashed lines for dislocation emissions into the lower grain. From the MD simulations results, the low critical strength of $\theta < 50°$ grain boundaries under uniaxial compression and $\theta > 120°$ grain boundaries under uniaxial tension is associated with the ready emission of edge-type $\langle 112 \rangle \{111\}$ Shockley partials ($\boldsymbol{b}_1$). In all cases, the transitions in the t_2 traction peaks between neighboring atom pairs from positive to negative or vice-versa (black dashed lines in Fig. 4.7 and 4.8), assisted at times by similar transition in the t_1 traction peaks (in the case of $\Sigma 33(554)$), result in high resolved shear stresses along the $\{111\}\langle 112 \rangle$ slip system. The atomic configurations of these grain boundaries at the instant of Shockley partial emission under corresponding load are display in Fig. 4.7-iii and 4.8-iii as well, which further confirm that slip indeed initiates from the traction transition locations. The close-up views of the deformed configurations in Fig. 4.8 display the effect of traction fields to resolved shear stress along the slip planes. While the atomic scale tractions are presented in Fig. 4.8-i as well the further validate traction field.

The critical resolved shear stress τ_c for emission of a b_1 partial has contributions from both the grain boundary normal and shear tractions, τ_{GB}, and external loading, τ_{ext}. To quantify the former, 2D finite element analysis is carried out with the commercial code ABAQUS 6.13 with a parallelogram model of length d_p in the x_1 direction to represent a single period of the upper grain

of the bicrystal structure. The parallelogram is inclined at an angle α with respect to the x_1 axis, representing the angle between grain boundary interface and the possible $\{111\}$ slip planes for Shockley partial emissions (Fig. 4.9a). The inclined boundaries on the left and right edges of the model are tied to simulate periodic boundary conditions, and the continuum-equivalent t_1 and t_2 grain boundary tractions are applied along the lower boundary of the half-space model (In Fig. 4.9a, traction signatures of $\Sigma 11(332)$ grain boundary is applied). The crystal structure is modeled with 4-noded bilinear plane strain elements, while infinite elements are introduced at the upper boundary of the model to represent the far field bulk crystal. The material properties are elastic anisotropic, with elastic constants $c_{11} = 247GPa$, $c_{44} = 125GPa$ and $c_{12} = 148\ GPa$ defined in the three $\langle 100 \rangle$material orientations [83].

To model partial dislocation slip induced by the grain boundary tractions, 4-noded cohesive zone elements are implemented along the $\langle 112 \rangle$ emission pathway pre-determined from traction signatures of the respective grain boundaries. To construct the constitutive relationship of the cohesive zone model, the generalized stacking fault energy (GSFE) surface of Ni is calculated by rigidly displacing two halves of a Ni single crystal along the close packed (111) plane in both the $[1\bar{1}0]$ and $[11\bar{2}]$ directions in MD simulations. Then the shear traction versus separation relationship for partial dislocation slip (solid black curve in Fig. 4.9b) is obtained by taking the gradient of the GSFE along the $\langle 112 \rangle$direction. This MD-derived traction-separation relationship is fitted to an exponential traction-separation law (dashed curve in Fig. 4.9b), which governs the shear response of the cohesive elements along the $\langle 112 \rangle$slip plane [99]. The normal traction-separation relation in the cohesive zone is set extremely large to simulate strong bond between close packed planes, while normal and shear traction-separation laws are not coupled.

The above finite element model is used to compute the grain boundary sliding-separation (δ_{GB}) along the slip direction, and in turn the resolved shear stress τ_{GB} contribution from the grain boundary traction distributions. The resolved shear stress contribution τ_{GB} associated with the equivalent sliding-separation, δ_{GB}, is achieved from inset in Fig. 4.9c. For a partial dislocation to be emitted, the total resolved shear stress from contributions of both τ_{GB} and external loading $\tau_{\mathrm{ext}} = m\,\sigma_{22}$ must exceed the critical barrier stress of τ_0~5.1 GPa for shear-slip (Fig. 4.9b), where σ_{22} is the applied tensile or compressive stress, and m is the Schmid factor of the slip-system associated with the $\boldsymbol{b}_1$ partial emission from the grain boundary**.** Hence, the critical tensile or compressive strength of the grain boundary, associated with the ready emission of Shockley partials, can be derived as

$$\sigma_{22}^{c} = (\tau_0 - \tau_{\mathrm{GB}})/m \tag{4.5}$$

As shown schematically in Fig. 4.9d for external tensile load and Fig. 4.9e for external compressive load, however, τ_{GB} only assists sliding of the slip-planes if τ_{ext} acts in the same direction as τ_{GB}. If τ_{GB} acts in the opposite direction of τ_{ext}, then, τ_{ext} must overcome both τ_0 and τ_{GB} to allow Shockley partial emission based on (4.5); the actual τ_{ext} required could be even higher in practice, since the emission of Shockley partials (e.g. $\frac{1}{6}[\bar{1}1\bar{2}]$) in the reverse direction ($[1\bar{1}2]$) requires the concurrent slip of two ($\frac{1}{6}[211]$ and $\frac{1}{6}[\bar{1}\bar{2}1]$) Shockley partials. This explains why grain boundary structures which readily emit dislocations under compression ($\theta < 50°$) tend to display high nucleation strength under tension, while those which readily emit dislocations under tension ($\theta > 120°$) display high nucleation strength under compression. The traction signatures further confirm that τ_{GB} for grain boundary structures with $\theta < 50°$ acts in the direction of τ_{ext} from uniaxial compression (Fig. 4.9e), while τ_{GB} for grain boundary structures with $\theta > 120°$ acts in the

direction of τ_{ext} from external tension (Fig. 4.9d). My predictions of σ_{22}^{c} based on (4.5) for the ready emission of Shockley partial dislocations, as summarized in Fig. 4.10, are in perfect agreement with postdictive MD simulation results.

4.4 Traction-impeded Dislocation Emission

When τ_{ext} generated by external loading acts in the opposite direction of τ_{GB}, the grain boundaries can now sustain much higher stresses prior to defect emission. In addition, the suppression of Shockley partial emission by the grain boundary tractions infers that other dislocation mechanisms instead can be activated. For the $\theta < 50°$ grain boundaries, the high critical strength of the grain boundaries under uniaxial tensile loading exceeds the $\sim 12GPa$ tensile strength of the perfect crystals, which allows dislocations to instead nucleate from the bulk (see Σ27(115) and Σ19(116) in Fig. 4.4). Hence, the critical tensile strength for the bi-crystal grain boundary structures are almost the same as that in perfect FCC crystals with the same tilt orientations [98]. For the $\theta > 120°$ grain boundaries, which favor the ready emission of dislocations only under tension, two new dislocation mechanisms are observed under high external compressive stresses: emission of non-Schmid full dislocations for Σ33(554) and Σ11(332) grain boundaries, and formation of extrinsic stacking faults for Σ9(221), Σ27(552), Σ19(331) and Σ33(441) grain boundaries.

4.4.1 Non-Schmid Full Dislocation Emission

During compressive deformation of the Σ33(554) grain boundary, pre-existing dislocations ($\boldsymbol{b}_1$) along the boundary (Fig. 4.8d-ii) first reform E-SUs. Under further compression, each of these

porous E-SUs in turn collapses to form two distorted A-SUs, as shown by the deformed atomic configuration prior to dislocation emissions in Fig. 4.11a. This reformation and subsequent collapse of the E-SUs along the boundary is completed under large compressive loads of ~15 GPa, since the resolved shear stress generated by external loads must overcome those from pre-existing grain boundary tractions. Beyond this point, non-Schmid $(001)[\bar{1}10]$ full dislocations, rather than Shockley partials, are emitted from the boundary, as shown in Fig. 4.11b. To understand the mechanisms underlying this process, the traction distributions along the deformed Σ33(554) grain boundary structure corresponding to Fig. 4.11a are projected in Fig. 4.11c. Here, $\hat{t}_1$ and $\hat{t}_2$ represent the uniform (mean) shear and normal tractions introduced by external compression, while the plotted $(t_1 - \hat{t}_1)$ and $(t_2 - \hat{t}_2)$ distributions represent the fluctuations in shear and normal tractions caused by the atomic structure of the deformed grain boundary. Similar traction profiles are observed compared to the traction distributions along the equilibrium Σ33(554) grain boundary structure in Fig. 4.8d-i. However, the reconfigured atomic structure of the grain boundary now exhibits two-fold higher compression-tension peaks for $(t_2 - \hat{t}_2)$. In addition, the compression-tension peaks are now shifted to atom pairs along neighboring (001) planes; the high τ_{GB} along the (001) $[\bar{1}10]$ slip system, as denoted by arrows in Fig. 4.11b, then results in the emission of full dislocations. This is in contrast to the deformation process of Σ33(554) under tension, where fluctuations in the traction signatures are centered about atom pairs along neighboring (111) planes.

The critical external load, σ_{22}^{c}, to trigger the emission of (001) $[\bar{1}10]$ full dislocations from the Σ33(554) grain boundary under compression can be ascertained from (4.5). The τ_{GB} of the deformed grain boundary atomic configuration in Fig. 4.11a is computed from the finite element half-space model with imposed $(t_1 - \hat{t}_1)$ and $(t_2 - \hat{t}_2)$ traction distributions along the lower

boundary. The cohesive elements in the new finite element model are now along the $[\bar{1}10]$ direction, and the associated traction-separation law is calculated from the gradient of the {001} plane GSFE for {001}<110> slip. Because of the high external compressive stress of $\sigma_{22}^{\mathrm{ext}} = -18.7$ GPa just prior to initiation of slip, the {001} plane of the crystal structure experiences high normal stress of $\sigma_n = \sigma_{22}^{ext}\cos^2\alpha$, where α denotes the angle between the grain boundary interface and the relevant {001} slip plane. This high compressive normal stress will significantly increase the GSFE along {100} plane [29]. As such, the {001} plane GSFE is obtained by rigidly displacing the (001)-oriented grains along the <110> direction in MD, while simultaneously imposing σ_n on the (001) surface. The extracted cohesive zone laws are shown in Fig. 4.11d (solid curve). Note that neglecting the normal load contribution (dashed curve) underestimates the critical barrier stress τ_0 for shear slip (16 GPa versus 18.5 GPa). My predicted critical strength of the boundary of $\sigma_{22}^{c} = -20.2$ GPa obtained from (4.5) is in close agreement with the MD-obtained value of -18.7 GPa. Similar calculations for the Σ11(332) grain boundary are performed and have obtained critical compressive strength values of $\sigma_{22}^{c} = -20.5$ GPa, which again is in good agreement with MD-obtained value of -20.2 GPa.

4.4.2 Extrinsic Stacking Fault Formation

The formation of extrinsic stacking faults is observed for grain boundaries with tilt angles of $\theta > 140°$ (Σ9(221), Σ27(552), Σ19(331), and Σ33(441)) subjected to uniaxial compression. Similar to the Σ33(554) and Σ11(332) grain boundaries discussed above, the compressive deformation process first results in the collapse of the porous E-SUs into two distorted A-SUs, as shown for the Σ33(441) grain boundary (Fig. 4.12a-i). Subsequent deformation induces the emission of a mixed partial ($\boldsymbol{b}_3 = \frac{1}{6}[211]$) along a $(\bar{1}11)$ close-packed plane (Fig. 4.12a-ii),

which is quickly followed by the emission of a second mixed partial ($\boldsymbol{b}_2 = \frac{1}{6}[\bar{1}\bar{2}1]$) along another parallel $(\bar{1}11)$ close-packed plane two {111} atomic planes away (Fig. 4.12a-iii). The emission of this second $\boldsymbol{b}_2$ partial cancels out any out-of-plane [110]deformation, i.e.

$$\frac{1}{6}[211] + \frac{1}{6}[\bar{1}\bar{2}1] = \frac{1}{6}[1\bar{1}2] \ \ (\text{-}\boldsymbol{b}_1) \tag{4.6}$$

, which displaces the crystal structure only along the $[\bar{1}1\bar{2}]$ direction, leaving behind a single atomic-layer thick extrinsic {111} stacking fault. A top view of the $(\bar{1}11)$closed-packed planes during the extrinsic stacking fault formation process is shown in Fig. 4.12b (above): grey atoms denote the {111} stacking fault plane (B) with neighboring {111} planes represented by yellow (A) and green atoms (C). The grey and green planes, as well as the crystal structure below, first slips in the [211] direction with $\boldsymbol{b}_3$, which is followed by slip of the green plane and crystal structure below in the $[\bar{1}\bar{2}1]$ direction with $\boldsymbol{b}_2$. This process leaves behind the extrinsic stacking fault, represented by the grey plane. The extrinsic stacking fault formation process is schematically illustrated in Fig. 4.12b (below). I have also observed deformation process with $\boldsymbol{b}_2$emission prior to $\boldsymbol{b}_3$emission along the Σ33(441) grain boundary, which is expected since both deformation processes have the same total effect ($-\boldsymbol{b}_1$) and which mix partial emits first only depends on the local out-of-plane (x_2) stress. Similar mechanisms are also observed for the Σ9(221), Σ27(552) and Σ19(331) grain boundaries, albeit with different extrinsic stacking fault thicknesses. This deformation mechanism is different from the simultaneous emission of numerous partial dislocations from the grain boundary, which leads to the formation of hexagonal-closed-packed (HCP) phase for symmetrical-tilt $\Sigma 19$ Cu grain boundary [29], presumably because of the higher stacking fault energy of Ni.

The reconfiguration of the grain boundary structure brought about by the collapse of the E-SUs into two A-SUs leads to a reconfiguration of the local stress field near the boundary. Comparison of the traction signatures of the equilibrium Σ33(441) grain boundary (Fig. 4.8f-i) versus the deformed grain boundary just prior to emission of $\boldsymbol{b}_3$ partials (Fig. 4.12a-i) shows that the maximum fluctuations in the traction peaks, and consequently the initiation sites for slip, have now shifted. However, these fluctuations in the traction peaks are still centered about two $(\bar{1}11)$ close-packed planes. Along the favored $(\bar{1}11)[\bar{1}1\bar{2}]$ slip system, τ_{GB} generated by these grain boundary tractions is in the same direction as τ_{ext}, but both $(\tau_{\mathrm{GB}} + \tau_{\mathrm{ext}})$ act in opposite direction to the $\boldsymbol{b}_1 = \frac{1}{6}[\bar{1}1\bar{2}]$ Shockley partial emission direction. Unlike full dislocations, emission of partial dislocations can only happen in one direction (i.e. $+\boldsymbol{b}_1$) [100]. In this case, where $(\tau_{\mathrm{GB}} + \tau_{\mathrm{ext}})$ act in the reverse direction (i.e. $-\boldsymbol{b}_1$), the asymmetry of partial dislocation slip requires the emission of ($\boldsymbol{b}_2 + \boldsymbol{b}_3$) partials to create the extrinsic stacking faults seen in my MD simulations.

4.5 Discussion

4.5.1 Relationship between Grain Boundary Tractions and Grain Boundary Energy

The grain boundary t_1, t_2 tractions will have associated u_1, u_2 separations along the grain boundary as a work-conjugate. For grain boundaries with active dislocation sources, i.e. pre-existing Shockley partials, the u_1, u_2 local separation distributions are computed via the displacements of the deformed half-space in the finite element model with cohesive zones representing the active slip-systems (Fig. 4.9c). In the absence of active dislocation sources, i.e. $\Sigma 11(113)$ and $\Sigma 3(111)$, these separation distributions are computed from a finite element half-

space without cohesive zones. Then, the traction energy defined by $\int \boldsymbol{u} \cdot \boldsymbol{t}\, dx_1$, accounting for contributions from both the upper and lower half-spaces (grains), represents the energy contribution from the local disruption in the bulk crystallographic arrangement of atoms outside the core structure of the grain boundary (e.g. outside of the dashed yellow and green lines in Fig. 4.7-ii and Fig. 4.8-ii). This traction energy is primarily responsible for the generation of (a) an elastic stress-field which decays with distance from the boundary, as well as (b) a resolved shear stress along the $\langle 112 \rangle$ crystal orientations for grain boundaries with active dislocation sources.

In addition to the traction energy, there is also a structural energy component which can be delineated into the structural energies of the A, C, D and E SUs, as well as the stacking fault energy and dislocation core energy of any pre-existing b_1 partial. The core energy of the b_1 partials per unit (x_3) thickness is estimated to be $\mathrm{E}_{\mathbf{b}_1} = 140\ \mathrm{meV/Å}$ [101], while the stacking fault energy based on the GSFE of Ni is $\mathrm{E}_{\mathrm{SF}} = 2\ \mathrm{meV/Å}^2$. Calculating the structural energy contributions of the A, C, D, and E SUs is more complex. In reality, the energy of the individual SUs among different grain boundary structures may be different, since the SUs can have different degrees of distortion. For simplicity, the distortion effect is neglected and the structural energies of the C, D, and E SUs is assumed to primarily come from their core energies. The core energies of $\mathrm{E}_{\mathrm{C}} = 118\ \mathrm{meV/Å}$, $\mathrm{E}_{\mathrm{D}} = 1\ \mathrm{meV/Å}$, and $\mathrm{E}_{\mathrm{E}} = 275\ \mathrm{meV/Å}$ for the C, D, and E SUs are obtained respectively by subtracting the traction energies of the $\Sigma 11(113)$, $\Sigma 3(111)$, and $\Sigma 9(221)$ favored grain boundary structures from the MD-calculated grain boundary energies, and divide by the number of specific SUs. On the other hand, the A SU represents the perfect FCC lattice and has 0 core energy; its structural energy comes directly from elastic distortion along the grain boundary. Here, $\Sigma 33(441)$ grain boundary structure, which has 4 A-SUs and 2 E-SUs per d_p, is chosen as representative of the typical extent of distortion of the A-SUs across the remaining grain

boundaries, and I calculate the structural energy of the A-SU to be $E_A = 61\ meV/Å$. Note that my predictions of the grain boundary energies in Fig. 4.13 are exact for $\Sigma 11(113)$, $\Sigma 9(221)$, $\Sigma 3(111)$, and $\Sigma 33(441)$, since the calculation of the structural energies of the A, C, D, and E SUs comes directly from the MD-calculated grain boundary energies of these structures. More importantly, the grain boundary energy predictions, based on combinations of the traction and structural energies, are also in very good agreement with MD simulation results for the remaining twelve grain boundary structures.

The combined contribution of the structural and traction energies then consititues the global descriptor – the grain boundary energy, as shown in Fig. 4.13. Observe that the structural energy is a major component of the grain boundary energy, but this component is not directly responsible for emission of dislocations from the grain boundary structure. Even from the traction energies, one cannot discern if the grain boundary structures are ductile or brittle, thus local grain boundary descriptors are required. This explains the poor correlation between grain boundary energy and the mechanical properties [21, 27].

4.5.2 Tension-Compression Asymmetry

The tension-compression asymmetry in the stress required for dislocation nucleation from symmetric-tilt grain boundaries has previously been attributed to both the role of the resolved stress normal to the slip-planes, and the structure of the grain boundary. My results suggest that the resolved normal stress plays only a supporting role in the tension-compression asymmetry response of the grain boundary. Instead, it is the traction distributions representing the local atomic structure along the grain boundary that are primarily responsible for the asymmetrical strength of the boundary under tension and compression. The origin of dislocation emission along the

boundary, and the resolved shear stress contributions from the disruption in atomic arrangement along boundary τ_{GB}, can be quantitatively ascertained from the grain boundary traction signatures. When τ_{GB} acts in the direction of the resolved shear stress contribution from external loading τ_{ext}, dislocations are readily emitted at lower stresses. When τ_{GB} opposes τ_{ext}, the grain boundaries can then sustain much higher stresses prior to dislocation emission. This dependence of the direction of τ_{ext} with respect to τ_{GB} explains why certain grain boundary orientations ($\theta > 120°$) readily emit dislocations under uniaxial tension but not compression, while others ($\theta < 50°$) instead readily emit dislocations under uniaxial compression but not tension.

The traction signatures along the equilibrium grain boundary structures, and the associated dislocation nucleation sites with high τ_{GB}, are closely related to the structural units (SUs) along the boundary. The C SUs have no active dislocation source under uniaxial tensile or compressive load, since they are lattice dislocations with $\frac{1}{2}[110]$cores in the out-of-plane direction [102]. The ready emission of Shockley partials for $\theta > 120°$ grain boundaries under tension consistently initiates from the E-SUs along the boundary, or in the case of $\Sigma 33(554)$, from pre-existing dislocations dissociated from E-SUs along the boundary. For $\theta < 50°$ grain boundaries, however, the ready emission of Shockley partials under compression consistently initiates from highly distorted A-SUs along the boundary. The E-SUs are porous regions along the boundary, and the weakened atomic bonding within the E-SUs infers low dislocation nucleation strength under tension loading. In contrast, distorted A-SUs represent high local atom density regions along the boundary. The build-up of stress concentration at these high local density sites under compression causes the ready emission of dislocations to relief the stress, which transforms the short diagonal of the rhombic A-SU (as viewed in the $\langle 110 \rangle$orientation) to become the long diagonal and conversely the long diagonal to become the short one. Similar observations have been made in the

uniaxial compression of E-SU-containing grain boundaries, where atomic reconfigurations associated with the collapse of the E-SUs transform each E-SU into two distorted A-SUs (Fig. 4.11a, Fig. 4.12a-i), from which dislocations are emitted.

Finally, the results also suggest that the tension-compression asymmetry in the stress for dislocation nucleation may be limited to symmetrical-tilt grain boundaries. Because of the short structural length d_p of these boundaries, only a small number of repeated SUs can lie within each d_p as shown in Fig.4.2. This severely limits the number of potential dislocation nucleation sites (A- or E-SUs) within each grain boundary period, each with its own preference for dislocation emission under tension (E-SU) or compression (A-SU). Nevertheless, it is possible for low-density E-SUs and highly-distorted, denser A-SUs to coexist along grain boundaries with sufficiently large d_p, which would pave the way for the ready emission of dislocations under both tension and compression.

4.6 Figures

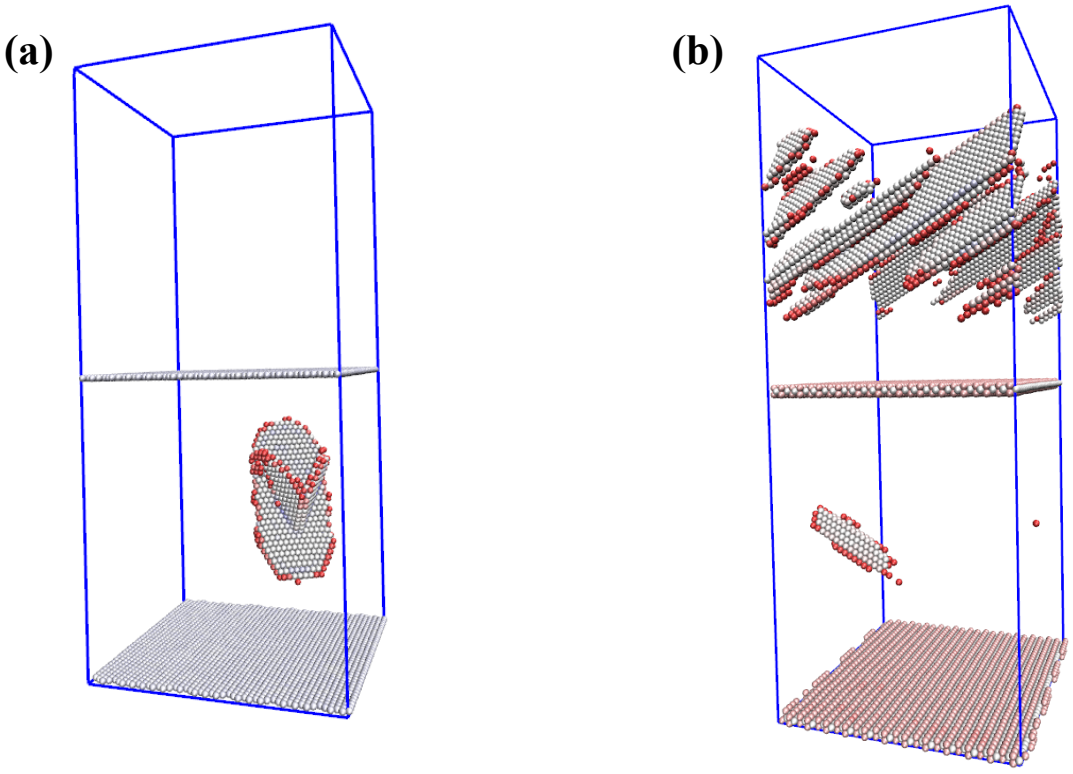

Figure 4.1 Deformed atomic configurations of (a) Σ3(111) and (b) Σ11(113) grain boundaries under uniaxial tensile load. structures are filtered based on the CSP values to display only non-FCC atoms, with dislocations colored in red and stacking faults colored in white. The dislocations are first emitted from perfect crystal bulk. Similar observations are found in uniaxial compression tests.

Name	Atomic Structure	Tilt Angle	Periodic Length d_p (nm)	Structure Units
Σ33(118)	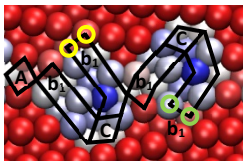	20.1°	2.02	2C+1A+4b_1
Σ19(116)	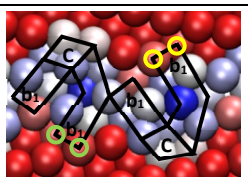	26.5°	1.53	2C+4b_1
Σ27(115)	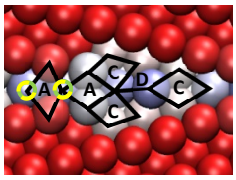	31.6°	1.29	3C+2A+D
Σ9(114)	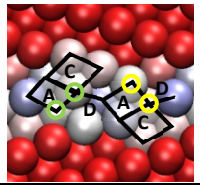	38.9°	1.06	2C+2A+2D
Σ33(554)	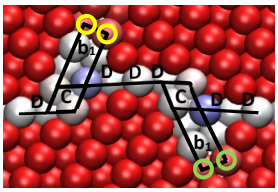	121.0°	2.02	2C+2b_1+6D
Σ11(332)	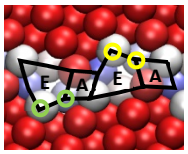	129.5°	1.17	2E+2A

Figure 4.2 Repeated structural units of periodicity d_p along symmetrical-tilt <110> Ni grain boundaries. The grain boundary structures are colored by the CSP values, with FCC atoms in red, dislocation cores in white, and stacking faults in blue. Initiation sites for ready-emission of $\boldsymbol{b_1}$ Shockley partials into the upper and lower grains under applied uniaxial compression are marked by open yellow and green circles.

Name	Atomic Structure	Tilt Angle	Periodic Length d_p (nm)	Structure Units
Σ9(221)	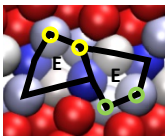	141.1°	0.75	2E
Σ27(552)	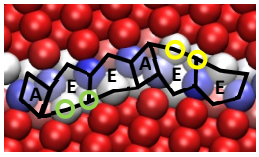	148.4°	1.83	4E+2A
Σ19(331)	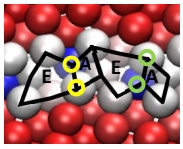	153.5°	1.09	2E+2A
Σ33(441)	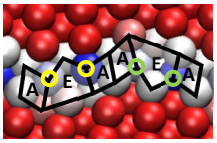	160.0°	1.43	2E+4A

Figure 4.2 (cont.) Repeated structural units of periodicity d_p along symmetrical-tilt <110> Ni grain boundaries. The grain boundary structures are colored by the CSP values, with FCC atoms in red, dislocation cores in white, and stacking faults in blue. Initiation sites for ready-emission of $\boldsymbol{b}_1$ Shockley partials into the upper and lower grains under applied uniaxial compression are marked by open yellow and green circles.

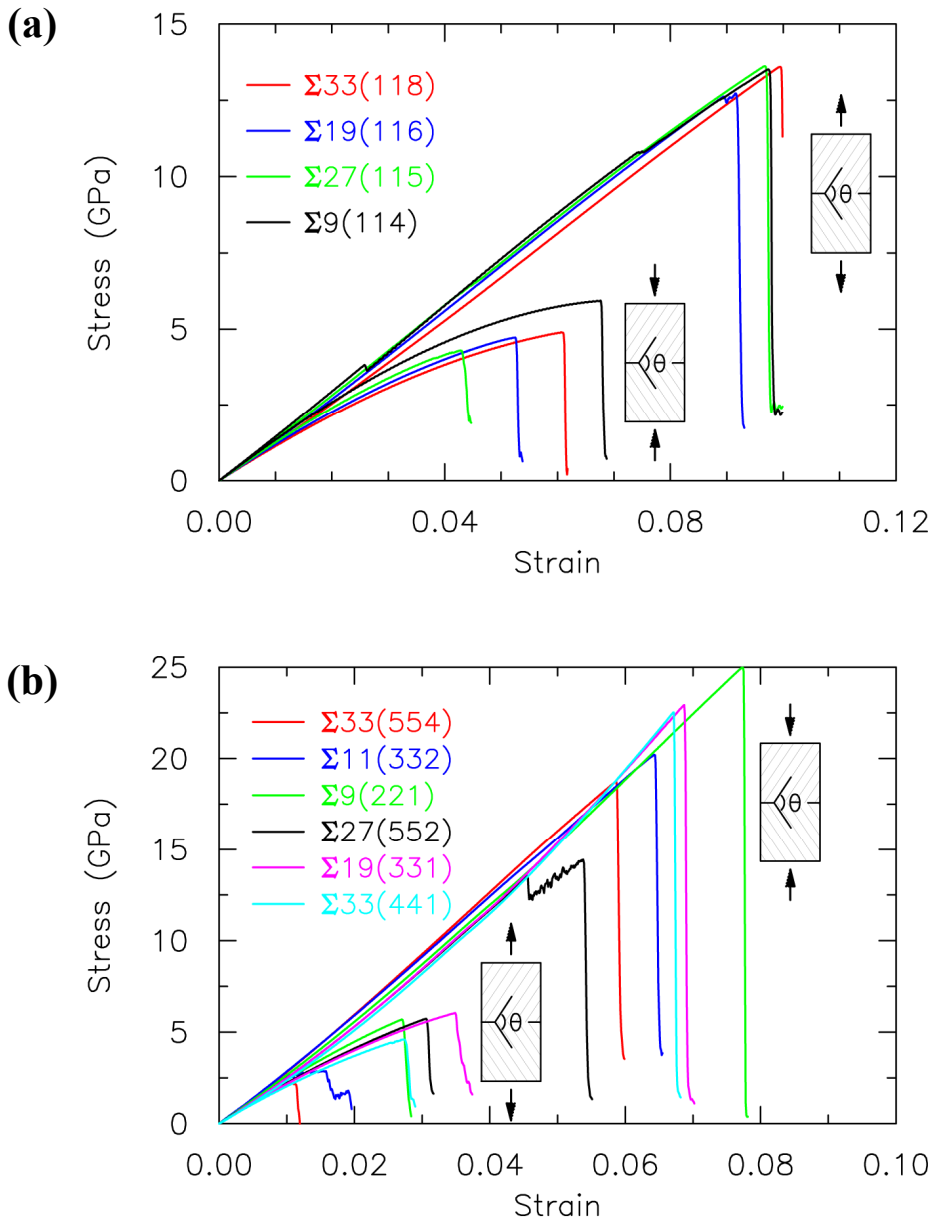

Figure 4.3 Stress-strain relationships for symmetrical-tilt <110> Ni grain boundaries with tilt angles of(a) $\theta < 50°$ and(b) $\theta > 120°$ under uniaxial tension and compression.

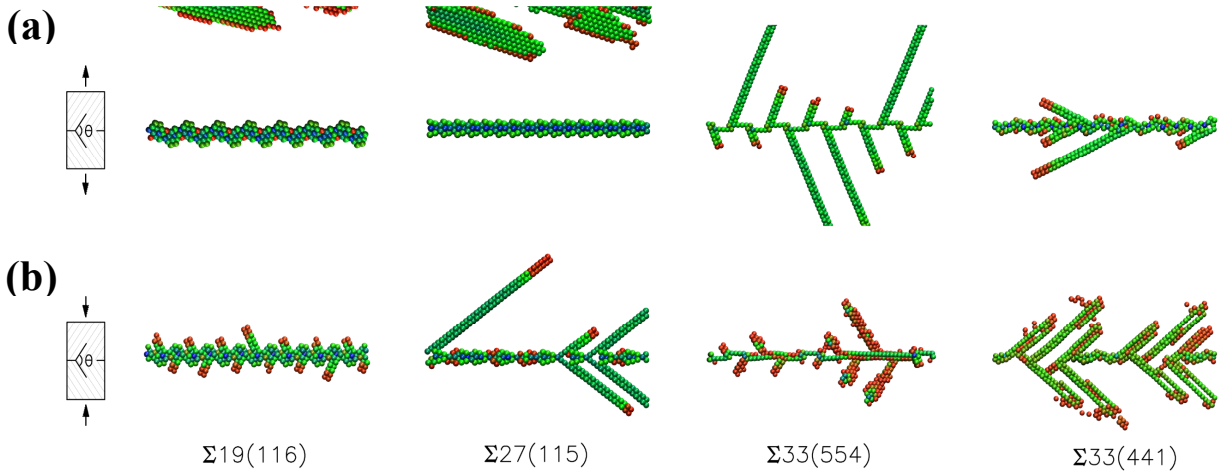

Figure 4.4 Deformed atomic configurations of four typical symmetrical-tilt <110> Ni grain boundaries at the peak tensile (a) and compressive (b) strength corresponding to the instant of dislocation emission; structures are filtered based on the centro-symmetric parameter to display only non-FCC atoms, with dislocations colored in red and stacking faults colored in green.

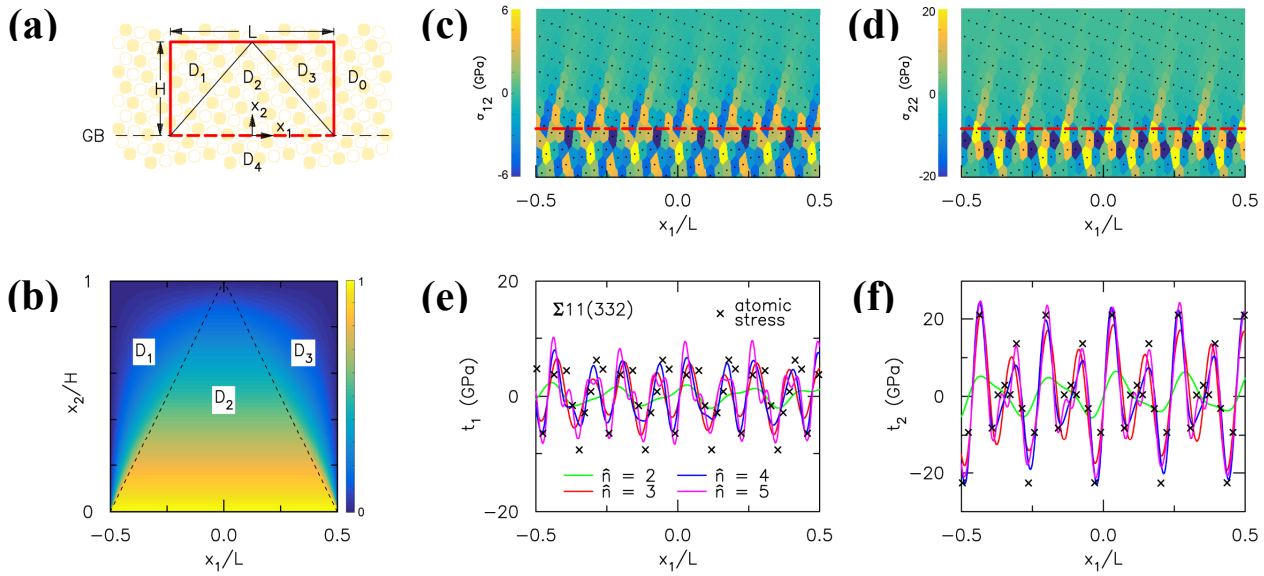

Figure 4.5 Atomic field projection method. (a) Calculation domain of the field projection scheme using atomic stress information in the vicinity of the grain boundary to reconstruct the continuum-equivalent grain boundary tractions. (b) Perturbation-displacement envelope function $F(x_1, x_2)$. (c) Contours of the σ_{12} stress in the upper grain of a Σ11(332) grain boundary structure. (d) Contours of the σ_{22} stress in the upper grain of a Σ11(332) grain boundary structure. Local atomic stresses in (c) and (d) are averaged over the Voronoi cell around each atom. (**e**) Field-projected shear tractions (t_1) along the grain boundary with increasing Fourier terms ($\hat{n}$). (**f**) Field-projected normal tractions (t_2) along the grain boundary with increasing Fourier terms ($\hat{n}$). Cross symbols in (**e**) and (f) denote atomic stress values within 1.5 Å from the boundary.

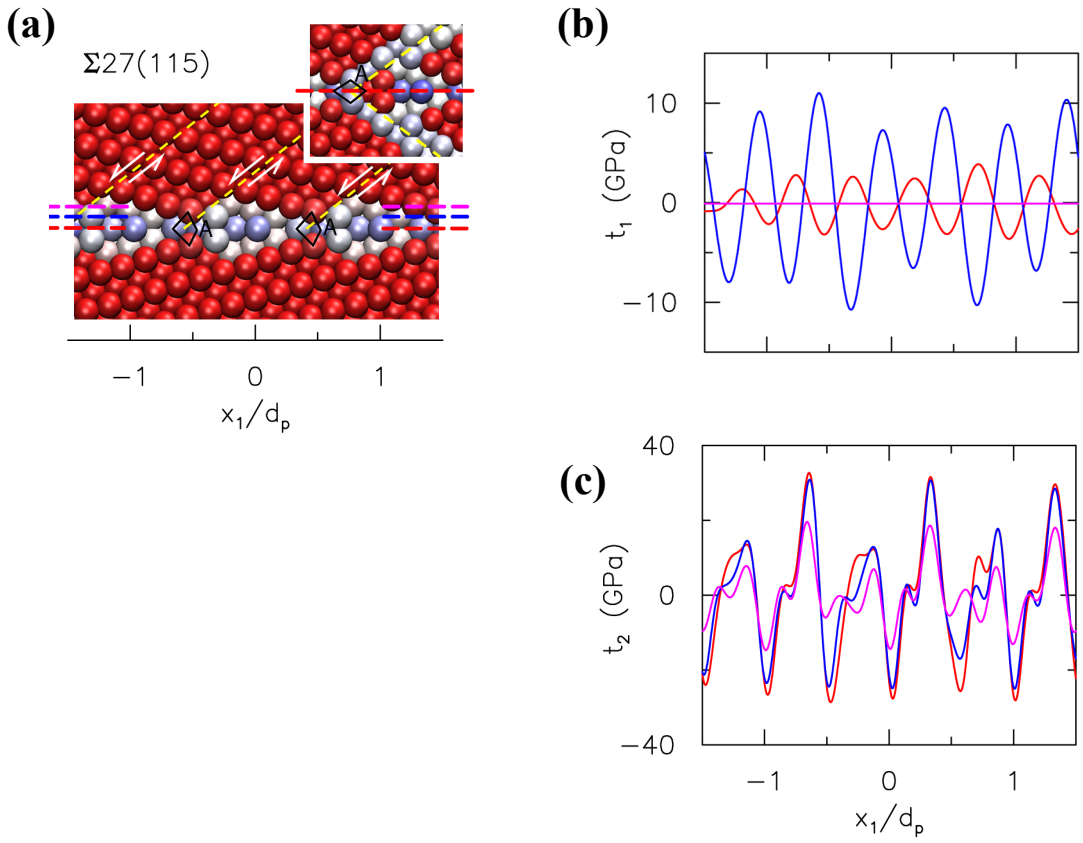

Figure 4.6 (a) Equilibrium atomic configuration of the Σ27(115) grain boundary; yellow dashed lines denote the active slip planes under uniaxial compression, with the deformed atomic configuration in the inset. (b, c) Field-projected shear t_1 (b) and normal t_2 (c) tractions along the corresponding colored dashed lines in (a).

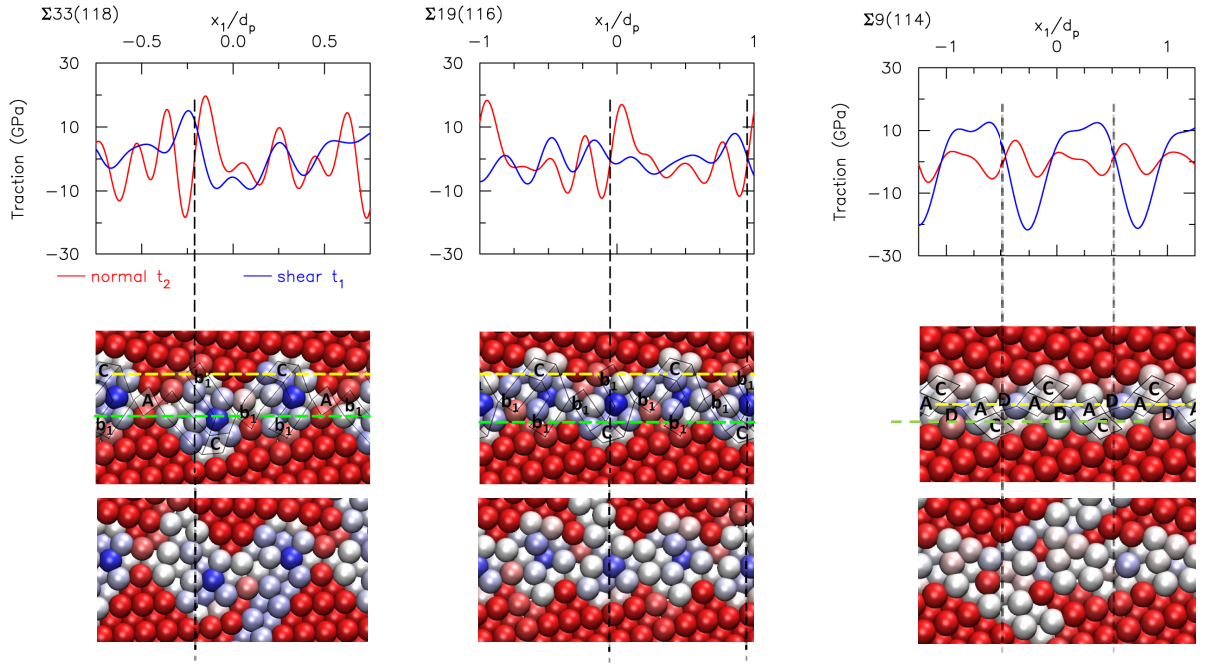

Figure 4.7 Traction-signatures along brittle grain boundaries of $\theta < 50°$: normal and shear traction distributions with corresponding atomic configuration of the equilibrium grain boundary structure; traction distributions are calculated along the yellow dashed lines.

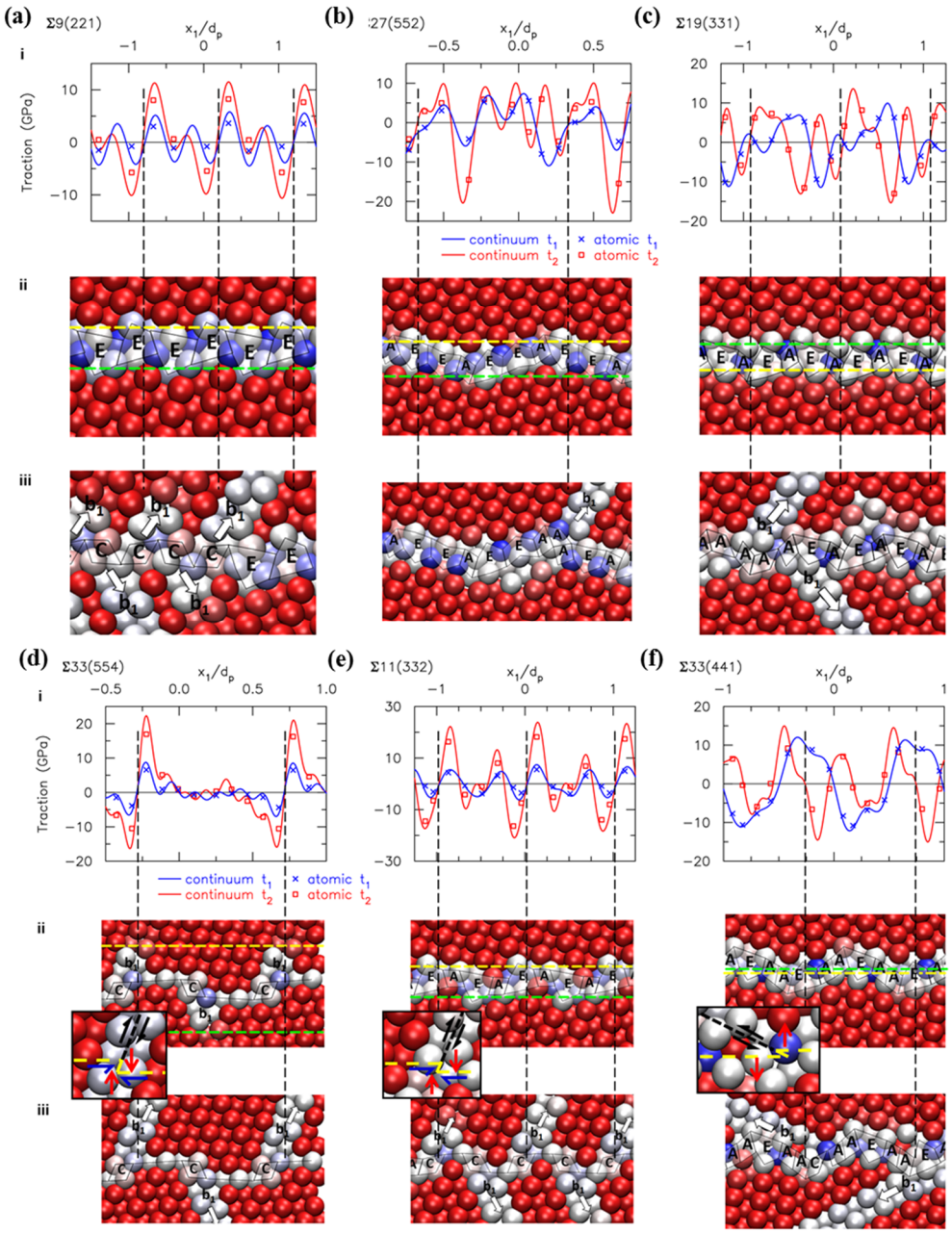

Figure 4.8 Traction signatures of (a) $\Sigma 9(221)$, (b) $\Sigma 27(552)$, (c) $\Sigma 19(331)$, (d) $\Sigma 33(554)$, (e) $\Sigma 11(332)$, and (f) $\Sigma 33(441)$grain boundaries. (i) Normal and shear traction distributions (lines), which are averaged over the atomic spacing to obtain atomic-scale tractions (symbols). (ii) Atomic configurations of equilibrium grain boundary structure. (iii) Atomic configurations of grain boundary structure at the first instant of partial emission. Atoms are colored by CSP values. Close-up views in the insets of (d), (e), and (f) (ii): red and blue arrows denote the normal and shear tractions on atom pairs at the origin of dislocation slip; black arrows denote the resolved shear stress contribution from the grain boundary tractions.

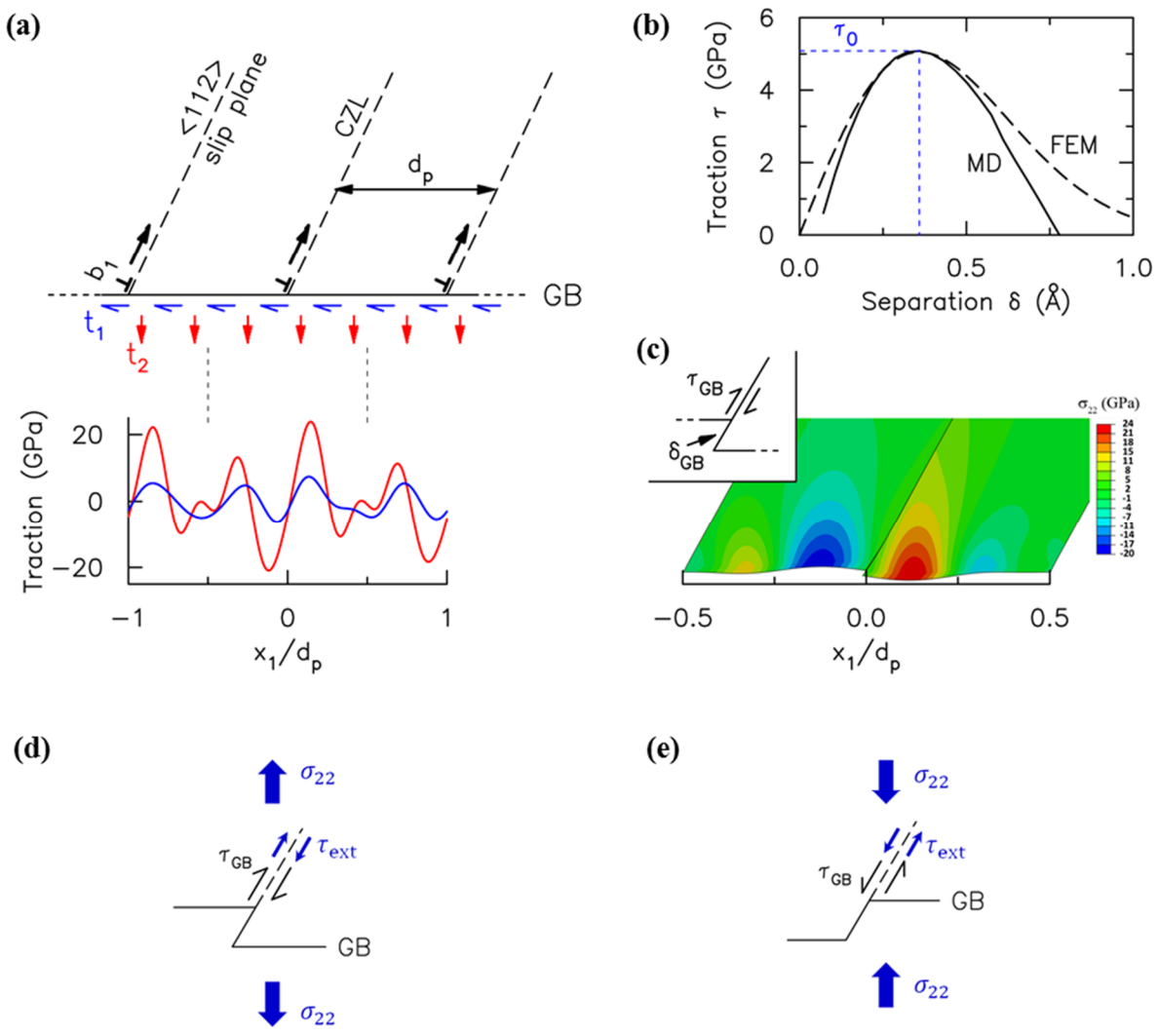

Figure 4.9 Resolved shear stress contributions from grain boundary tractions. (a) Schematic of the finite element model of an upper half-space with imposed grain boundary tractions to represent the upper grain; cohesive zone laws (CZL) along the emission path account for slip of the b_1 partials. (b) Cohesive zone law calibrated from MD for slip of a b_1 partial in the $\langle 112 \rangle$ direction. (c) Finite element calculations of the deformed geometry of the equilibrium $\Sigma 11(332)$ grain boundary structure with displayed contours of the σ_{22} stress; schematic of the resolved shear stress τ_{GB} and associated sliding-separation δ_{GB} along the slip plane in the inset. (d) Illustration showing the ready emission of dislocations only when τ_{GB} acts in the same direction as the resolved shear stress contribution from external loading τ_{ext}.

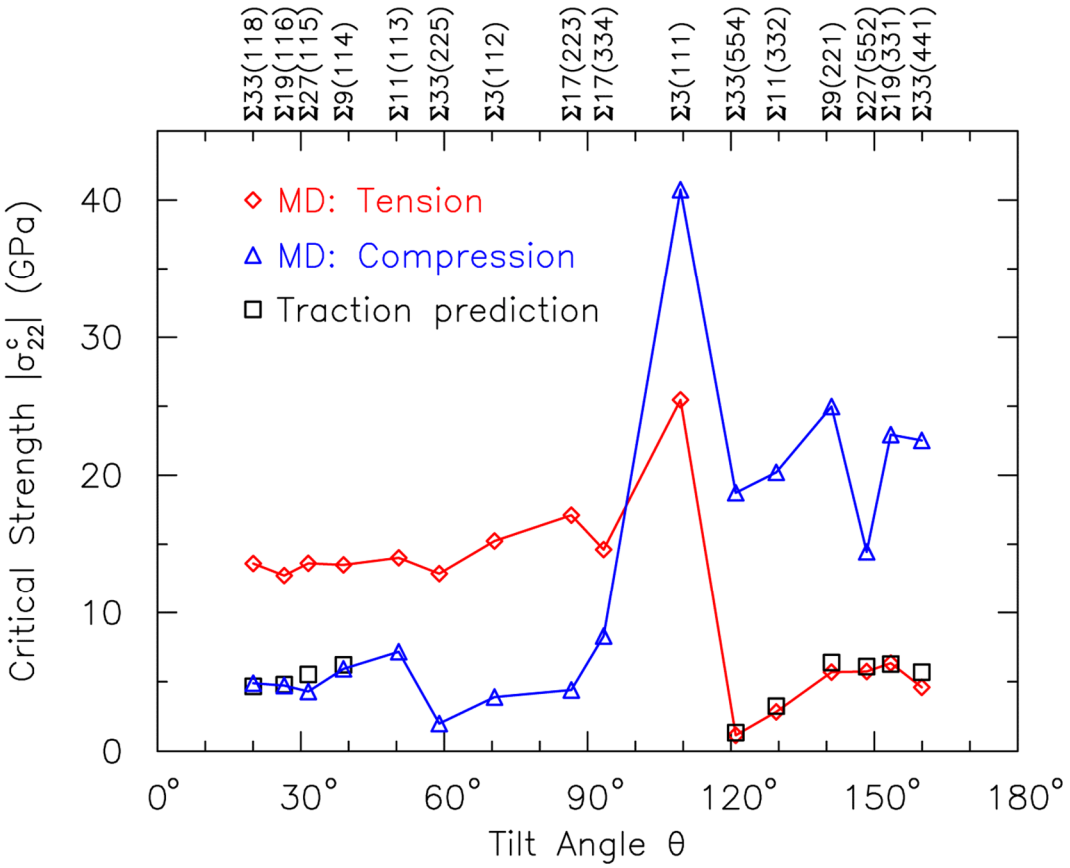

Figure 4.10 Summary of the critical tensile (red symbols) and compressive (blue symbols) strength of symmetrical-tilt ⟨110⟩ Ni grain boundaries from MD, and corresponding predictions (black symbols) from the traction signatures of the equilibrium grain boundary structures.

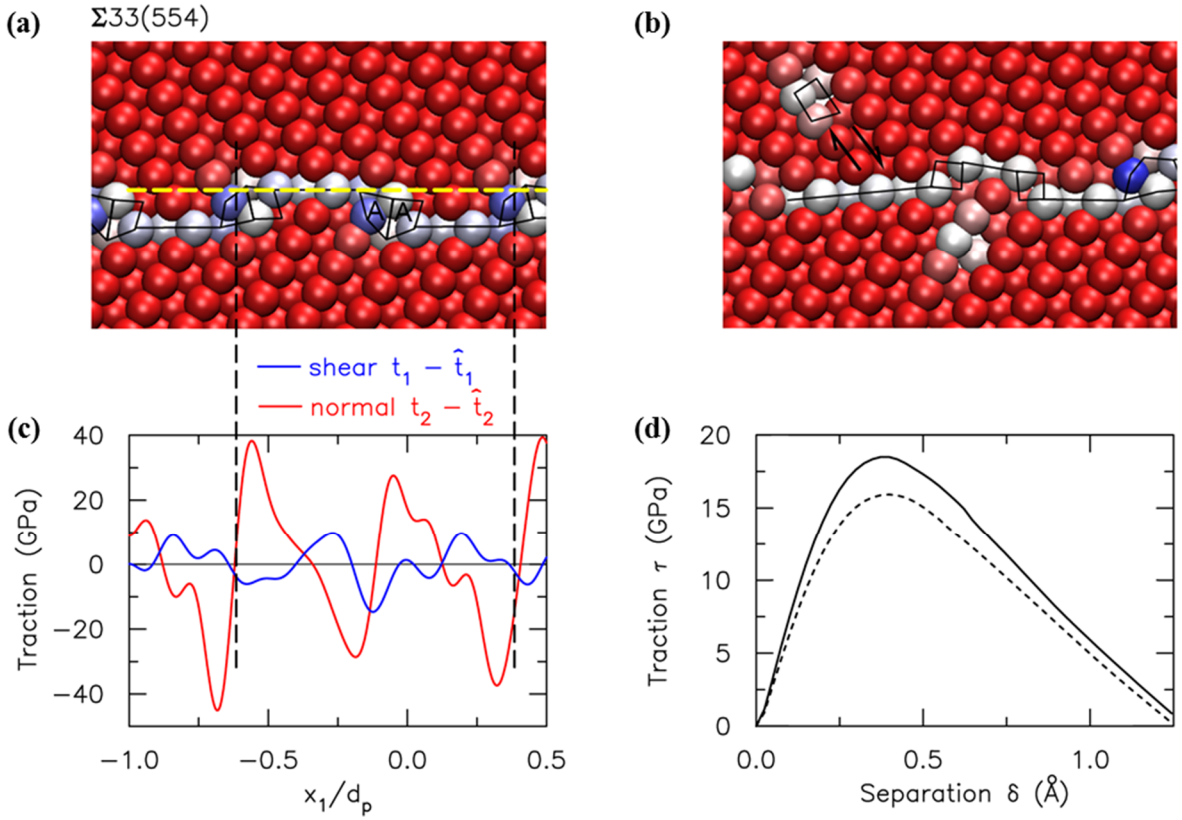

Figure 4.11 (a, b) Deformed atomic configurations of the Σ33(554) grain boundary under uniaxial compression, just prior to (a) and at the instant of (b) full dislocation emission. (c) Traction signatures along the deformed grain boundary structure corresponding to (a). (d) Traction separation laws for non-Schmid {001}⟨110⟩ dislocation slip in the absence of normal [001] stresses (dashed line), and at the stress-state corresponding to (a) (solid line).

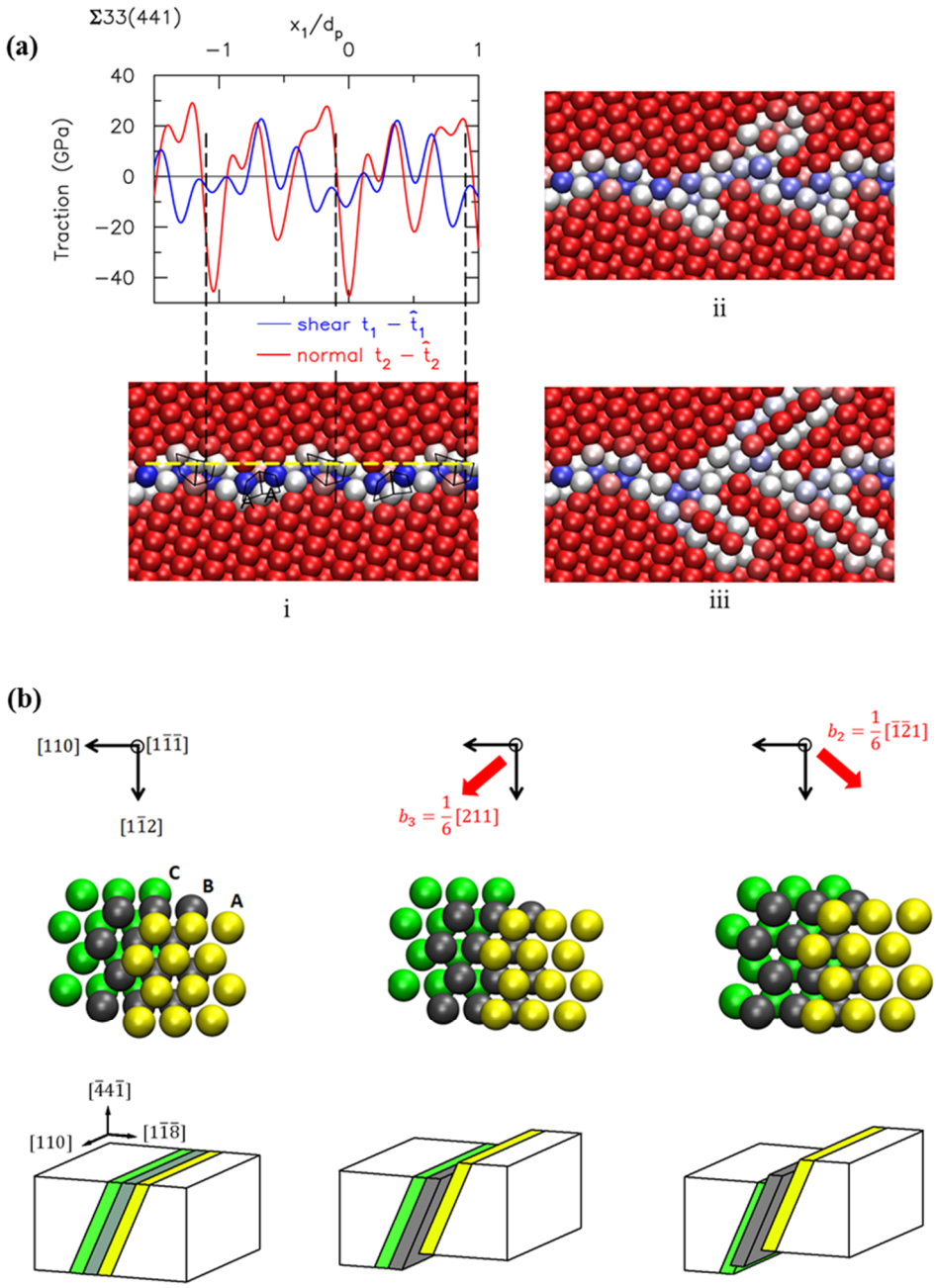

Figure 4.12 (a) Deformed atomic configurations depicting sequence of out-of-plane partial dislocation emissions to form extrinsic stacking faults for Σ33(441) grain boundary under uniaxial compression, with traction signatures of the deformed grain boundary structure in (i) just prior to dislocation emission. (b) Top view and schematic representation of the stacking arrangements of {111} planes during the partial dislocation emission processes corresponding to (a).

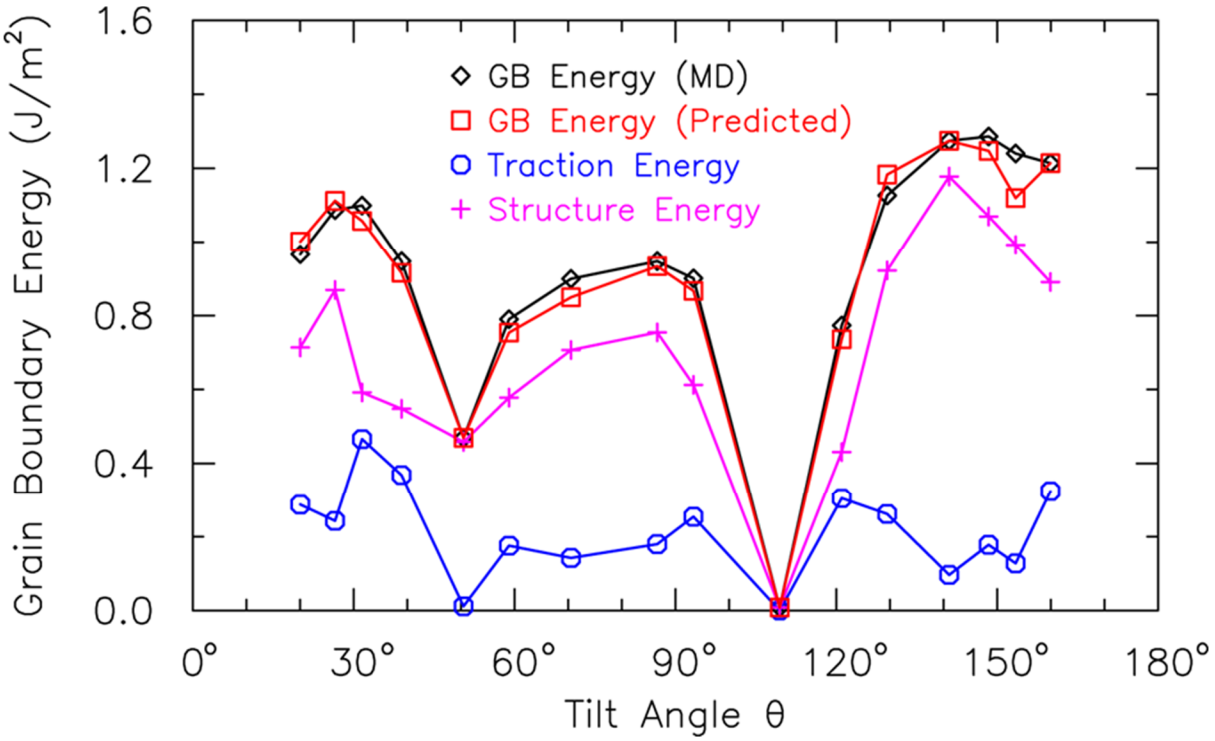

Figure 4.13 Grain boundary energy of the Ni ⟨110⟩ symmetrical-tilt grain boundary structures, delineated into traction and structural energy contributions.

Chapter 5. Conclusion and Future Work

5.1 Conclusion

My research centers on quantifying the interface deformation mechanics in nanostructured metals using both atomic simulations and continuum traction signatures. The major findings of my thesis research are summarized below:

Elucidated with molecular dynamics (MD) simulations, the first part of my research focuses on the complex interface-dominant deformation mechanisms in nanoscale Cu-Ag and Cu-Al multilayered metals. In Cu-Ag nanolayered metals, my results uncover a novel mechanism responsible for the abrupt transition of the initially planar Cu-Ag nanolayers to become wavy during uniaxial tensile deformation normal to the Cu-Ag interface. Activation of this planar-to-wavy interlayer transition mechanism is facilitated by the unique structure of the semi-coherent Cu-Ag interface, which permits interface sliding between the Cu and Ag interlayers to simultaneously accommodate the out-of-plane deformation, and to redistribute misfit dislocations to relax the bending stress associated with the wavy structure. In Cu-Al nanolayers, however, the unique Cu-Al interface structure results in the formation of closed and open stacking fault tetrahedra (SFT) during tensile deformation. These SFTs originate from the concurrent nucleation of Shockley partials from the dissociated misfit dislocations along the Cu-Al interfaces under tensile deformation. The final deformed configuration comprises closed SFTs within the Cu interlayers, as well as open-ended SFTs within the Al interlayers, which are all tied to the Cu-Al interfaces. The distinct interface-dominant deformation mechanisms for Cu-Ag and Cu-Al nanolayers are found to be associated with the contrasting shear-slip resistance of the respective interfaces. Specifically, the relative low shear resistance along Cu-Ag interface facilitates planar-

to-wavy transition in Cu-Ag nanolayers, while the Cu-Al interlayers remain planar due to the strong barrier energy for shear-slip and the strong bonding between the Cu and Al interlayers leads to the formation of SFTs. The planar-to-wavy transition of the Cu-Ag nanolayers introduces high stress concentrations at the summits and valleys of the wavy interfaces, which are the initiation sites for the emission of micro-twinning partials. On the other hand, the network of open and closed SFTs along the Cu-Al interfaces introduces significant strain hardening. The competition between the interlayer thickness and the waviness wavelength for Cu-Ag nanolayers or size of the SFTs for Cu-Al nanolayers, ultimately controls the macroscopic strength of the respective nanolayered metals.

The second part of my thesis focuses on the development of quantitative descriptors capable of predicting and quantifying the deformation mechanics without postdictive MD simulations. Using symmetrical-tilt <110> Ni grain boundaries as a model system, an atomic field projection method based on the virtual work principle is developed to reconstruct continuum-equivalent traction fields from atomic stress information. Criteria based on traction signatures are proposed to predict the critical stress for the emission of dislocations from these grain boundaries under applied tension and compression. The results are in perfect agreement with postdictive MD simulations, suggesting that the grain boundary tractions are indeed local descriptors of the grain boundary atomic structure. The grain boundary traction signatures are used to explain the relationship between the atomic structure of the grain boundary and the observed tension-compression asymmetry in the stress required for dislocation nucleation from symmetric-tilt grain boundaries. In addition, the grain boundary signatures are used to explain the formation of extrinsic stacking faults or the emission of non-Schmid full dislocations from certain grain boundary structures under compression.

5.2 Future Work

My thesis research introduces the notion of traction signatures as quantitative interface descriptors, which have been applied to predict grain boundary dislocation emission. The traction signatures can potentially be used to establish the relationship between the atomic structure of the grain boundary structure and its propensity to impede, absorb, or transmit dislocations. This method is also broadly applicable to more complex interface structures, such as semi-coherent interfaces elucidated in the first part of my research. Therefore, my thesis is expected to be extended towards two specific directions:

1. Dislocation-grain boundary interaction

In addition to the emission of dislocations from grain boundaries, the interaction of newly-emitted or pre-existing dislocations with the grain boundary plays an important role in the strengthening mechanisms in nanocrystalline metals. To demonstrate the dislocation-grain boundary interaction process, bilayer models of symmetrical-tilt ⟨110⟩ Ni grain boundaries are created in MD, as shown in Fig. 5.1 for Σ9(221) grain boundary. A larger grain size is assumed for the lower grain ($10\times14\times10nm^3$) compared to the upper one ($10\times6\times10nm^3$) to accommodate the presence of two pre-existing partial dislocations. These partial dislocations are introduced by deleting a group of 5 atoms along the $(\bar{1}1\bar{1})$ plane in the $[1\bar{1}\bar{2}]$ direction to create a full dislocation dipole and the model is subjected to energy minimization. After minimization, the full dislocations are dissociated into Shockley partials; two of the Shockley partials along the $(\bar{1}1\bar{1})$ plane ($\frac{1}{6}[1\bar{1}\bar{2}]$ and $\frac{1}{6}(\bar{1}12)$) cancel out, while the remaining two ($\frac{1}{6}[\bar{1}1\bar{2}]$and $\frac{1}{6}[1\bar{1}2]$) reside along $(\bar{1}11)$ planes. The application of tensile loading then causes the $\frac{1}{6}[\bar{1}1\bar{2}]$ and $\frac{1}{6}[1\bar{1}2]$ partials to glide towards and interact with the grain boundary interfaces. Interesting interaction

mechanisms have been observed for dislocations gliding towards different parts of the grain boundary. As an example, Fig. 5.2 shows the interactions of incoming partials with Σ19(331) grain boundary surface taken at $\varepsilon_{22} = 1.8\%$. By introducing Shockley partials along two different close-packed planes, the incoming dislocations can interact with varying SUs along the grain boundary structure within its periodic length d_p. Observe in Fig. 5.2a that the Shockley partial gets transmitted through the grain boundary and glides in another <112> direction thereafter. In contrast, Fig. 5.2b shows that the incoming Shockley partial three atomic layers away from that in Fig. 5.2a is impeded by the boundary surface, with no transmission observed. This phenomenon indicates that the interaction between grain boundary and incoming dislocations are not only affected by the grain orientation, but also by the inhomogeneous atomic structure of the grain boundary. Examining the evolving grain boundary tractions as the Shockley partial approaches and interacts with the boundary could provide important insights into how the atomic structure or SUs along the boundary impedes, absorbs, or transmits dislocations. Direct quantification of the probability of slip transmission based on the traction signatures can be useful in higher-scale dislocation dynamics modeling of the grain boundary structure.

2. Traction signatures of 2D heterogeneous interfaces

Symmetrical-tilt grain boundary structures are one-dimensional (1D) in general. The semi-coherent heterogeneous interfaces, such as the Cu-Ag and Cu-Al model systems, however, have two-dimensional (2D) interlayer interface structures, with more complex, tri-axial, local stress field. Fig. 5.3 displays the σ_{22} component of the virial stress of Cu and Ag atoms along the cube-on-cube Cu-Ag interlayer interface. Observe that σ_{22} is positive at the triangular stacking fault planes, while σ_{22} is negative at the dissociated misfit dislocations. Additionally, the stress distributions are different between Cu and Ag layers. All these interesting findings are expected to

be interpreted by the varying 2D traction signatures along the interlayers, which is easy to obtain by extending the 1D atomic field projection to 2D. The traction signatures could also provide predictive insights into the process of unique dislocation structures (e.g. SFTs) to be formed, as well as the critical stress to trigger the formation of these structures. Note that the 2D traction signatures include the stress information of atoms in the vicinity of interfaces. Therefore, they account for both the atomic structure of the interlayer boundary and the coherency stress within the interlayers.

5.3 Figures

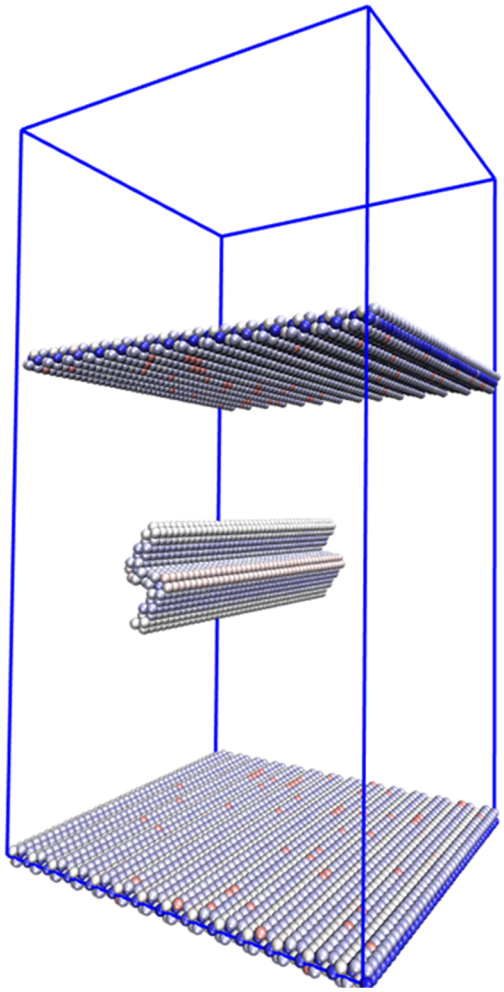

Figure 5.1 Atomic configuration of $\Sigma 9(221)$grain boundary model with inserted pre-existing partial dislocations. The atoms are filtered with CSP values where only non-FCC atoms are displayed.

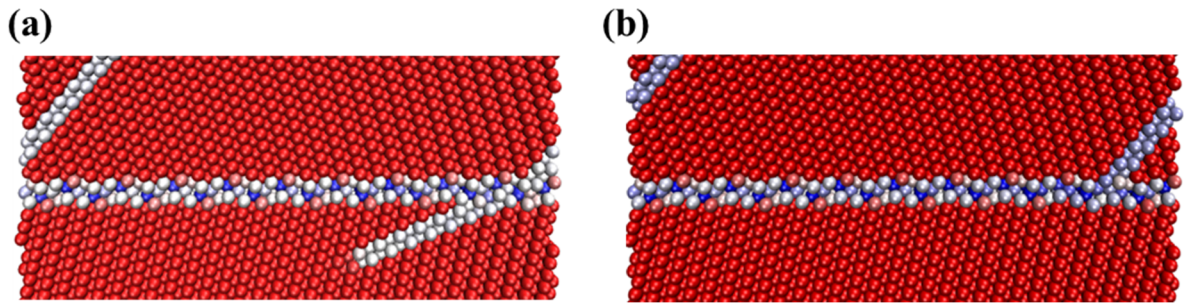

Figure 5.2 Atomic configuration of $\Sigma 19(331)$ grain boundary with incoming dislocations interact at different sites. The atoms are colored with CSP values where FCC atoms are in red while non-FCC atoms are in white to blue.

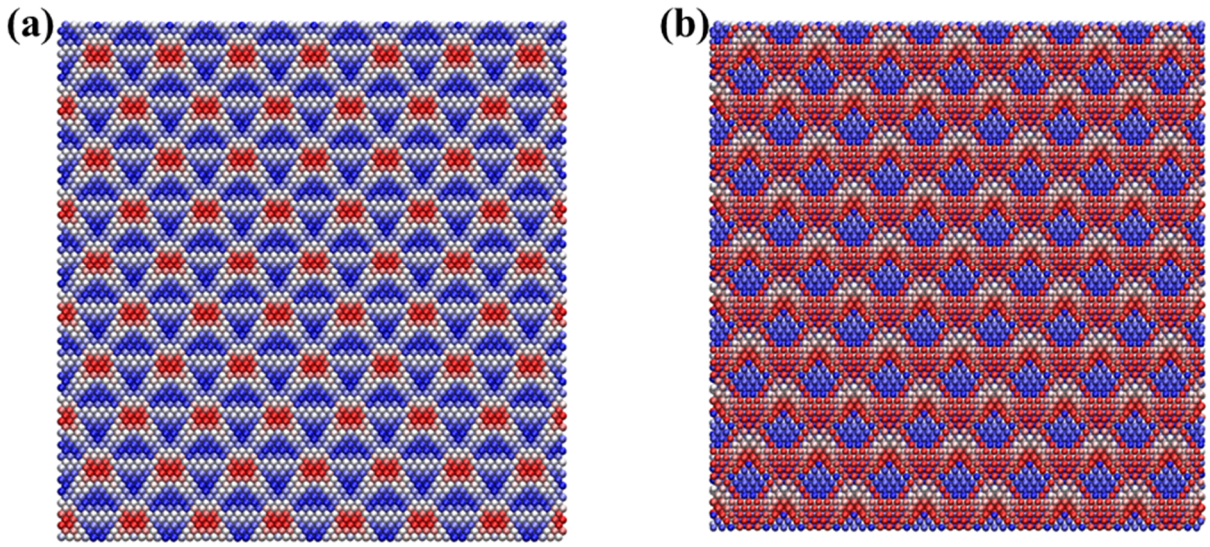

Figure 5.3 Atomic virial stress of atoms along Cu-Ag interfaces. (a) normal stress (σ_{22}) in Cu; (b) normal stress (σ_{22}) in Ag.

References

1. Anderson, P. M., Foecke, T., & Hazzledine, P. M. (1999). Dislocation-based deformation mechanisms in metallic nanolaminates. *MRS Bulletin*, 24(02), 27-33.
2. Wang, J., & Misra, A. (2011). An overview of interface-dominated deformation mechanisms in metallic multilayers. *Current Opinion in Solid State and Materials Science,* 15(1), 20-28.
3. Van Swygenhoven, H. (2002). Grain boundaries and dislocations. Science, 296(5565), 66-67.
4. Tench, D., & White, J. (1984). Enhanced tensile strength for electrodeposited nickel-copper multilayer composites. *Metallurgical Transactions A,* 15(11), 2039-2040.
5. Kacher, J., Eftink, B. P., Cui, B., & Robertson, I. M. (2014). Dislocation interactions with grain boundaries. *Current Opinion in Solid State and Materials Science,* 18(4), 227-243.
6. Hull, D., & Bacon, D. J. (2001). *Introduction to dislocations*. Butterworth-Heinemann.
7. Hall, E. O. (1951). The deformation and ageing of mild steel: III discussion of results. *Proceedings of the Physical Society. Section B,* 64(9), 747.
8. Petch, N.J. (1953). The Cleavage Strength of Polycrystals. *Journal of the Iron and Steel Institute,* 173, 25–28.
9. Misra, A., Hirth, J. P., & Hoagland, R. G. (2005). Length-scale-dependent deformation mechanisms in incoherent metallic multilayered composites. *Acta Materialia,* 53(18), 4817-4824.
10. Yamakov, V., Wolf, D., Phillpot, S. R., Mukherjee, A. K., & Gleiter, H. (2002). Dislocation processes in the deformation of nanocrystalline aluminium by molecular-dynamics simulation. *Nature Materials,* 1(1), 45-49.
11. Shan, Z., Stach, E. A., Wiezorek, J. M. K., Knapp, J. A., Follstaedt, D. M., & Mao, S. X. (2004). Grain boundary-mediated plasticity in nanocrystalline nickel. *Science,* 305(5684), 654-657.
12. Li, X., Wei, Y., Lu, L., Lu, K., & Gao, H. (2010) Dislocation nucleation governed softening and maximum strength in nano-twinned metals. *Nature,* 464(7290), 877-880.
13. Misra, A., & Krug, H. (2001). Deformation behavior of nanostructured metallic multilayers. *Advanced Engineering Materials,* 3(4), 217-222.
14. Kronberg, M. L., & Wilson, F. H. (1949) Secondary recrystallization in copper. *AIME TRANS,* 185, 501-514.

15. Grimmer, H., Bollmann, W., Warrington, D. H. (1974) Coincidence-site lattices and complete pattern-shift lattices in cubic crystals. *Acta Crystallographica, Section A: Crystal Physics, Diffraction, Theoretical and General Crystallography,* 30(2), 197-207.
16. Randle, V. (2001) The coincidence site lattice and the 'sigma enigma'. *Materials Characterization,* 47(5), 411-416.
17. Randle, V. (2004) Application of electron backscatter diffraction to grain boundary characterisation. *International Materials Reviews,* 49(1), 1-11.
18. Lim, L. C. (1987) Surface intergranular cracking in large strain fatigue. *Acta Metallurgica,* 35(7), 1653-1662.
19. Yang, S. L., Krupp, U., Christ, H. J., & Braz Trindade, V. (2005). The relationship between grain boundary character and the intergranular oxide distribution in IN718 superalloy. *Advanced Engineering Materials,* 7(8), 723-726.
20. Li, N., Wang, J. (2015) In-situ TEM Study of dislocation-interface interactions. *The Transmission Electron Microscope- Theory and Applications,* DOI: 10.5772/60880.
21. Olmsted, D. L., Foiles, S. M., & Holm, E. A. (2009). Survey of computed grain boundary properties in face-centered cubic metals: I. Grain boundary energy. *Acta Materialia,* 57(13), 3694-3703.
22. Sutton, A. P., & Vitek, V. (1983). On the structure of tilt grain boundaries in cubic metals I. Symmetrical tilt boundaries. *Philosophical Transactions of the Royal Society of London A: Mathematical, Physical and Engineering Sciences,* 309(1506), 1-36.
23. Rittner, J. D., & Seidman, D. N. (1996). <110> symmetric tilt grain-boundary structures in fcc metals with low stacking-fault energies. *Physical Review B,* 54(10), 6999.
24. Balluffi, R. W., & Bristowe, P. D. (1984). On the structural unit/grain boundary dislocation model for grain boundary structure. *Surface Science,* 144(1), 28-43.
25. McPhie, M. G., Berbenni, S., & Cherkaoui, M. (2012). Activation energy for nucleation of partial dislocation from grain boundaries. *Computational Materials Science,* 62, 169-174.
26. Mompiou, F., Caillard, D., Legros, M., & Mughrabi, H. (2012). In situ TEM observations of reverse dislocation motion upon unloading in tensile-deformed UFG aluminium. *Acta Materialia,* 60(8), 3402-3414.
27. Tschopp, M. A., Tucker, G. J., & McDowell, D. L. (2007). Structure and free volume of <110> symmetric tilt grain boundaries with the E structural unit. *Acta Materialia,* 55(11), 3959-3969.

28. Spearot, D. E., Tschopp, M. A., Jacob, K. I., & McDowell, D. L. (2007). Tensile strength of <100> and <110> tilt bicrystal copper interfaces. *Acta Materialia*, 55(2), 705-714.
29. Tschopp, M. A., Tucker, G. J., & McDowell, D. L. (2008). Atomistic simulations of tension–compression asymmetry in dislocation nucleation for copper grain boundaries. *Computational Materials Science,* 44(2), 351-362.
30. Sangid, M. D., Ezaz, T., Sehitoglu, H., & Robertson, I. M. (2011). Energy of slip transmission and nucleation at grain boundaries. *Acta Materialia,* 59(1), 283-296.
31. Freund, L. B., & Suresh, S. (2004). *Thin film materials: stress, defect formation and surface evolution.* Cambridge University Press.
32. Zang, L. *Lecture 21: Types of Interfaces: coherent, semi-coherent, and incoherent.* Retrieved from Lecture Notes Online Web site: http://www.eng.utah.edu/~lzang/images/lecture-21.pdf.
33. Demkowicz, M. J., Wang, J., & Hoagland, R. G. (2008). Interfaces between dissimilar crystalline solids. *Dislocations in Solids,* 14, 141-207.
34. Wang, J., Hoagland, R. G., Hirth, J. P., & Misra, A. (2008). Atomistic modeling of the interaction of glide dislocations with "weak" interfaces. *Acta Materialia,* 56(19), 5685-5693.
35. Phillips, M. A., Clemens, B. M., & Nix, W. D. (2003). Microstructure and nanoindentation hardness of Al/Al_3Sc multilayers. *Acta Materialia,* 51(11), 3171-3184.
36. McKeown, J., Misra, A., Kung, H., Hoagland, R. G., & Nastasi, M. (2002). Microstructures and strength of nanoscale Cu–Ag multilayers. *Scripta Materialia,* 46(8), 593-598.
37. Huang, H., & Spaepen, F. (2000). Tensile testing of free-standing Cu, Ag and Al thin films and Ag/Cu multilayers. *Acta Materialia,* 48(12), 3261-3269.
38. Verdier, M., Huang, H., Spaepen, F., Embury, J. D., & Kung, H. (2006). Microstructure, indentation and work hardening of Cu/Ag multilayers. *Philosophical Magazine,* 86(32), 5009-5016.
39. Li, J., Mei, J., Ni, Y., Lu, H., & Jiang, W. (2010). Two-dimensional quasicontinuum analysis of the strengthening and weakening effect of Cu/Ag interface on nanoindentation. *Journal of Applied Physics,* 108(5), 054309-054309.
40. Wang, J., Beyerlein, I. J., Mara, N. A., & Bhattacharyya, D. (2011). Interface-facilitated deformation twinning in copper within submicron Ag–Cu multilayered composites. *Scripta Materialia,* 64(12), 1083-1086

41. Kingstedt, O. T., Eftink, B., Lambros, J., & Robertson, I. M. (2014). Quasi-static and dynamic compressive deformation of a bulk nanolayered Ag–Cu eutectic alloy: Macroscopic response and dominant deformation mechanisms. *Materials Science and Engineering: A,* 595, 54-63.
42. Jiang, H. G., Dai, J. Y., Tong, H. Y., Ding, B. Z., Song, Q. H., & Hu, Z. Q. (1993). Interfacial reactions on annealing Cu/Al multilayer thin films. *Journal of Applied Physics,* 74(10), 6165-6169.
43. Guo, Y., Qiao, G., Jian, W., & Zhi, X. (2010). Microstructure and tensile behavior of Cu–Al multi-layered composites prepared by plasma activated sintering. *Materials Science and Engineering: A,* 527(20), 5234-5240.
44. Retrieved from Online Web site: http://nptel.ac.in/courses/113101003/parts/partII/module1/1.4.html.
45. Retrieved from Online Web site: http://www.matter.org.uk/glossary/detail.asp?dbid=367.
46. Zheng, S., Beyerlein, I. J., Carpenter, J. S., Kang, K., Wang, J., Han, W., & Mara, N. A. (2013). High-strength and thermally stable bulk nanolayered composites due to twin-induced interfaces. *Nature Communications,* 4, 1696.
47. Plimpton, S. (1995). Fast parallel algorithms for short-range molecular dynamics. *Journal of Computational Physics,* 117(1), 1-19.
48. Williams, P. L., Mishin, Y., & Hamilton, J. C. (2006). An embedded-atom potential for the Cu–Ag system. *Modelling and Simulation in Materials Science and Engineering,* 14(5), 817.
49. Apostol, F., & Mishin, Y. (2011). Interatomic potential for the Al-Cu system. *Physical Review B,* 83(5), 054116.
50. Ercolessi, F. (1997). A molecular dynamics primer. *Spring College in Computational Physics,* ICTP, Trieste, 19.
51. Kelchner, C. L., Plimpton, S. J., & Hamilton, J. C. (1998). Dislocation nucleation and defect structure during surface indentation. *Physical Review B,* 58(17), 11085.
52. Shao, S., Wang, J., Misra, A., & Hoagland, R. G. (2013). Spiral patterns of dislocations at nodes in (111) semi-coherent FCC interfaces. *Scientific Reports,* 3, 2448.
53. Umezawa, K., Nakanishi, S., Yoshimura, M., Ojima, K., Ueda, K., & Gibson, W. M. (2000). Ag/Cu (111) surface structure and metal epitaxy by impact-collision ion-scattering spectroscopy and scanning tunneling microscopy. *Physical Review B,* 63(3), 035402.

54. Zheng, S. J., Wang, J., Carpenter, J. S., Mook, W. M., Dickerson, P. O., Mara, N. A., & Beyerlein, I. J. (2014). Plastic instability mechanisms in bimetallic nanolayered composites. *Acta Materialia,* 79, 282-291.
55. Cheung, K. S., & Yip, S. (1991). Atomic-level stress in an inhomogeneous system. *Journal of Applied Physics,* 70(10), 5688-5690.
56. Li, R., & Chew, H. B. (2014). Deformation twinning and plastic recovery in Cu/Ag nanolayers under uniaxial tensile straining. *Philosophical Magazine Letters,* 94(5), 260-268.
57. Beyerlein, I. J., Mara, N. A., Bhattacharyya, D., Alexander, D. J., & Necker, C. T. (2011). Texture evolution via combined slip and deformation twinning in rolled silver–copper cast eutectic nanocomposite. *International Journal of Plasticity,* 27(1), 121-146.
58. Kolluri, K., Gungor, M. R., & Maroudas, D. (2008). Atomic-scale analysis of defect dynamics and strain relaxation mechanisms in biaxially strained ultrathin films of face-centered cubic metals. *Journal of Applied Physics,* 103(12), 123517.
59. Simpson, C. J., & Aust, K. T. (1972). Grain boundary migration. *Surface Science,* 31, 479-497.
60. Silcox, J., & Hirsch, P. B. (1959). Direct observations of defects in quenched gold. *Philosophical Magazine,* 4(37), 72-89.
61. Singh, B. N., Golubov, S. I., Trinkaus, H., Edwards, D. J., & Eldrup, M. (2004). Review: Evolution of stacking fault tetrahedra and its role in defect accumulation under cascade damage conditions. *Journal of Nuclear Materials,* 328(2), 77-87.
62. Kadoyoshi, T., Kaburaki, H., Shimizu, F., Kimizuka, H., Jitsukawa, S., & Li, J. (2007). Molecular dynamics study on the formation of stacking fault tetrahedra and unfaulting of Frank loops in fcc metals. *Acta materialia,* 55(9), 3073-3080.
63. Moroz, P. J., Polonis, D. H., & Taggart, R. (1969). Observation of linear arrays of stacking fault tetrahedra in quenched and aged alpha copper-germanium alloys. *Metallography,* 2(4), 385-389.
64. Shirai, Y., Furukawa, K., Takamura, J., Yamada, W., & Iwata, S. (1985). Nucleation process of stacking fault tetrahedra in gold studied by positron lifetime spectroscopy. *Applied Physics A,* 37(2), 65-72.

65. Sigler, J. A., & Kuhlmann-Wilsdorf, D. (1967). Calculations on the Mechanical Energy of Vacancy Condensation Loops, Stacking Fault Tetrahedra, and Voids. *Physica Status Solidi (B),* 21(2), 545-556.
66. Wang, H., Xu, D. S., Yang, R., & Veyssiere, P. (2011). The formation of stacking fault tetrahedra in Al and Cu: I. Dipole annihilation and the nucleation stage. *Acta Materialia,* 59(1), 1-9.
67. De Jong, M., & Koehler, J. S. (1963). Diffusion of single vacancies and divacancies in quenched gold. *Physical Review,* 129(1), 40.
68. Kuhlmann-Wilsdorf, D. (1965). Theory of melting. *Physical Review,* 140(5A), A1599.
69. Jossang, T., & Hirth, J. P. (1966). The energies of stacking-fault teirahedra in fcc metals. *Philosophical Magazine,* 13(124), 657-670.
70. Loretto, M. H., Clarebrough, L. M., & Segall, R. L. (1965). Stacking-fault tetrahedra in deformed face-centred cubic metals. *Philosophical Magazine,* 11(111), 459-465.
71. Howard, D. J., Bailey, W. E., & Paine, D. C. (1993). Observation of open-ended stacking fault tetrahedra in $Si_{0.85}Ge_{0.15}$grown on V-grooved (001) Si and planar $(1\bar{1}1)$Si substrates. *Applied Physics Letters,* 63(21), 2893-2895.
72. Coene, W., Bender, H., & Amelinckx, S. (1985). High resolution structure imaging and image simulation of stacking fault tetrahedra in ion-implanted silicon. *Philosophical Magazine A,* 52(3), 369-381.
73. Wirth, B. D., Bulatov, V. V., & de la Rubia, T. D. (2002). Dislocation-stacking fault tetrahedron interactions in Cu. *Journal of Engineering Materials and Technology,* 124(3), 329-334.
74. Osetsky, Y. N., Rodney, D., & Bacon, D. J. (2006). Atomic-scale study of dislocation–stacking fault tetrahedron interactions. Part I: mechanisms. *Philosophical Magazine,* 86(16), 2295-2313.
75. Anderson, E., Li, R., & Chew, H. B. (2014). Negative stiffness induced by shear along wavy interfaces. *Journal of the Mechanics and Physics of Solids,* 63, 285-297.
76. Vergnol, J. F. M., & Grilhe, J. R. (1984). Relationship between extrinsic stacking faults and mechanical twinning in FCC solid solutions with low stacking fault energy. *Journal de Physique,* 45(9), 1479-1490.

77. Kim, S. P., Chew, H. B., Chason, E., Shenoy, V. B., & Kim, K. S. (2012). Nanoscale mechanisms of surface stress and morphology evolution in FCC metals under noble-gas ion bombardments. *Proceedings of Royal Society A,* 468(2145), 2550-2573.
78. Dillamore, I. L., & Smallman, R. E. (1965). The stacking-fault energy of fcc metals. *Philosophical Magazine,* 12(115), 191-193.
79. Guan, Q. F., Pan, L., Zou, H., Wu, A. M., Hao, S. Z., Zhang, Q. Y., & Zou, G. T. (2004). Stacking fault tetrahedra in aluminum. *Journal of Materials Science,* 39(20), 6349-6351.
80. Gumbsch, P., & Daw, M. S. (1991). Interface stresses and their effects on the elastic moduli of metallic multilayers. *Physical Review B,* 44(8), 3934.
81. Landau, L. D., & Lifshitz, E. M. (2013). *Course of theoretical physics*. Elsevier.
82. Czigány, Z., & Radnóczi, G. (1999). Columnar growth structure and evolution of wavy interface morphology in amorphous and polycrystalline multilayered thin films. *Thin Solid Films,* 347(1), 133-145.
83. Adams, J. B., Foiles, S. M., & Wolfer, W. G. (1989). Self-diffusion and impurity diffusion of fee metals using the five-frequency model and the Embedded Atom Method. *Journal of Materials Research,* 4(01), 102-112.
84. Cheng, Y., Jin, Z. H., Zhang, Y. W., & Gao, H. (2010). On intrinsic brittleness and ductility of intergranular fracture along symmetrical tilt grain boundaries in copper. *Acta Materialia,* 58(7), 2293-2299.
85. Sangid, M. D., Sehitoglu, H., Maier, H. J., & Niendorf, T. (2010). Grain boundary characterization and energetics of superalloys. *Materials Science and Engineering: A,* 527(26), 7115-7125.
86. Krakow, W., Wetzel, J. T., & Smith, D. A. (1986). Observation and interpretation of the atomic structure of a Σ=19/[110]$(3\bar{3}1)$ tilt boundary in Au thin films. *Philosophical Magazine A,* 53(5), 739-754.
87. Priester, L. (2001). "Dislocation–interface" interaction-stress accommodation processes at interfaces. *Materials Science and Engineering: A,* 309, 430-439.
88. Sansoz, F., & Molinari, J. F. (2005). Mechanical behavior of Σ tilt grain boundaries in nanoscale Cu and Al: A quasicontinuum study. *Acta Materialia,* 53(7), 1931-1944.
89. Wang, J., Misra, A., & Hirth, J. P. (2011). Shear response of $\Sigma3\{112\}$ twin boundaries in face-centered-cubic metals. *Physical Review B,* 83(6), 064106.

90. Tucker, G. J., Tschopp, M. A., & McDowell, D. L. (2010). Evolution of structure and free volume in symmetric tilt grain boundaries during dislocation nucleation. *Acta Materialia,* 58(19), 6464-6473.
91. Allen, M. P., & Tildesley, D. J. (1989). *Computer simulation of liquids.* Oxford university press.
92. Chew, H. B., Hong, S., & Kim, K. S. (2009). Cohesive zone laws for void growth—II. Numerical field projection of elasto-plastic fracture processes with vapor pressure. *Journal of the Mechanics and Physics of Solids,* 57(8), 1374-1390.
93. Kim, H. G., Chew, H. B., & Kim, K. S. (2012). Inverse extraction of cohesive zone laws by field projection method using numerical auxiliary fields. *International Journal for Numerical Methods in Engineering,* 91(5), 516-530.
94. Chew, H. B. (2013). Inverse extraction of interfacial tractions from elastic and elasto-plastic far-fields by nonlinear field projection. *Journal of the Mechanics and Physics of Solids,* 61(1), 131-144.
95. Wang, C. K., Chew, H. B., & Kim, K. S. (2011). Nanometer Scale Mechanical Behavior of Grain Boundaries. *MRS Online Proceedings Library Archive,* 1297.
96. Zimmerman, J. A., Webb III, E. B., Hoyt, J. J., Jones, R. E., Klein, P. A., & Bammann, D. J. (2004). Calculation of stress in atomistic simulation. *Modelling and Simulation in Materials Science and Engineering,* 12(4), S319.
97. Subramaniyan, A. K., & Sun, C. T. (2008). Continuum interpretation of virial stress in molecular simulations. *International Journal of Solids and Structures,* 45(14), 4340-4346.
98. Li, R., & Chew, H. B. (2016). Grain Boundary Traction Signatures: Quantitative Predictors of Dislocation Emission. *Physical review letters,* 117(8), 085502.
99. Xu, X. P., & Needleman, A. (1994). Numerical simulations of fast crack growth in brittle solids. *Journal of the Mechanics and Physics of Solids,* 42(9), 1397-1434.
100. Xie, H., Yu, T., & Yin, F. (2014). Tension–compression asymmetry in homogeneous dislocation nucleation stress of single crystals Cu, Au, Ni and Ni_3Al. *Materials Science and Engineering: A,* 604, 142-147.
101. Lee, D. W., Kim, H., Strachan, A., & Koslowski, M. (2011). Effect of core energy on mobility in a continuum dislocation model. *Physical Review B,* 83(10), 104101.

102. Shimokawa, T. (2010). Asymmetric ability of grain boundaries to generate dislocations under tensile or compressive loadings. *Physical Review B,* 82(17), 174122.